University of Southern Indiana
Pott College of Science, Engineering, and Education
Engineering Department
8600 University Boulevard
Evansville, Indiana 47712

Design of a Lava Rock Crushing System

Aevar Andri Amundinusarson Oefjoerd

ME 491 - Mechanical Engineering Senior Design
Spring 2024

Approved by: _____
Faculty Advisor: Juilian Davis, Ph.D. Date

Approved by: _____
Department Chair: Paul Kuban, Ph.D. Date

ACKNOWLEDGEMENTS

I would like to express significant appreciation to the following people. Without them, this project would not have been possible.

The University of Southern Indiana Engineering Department:

Dr. Glen Kissel

Dr. Todd Nelson

Dr. Julian Davis

Blue Lagoon Iceland:

Ámundínus Örn Sveinsson Öfjörð

Halldór Ingi Lúðvíksson

Abstract

Blue Lagoon, a well-known company in Iceland, is focused on implementing environmentally friendly practices in its skincare line. A significant step in this direction is their plan to start producing lava sand, a critical ingredient in their products, internally. This paper outlines the engineering challenge of developing a system capable of converting local lava rocks into clean lava sand. The process includes washing, crushing, and drying lava rocks. This project combines innovative engineering techniques with sustainable practices, providing Blue Lagoon with a system that aligns with its sustainability goals. The report includes a detailed overview of the process of turning lava rocks into lava sand, and demonstrating the complete approach taken to meet these objectives.

Table of Contents

List of Figures

List of Table

Design of a Lava Rock Crushing System

1 Introduction

Blue Lagoon, based in Iceland, employs over 900 people. The company operates in various areas, with its most notable being the geothermal spa in Grindavik. Additionally, they manage two hotels: the Retreat Hotel and the Silica Hotel. Blue Lagoon also has its own skincare production, and that is where this project fits in.

Blue Lagoon is dedicated to being sustainable and reducing its carbon footprint. Their efforts were recognized in 2021 when they were named the "Icelandic Environmental Company of the Year." They have focused on sustainability for over 40 years, aiming to produce no waste. Their research and development center, powered by geothermal energy, has led to new methods to recycle CO2. This center also develops ways to extract key ingredients from geothermal seawater, like silica, minerals, and algae. These ingredients are important for the Blue Lagoon Skincare line, which started with one product in 1995 and has now grown to include three main product lines: Spa, Derma, and BL+.**[1]**

In 2020, their skincare products earned the COSMOS certification from Ecocert. This means the products meet high standards for being natural and eco-friendly. Also, their BL+ line received an award from ELLE in 2021 for its green approach. An important part of many of their skincare products is lava sand, made from crushed local lava rocks. Currently, they purchase this sand from an external supplier. However, Blue Lagoon aims to start producing it in-house at its R&D center. **[2]**

Figure 1. Image of the Blue Lagoon's geothermal spa **[3]**

1.1 Objective

The objective for his project is:

Design a semi-autonomous system capable of transforming raw lava rocks into clean and dry lava sand.

1.2 Deliverables

- Theoretical Design
- SolidWorks Drawings
- Feasibility Study & Cost-Benefit Analysis

2 Statement of the Problem

An operational challenge for Blue Lagoon Skincare is the sourcing of lava sand with consistent grain size for their Lava Scrub Mask and their Lava Soap Bar. The sand currently used varies in grain size, and only about 1500kg of the 6000kg of sand purchased each year meets the crucial requirement of being 500 micrometers or smaller.

Figure 2. Lava rocks [4]

The inconsistency in the grain size from external suppliers slows the production flow and is at odds with the company's sustainability principles, since sand with grain size larger than 500 micrometers cannot be used in the production. Moreover, transporting the sand from external sources adds to the company's carbon footprint.

The project aims to address this inefficiency by creating an in-house system capable of processing local lava rocks into lava sand with consistent grain size. This system must be robust enough to withstand the challenging environmental conditions at the Blue Lagoon, requiring the use of durable and corrosion-resistant materials or coatings. It is important that this new system integrates smoothly with Blue Lagoon's existing operations, supporting its zero-waste and sustainability commitments.

Implementing this in-house system is expected to improve the Blue Lagoon's skincare production by minimizing waste, reducing the carbon footprint, and ensuring a consistent supply of lava sand.

Figure 3. Lava field around the Blue Lagoon **[5]**

3 System Design and Requirements

3.1 Current Process

Currently, the sand is purchased externally and transported to the Blue Lagoon, where it undergoes several processing steps. Initially, the sand is washed to remove impurities. It is then dried, followed by screening to achieve a consistent grain size of 500 micrometers or smaller. This specific grain size is required to meet the quality standards for the products in which the sand is used.

3.2 System Requirements

- System input: The system shall be capable of processing raw lava rocks with a maximum cross-sectional area of 50x20 cm.
- System output: The system shall produce clean and dry lava sand with a consistent grain size of 500 micrometers.
- Material Durability: All materials used in the construction of the system shall have at least 3-year corrosion resistance to environmental factors, including salty air and sulfur dioxide.
- Operational Safety: The system shall include an emergency stop button and safety shields around moving parts and high-risk areas to prevent accidental injuries.
- Operational Efficiency: The system shall be designed for semi-autonomous operation.
- Maintenance Accessibility: The design shall allow for access to all system components for standard inspections, cleaning, and maintenance tasks.
- Cost: The system shall cost less than $30,000

3.3 Applicable Professional Standards

- ISO 12100: Safety of Machinery - General Principles for Design – “specifies basic terminology, principles and a methodology for achieving safety in the design of machinery. It specifies principles of risk assessment and risk reduction to help designers in achieving this objective. These principles are based on knowledge and experience of the design, use, incidents, accidents and risks associated with machinery. Procedures are described for identifying hazards and estimating and evaluating risks during relevant

phases of the machine life cycle, and for the elimination of hazards or sufficient risk reduction."**[6]**

3.4 Factors That Impact Design

3.4.1 Considerations for Public Health, Safety, and Welfare

During the design phase of the lava sand production system, ensuring public health, safety, and welfare will be a top priority. The system will adhere to ISO 12100 standard, which is important when designing safe machinery and reliable systems. Safety features such as emergency stop button and protective shields will be important to the design to prevent accidents and ensure the safety of operators and maintenance personnel. Additionally, ease of maintenance and resistance to corrosion are also important considerations to increase the system's safety and longevity.

3.4.2 Environmental and Economic Considerations

The design of the lava sand production system will be guided by environmental and economic considerations. Using local lava rocks reduces the need for transported materials, which lowers the carbon footprint and supports Blue Lagoon's environmental sustainability goals. From an economic perspective, the design aims to be cost-effective, with a budget under $30,000.

3.5 System Conceptual Designs

3.5.1 Design 1

The initial Concept for the system consisted of a long conveyor line that would take the lava rock through five different subsystems, a washer, dryer, primary crusher, secondary crusher, and finally a Sand Screening Machine. The process would start by loading lava rocks onto a conveyor belt. The rocks first go through the Rock Washer, where any moss and dirt are washed off. Following this, the rocks proceed to the Rock Dryer for air drying. After they are dried, the rocks enter the crushing phase, beginning with the Jaw Crusher, where they are crushed into gravel-sized pieces. These pieces are then conveyed to the Hammer Mill Crusher for further crushing. The final stage is the Sand Screening, where the crushed rocks are separated into two size groups: one of 500 micrometers and smaller, and the other larger than 500 micrometers.

However, due to concerns about the feasibility of drying the rocks sufficiently given their porous nature, this concept was eventually not pursued.

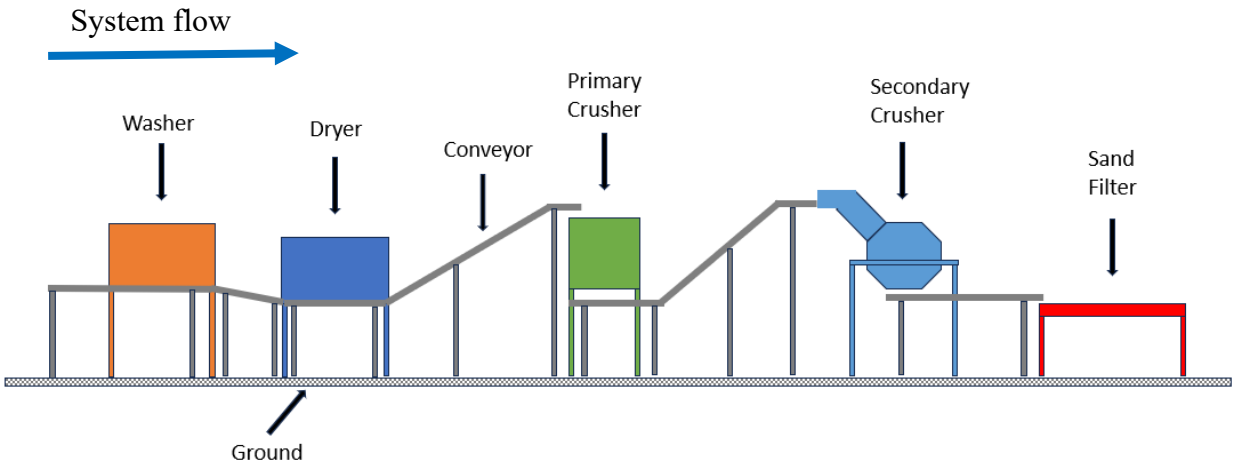

Figure 4. System Concept 1

3.5.2 Design 2

This system concept is split into two smaller systems. System 1 begins with the manual washing of lava rocks using a pressure washer. After this initial cleaning, the rocks are loaded onto a conveyor belt. They then go through a secondary washing stage while on the conveyor. Next, the rocks enter the primary crusher, where they are crushed into gravel-sized rocks. These smaller rocks slide down a declined plate, directing them into the secondary crusher for further crushing into sand. This sand then falls into a collection box when it exits the secondary crusher. This is where system 2 begins, the sand from the collection box must be manually loaded onto the Sand Washer. The sand is then washed in the sand washer, and finally, conveyed to the sand dryer for drying. This Concept, with its more compact design and fewer conveyors, was considered a more efficient alternative to the first Concept.

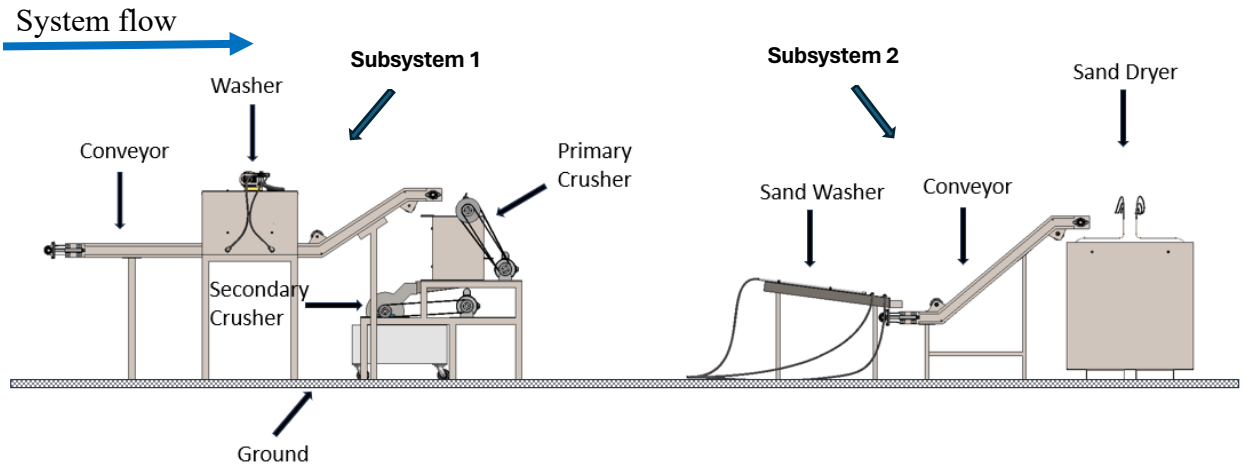

Figure 5. System Concept 2

3.5.3 Design 3

The final design is a simplified version of design 2. It starts with the manual washing of lava rocks using a pressure washer. After this initial cleaning, the rocks are loaded onto a conveyor belt that will take the rocks to the Primary Crusher, where they are crushed into gravel-sized rocks. These gravel sized rocks fall from the bottom of the primary crusher into the Secondary Crusher which is located directly below the primary crusher for further crushing into sand. This sand then falls into a collection box when it exits the Secondary Crusher. The sand will then be manually loaded into the Sand Dryer. Once the sand is dried it is ready to be used.

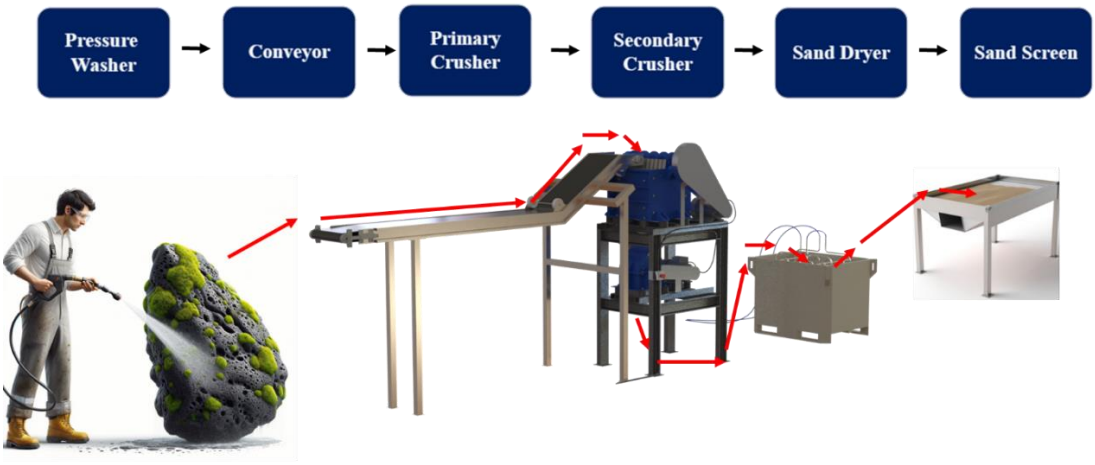

Figure 6. System Concept 3

4 Similar Projects

In my research, I could not find projects identical to mine. Most were related to large-scale mining systems. While these were not direct matches, the individual machines I plan to use are not my invention. I aim to learn from previous design challenges when building each subsystem and adjusting it to the needs of the project.

4.1 Primary Crusher

Selecting an appropriate primary crusher is pivotal for efficiently reducing the size of lava rocks to smaller pieces suitable for the next processing stages. The primary crusher options considered include gyratory crushers, cone crushers, and Jaw Crushers, each offering different advantages.

Comparison of Crusher Types:

- Gyratory Crushers: These crushers are highly effective for hard and abrasive materials, typically used in high tonnage mining and quarrying applications. They offer a good reduction ratio of 4:1 to 7:1 and feature a tall crushing chamber and a robust design. However, gyratory crushers require significant investment and large housing structures, making them less ideal for projects like this which are small on scale compared to mining operations.**[6]**

Figure 7. Gyratory Crusher **[8]**

- Cone Crushers: Known for their ability to handle medium-hard to very hard and abrasive feeds, cone crushers work by compression, similar to gyratory crushers but with a less steeply angled crushing chamber. Their design complexity and the necessity for precise feed size control can complicate the operation and the maintenance.**[9]**

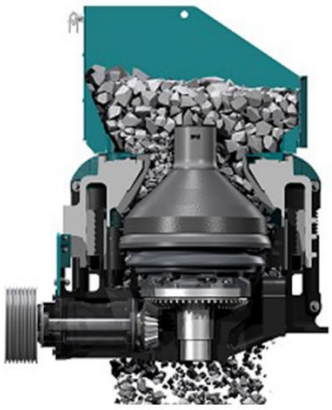

*Figure 8. Cone Crusher***[10]**

- Jaw Crushers: This category includes both single and double toggle Jaw Crushers, which are known for their robustness and ability to crush the toughest materials without significant wear and tear. Jaw Crushers are best suited for heavy mining, quarried materials, and recycling applications. They are especially effective for dry to slightly wet material that is not sticky, making them a good fit for crushing lava rocks. **[7]**

Single vs. Double Toggle Jaw Crushers:

- Single Toggle Jaw Crushers are characterized by their simplified design, which includes fewer moving parts and a single toggle that causes the stationary jaw to crush against a moving jaw. This simple design leads to lower maintenance and potentially lower costs. The design allows for a downward and forward motion that efficiently crushes material at the bottom of the crushing chamber, where the action is most intense **[11]**
- Double Toggle Jaw Crushers use two toggles, connecting the pitman to the jaw, and typically provide more force with each cycle, making them effective for sticky or highly abrasive materials. However, their complex design increases maintenance requirements and operational costs. They also have a lower throughput compared to single toggle Jaw Crushers. **[12]**

Given the project's requirements for a robust yet economically viable system that can operate reliably, a single toggle Jaw Crusher was identified as the most suitable option. This choice was reinforced by the compact design, simplicity, and cost-effectiveness of single toggle Jaw Crushers, which are capable of handling the size of lava rocks.**[11]**

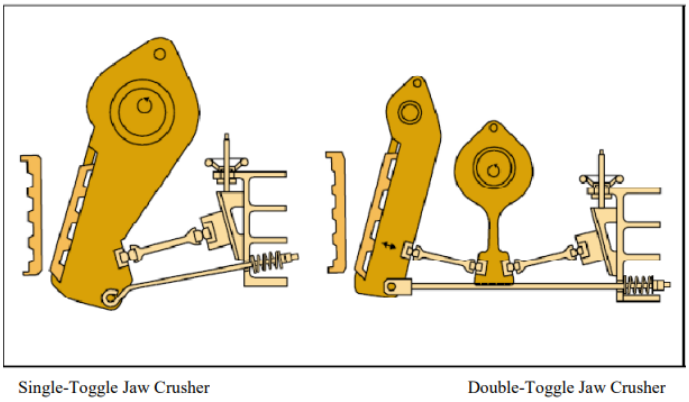

Figure 9. Single and double toggle Jaw Crushers **[8]**

4.2 Secondary Crusher

Following the initial reduction of lava rocks by the primary crusher, the secondary crushing stage aims to further reduce the material size. Given the variety of secondary crusher types, including cone crushers, horizontal shaft impactors, Hammer Mills, and roll crushers, careful evaluation was necessary to select the most suitable crusher.

Overview of Secondary Crusher Types:

- Cone Crushers: Cone crushers reduce material by compression, squeezing it between a moving piece of steel and a stationary liner. This method is highly effective for medium to hard materials and provides a reduction ratio of 6:1 to 8:1. **[13]**
- Horizontal Shaft Impactors (HSIs): These crushers operate with a fast-spinning rotor equipped with hammers to impact the feed material against breaker plates. HSIs are suitable for softer, slightly abrasive materials and provide a good reduction ratio of 8:1 to 10:1. They excel in generating finer materials but may require precise speed and gap settings to achieve the desired output. **[13]**

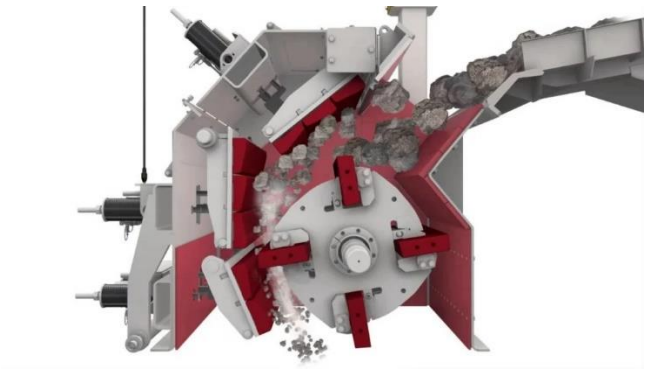

Figure 10. Horizontal Shaft Impactor **[14]**

- Hammer Mills: Hammer Mills use continuous blows by swinging hammers to shatter materials. They are particularly adept at handling less abrasive materials and can achieve high reduction ratios as high as 20:1. Their ability to control product sizing through screen makes them good for creating consistently sized output. **[13]**

Figure 11. Hammer Mill Crusher **[15]**

- Roll Crushers: These crushers are noted for their ability to handle a range of materials from soft to medium hardness. Roll crushers crush material between two rotating rolls equipped with teeth, offering a reduction ratio that typically ranges from 4:1 to 6:1. Their low headroom and horsepower requirements make them suitable for inline installation with other milling operations. **[16]**

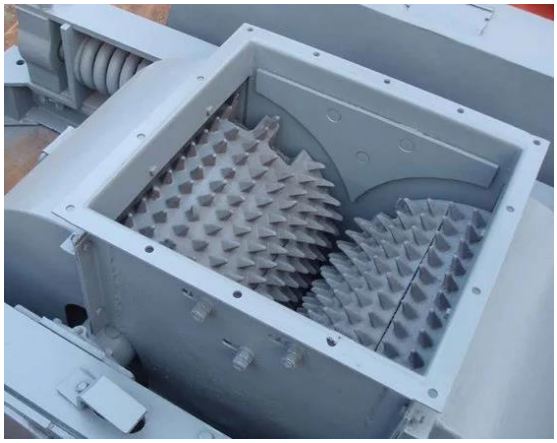

Figure 12. Roll Crusher **[14]**

Selection Criteria and Decision:

Given the project's need to produce a consistent output size from the variably sized output of the primary crusher, the secondary crusher must be capable of handling irregular loads with minimal downtime. The considerations were:

- Efficiency in Size Reduction: Cone crushers and roll crushers, while capable of high reduction ratios, did not match the projects required output size.
- Operational Flexibility and Maintenance: HSIs and Hammer Mills are more adaptable to changes in input size and output goals. However, Hammer Mills provide better reduction and are less prone to clogging compared to roll crushers. **[16]**
- Cost and Maintenance Considerations: Feedback from discussions with an experienced engineer, who has worked with both roll crushers and Hammer Mill Crushers, highlighted that roll crushers tend to have higher operational and maintenance costs. This type of crusher is also more prone to clogging.

Conclusion:

Considering the above factors, Hammer Mills were chosen as the secondary crusher for this project. Their ability to handle varying input sizes, and ability to produce a consistent size reduction are ideal for the demands of this project.

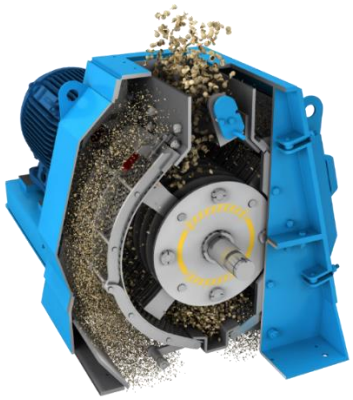

Figure 13. Sectional view of a Hammer Mill Crusher **[17]**

4.3 Sand Dryer

In evaluating various drying methods, it became apparent that traditional sand dryer designs mainly rely on combustion heating methods. These methods, while effective in large-scale outdoor operations or well-ventilated areas, are not suitable for indoor environments due to safety concerns. **[18]**

Traditional sand drying methods typically involve:

- Single Pass Rotary Dryers: These dryers use a direct fire heating method where materials pass through a rotating drum and are exposed to a flame. **[18]**
- Triple Pass Rotary Drum Dryers: Similar to single pass dryers but with enhanced efficiency, these also rely on direct fire methods that may pose risks in enclosed spaces due to fire hazards and exhaust fumes. **[18]**
- Direct Fire Roasting Dryers: Often used in smaller scale or specific applications like drying nuts or grains, these dryers also use open flames which are not suitable for the enclosed operational environment at Blue Lagoon. **[18]**

Current drying method at Blue Lagoon:

The current drying method at Blue Lagoon, which utilizes an insulated container and a heating element which geothermally heated water is circulated through, presents several advantages over the combustion heating methods.

- Environmental Benefits: Unlike combustion-based systems, the current method does not emit harmful byproducts, making it significantly more environmentally friendly.
- Use of Geothermal Energy: The availability of 80°C water from a nearby geothermal power plant provides a unique resource that can be efficiently used for drying sand. This method harnesses renewable energy, which aligns with the sustainability goals of Blue Lagoon.
- Indoor Suitability: The system's design avoids the risks associated with fire-based drying methods, such as exhaust fumes or flames, making it suitable for indoor use.

Strategic Decision to Optimize Existing Technology:

Given the review of available drying methods and resources at Blue Lagoon, it was decided to further optimize the existing drying system rather than replacing it with a conventional combustion-based dryer. The optimization will focus on improving heat transfer efficiency and reducing drying times without compromising the environmental integrity of the process.

Planned Improvements:

- Improving Heat Distribution: Modifying the design of the heating element to achieve more uniform heat distribution within the sand mass, thereby speeding up the drying process while ensuring even drying.

Figure 14. Current Sand Dryer at the Blue Lagoon

5 Subsystem Conceptual Designs

5.1 Subsystem 1 - Primary Crusher

In Section 4.1, the single toggle Jaw Crusher was selected for this project due to its proven robustness and effectiveness in handling hard materials. This section explores the specific design considerations for the primary crusher subsystem, focusing on the standard single toggle design and a new variation of a single toggle Jaw Crusher.

5.1.1 Standard Single Toggle Jaw Crusher

A Single toggle Jaw Crusher has two jaws; one jaw is fixed while the other jaw known as the swinging jaw, is capable of movement. This motion is facilitated by an eccentric shaft located at the top of the swinging jaw as seen in Figure 15. As the shaft rotates, the jaw moves in an elliptical path, moving towards the fixed jaw while simultaneously moving downward, thereby compressing the material placed between the two jaws.

A key component in this system is the toggle plate, attached to the back of the swinging jaw. This plate plays a crucial role in limiting the jaw's backward movement during its elliptical motion. Additionally, the toggle plate serves as a safety device in traditional settings, especially in the mining industry. It is designed to break under excessive load to prevent further damage to the crusher by absorbing forces that exceed the machine's operational tolerance.

For this projects specific design, where the crusher will only process hand-picked rocks of the same type, the toggle plate will not serve as a safety mechanism.

The toggle plate also serves as an adjustment of the crusher's output gap. In traditional single toggle Jaw Crushers, a toggle plate system is positioned between two seats, one on the swinging jaw and the other on the back plate. A rod attached to the swinging jaw equipped with a compression spring pulls the swinging jaw back towards the back plate, ensuring the toggle plate remains securely within the two seats.

For adjusting the gap, smaller crusher models often use a screw located behind the toggle seat on the back plate, which adjusts the seat's position forward or backward, thus altering the gap size. In larger crushers, a hydraulic system is used instead the adjustment screw, using hydraulic power to shift the jaw position.

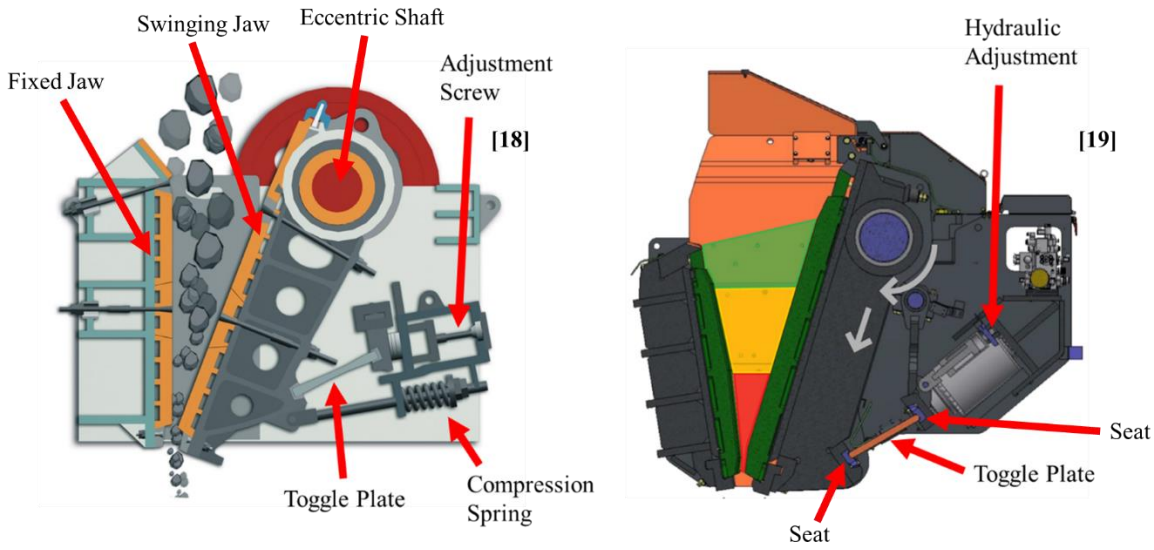

Figure 15. Two Types of Toggle Mechanisms

5.1.2 Single Toggle Jaw Crusher – Concept 1

The first Concept for the Jaw Crusher features a unique alternative to the traditional single toggle Jaw Crusher design. This new design maintains the placement of the driving shaft at the top part of the swinging jaw, similar to conventional models. However, it introduces an innovative toggle mechanism that differentiates it from standard configurations.

Contrasting with the traditional method, the new Concept uses two shafts, one shaft passes through aligned holes in the back of the swinging jaw and holes on the toggle plate, the other shaft passes through aligned holes on a bracket that is bolted to the back plate and through holes on the toggle plate. To adjust the crusher's output gap, spacers are inserted or removed between the bracket and the back plate. This method simplifies the gap adjustment process and eliminates the need for a compression spring to secure the toggle plate.

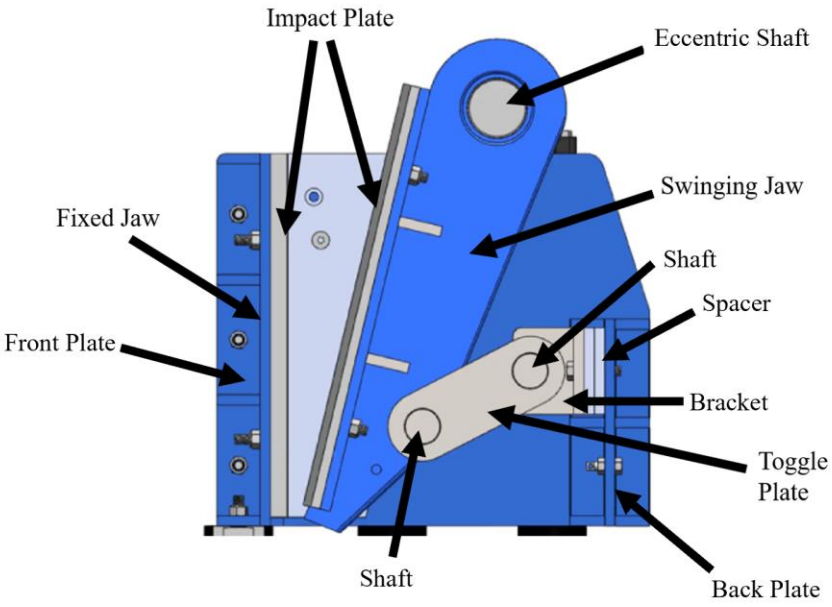

Figure 16. Jaw Crusher Concept 1

5.1.3 New Concept Single Toggle Jaw Crusher – Concept 2

This section introduces a new approach to the design of the single-toggle Jaw Crusher, which deviates from the traditional placement of the shaft. Traditionally mounted atop the crusher, the shaft in this Concept is directly attached to the toggle plate located behind the swinging jaw. This strategic relocation is inspired by the mechanics of a double toggle Jaw Crusher, altering the movement of the swinging jaw from its usual elliptical path to an arc like motion. This change mirrors the functionality of the double toggle Jaw Crusher and is expected to enhance the output force by enabling a more direct application of force during the crushing process. This is because the force is concentrated in a single direction, unlike in Concept 1, where the output force is directed both toward the fixed jaw and downward.

In this new design, the method for adjusting the output gap is different from the standard adjustment methods for Jaw Crushers and also the Concept mentioned previously. The flange bearings that secure the shaft are mounted in adjustable locations on the crusher housing. Operators can alter the vertical position of these bearings by switching the holes where they are bolted to the housing. Moving the bearings upward increases the gap, allowing larger material to pass through, while moving them downward decreases the gap, resulting in finer crushed material.

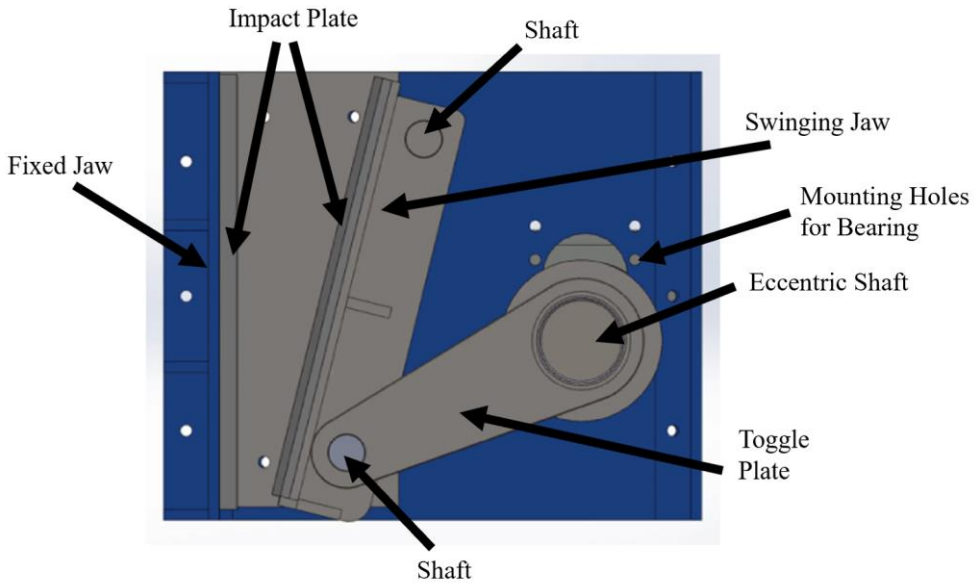

Figure 17. Jaw Crusher Concept 2

5.2 Subsystem 2 - Secondary Crusher

To further reduce the size of the lava rocks to achieve an output of 500 micrometers, a secondary crushing stage is necessary. As outlined in Section 4.2, the Hammer Mill Crusher was chosen for this purpose due to its suitability for achieving the desired granularity.

Hammer Mill Crushers consist of a rotating shaft equipped with free-swinging hammers which are mounted on the shaft. As the shaft rotates, these hammers swing out due to centrifugal force and strike the material as it enters the crushing chamber.

Once inside, the material is repeatedly struck by rotating hammers. The impact of the hammers not only breaks down the material but also propels it against the walls of the chamber, for further sized reduction, these repeated impacts cause the material to shatter.

Typically, at the bottom of the crushing chamber is a screen in which the crushed material exits the chamber. The screen's hole size determines the final size of the crushed material, as only particles small enough to pass through the holes can exit the crusher. Larger particles remain in the crushing chamber, where they continue to be struck by the hammers until they can pass through the screen.

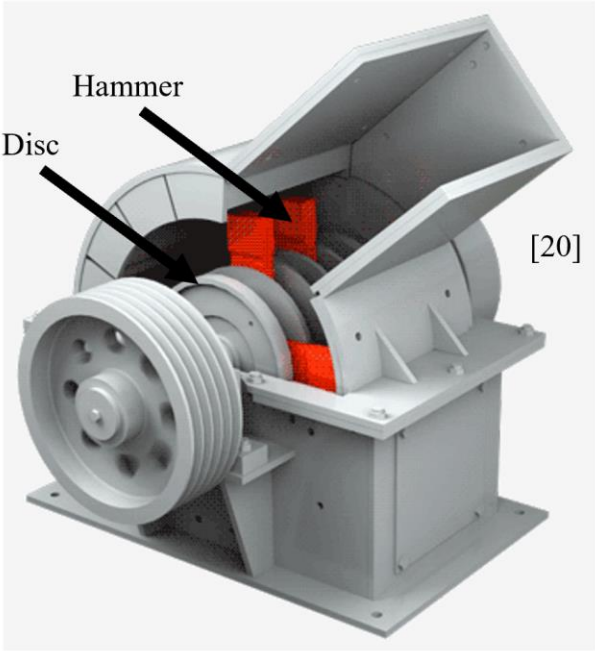

Figure 18. Hammer Mill Crusher **[21]**

5.2.1 Hammer Mill Crusher Concept 1

The initial design for the Hammer Mill Crusher featured a circular housing with an angled entry for the material. This angled entry was specifically chosen to reduce the likelihood of materials being ejected back out upon impact with the hammers. Additionally, the screen within the crusher was positioned parallel to this entry point rather than at the bottom of the housing. The rationale behind an angled screen was to minimize clogging. With this setup, rocks not small enough to pass through the screen would either fall to the bottom of the crusher for further processing or be subjected to additional impacts from the hammers and preventing buildup on the screen.

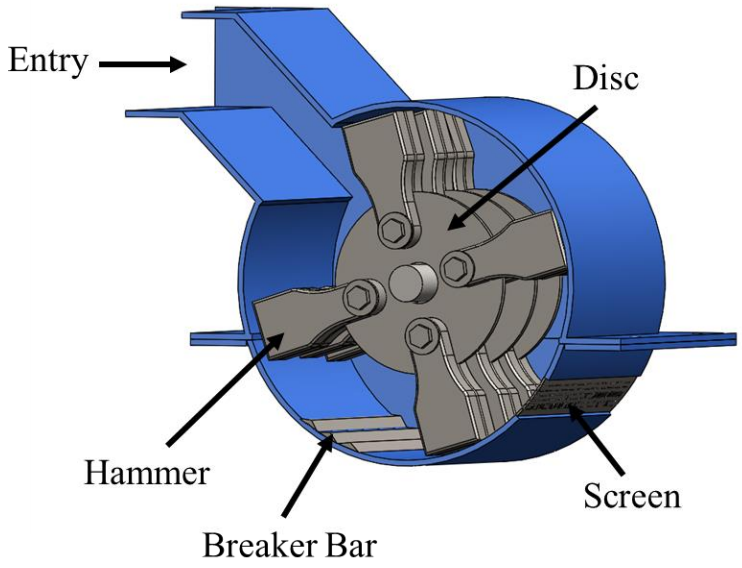

Figure 19. Hammer Mill Crusher Concept 1

5.2.2 Hammer Mill Crusher Concept 2

Built on the foundation laid by the first Concept, the second Concept Hammer Mill Crusher addressed several identified weaknesses to improve durability and efficiency. One of the key improvements was the integration of replaceable impact plates within the crusher housing. This modification allows for simple replacement of the worn plates instead of the entire housing, extending the lifespan of the crusher and reducing maintenance costs. Additionally, the screen area was enlarged to allow for more material to pass through, aiming to decrease the potential for clogging.

Another change was the replacement of welded breaker bars with impact plates that also serve as wear plates. This modification not only simplifies maintenance but also improves the wear resistance of the crusher since once the impact plate wears down it can be replaced by a new one, instead of having to replace part of the housing. Finally, the material entry point was relocated from an angled position to the top of the crusher. This top entry design was thought to reduce the chances of material being propelled back out through the entrance by the hammers.

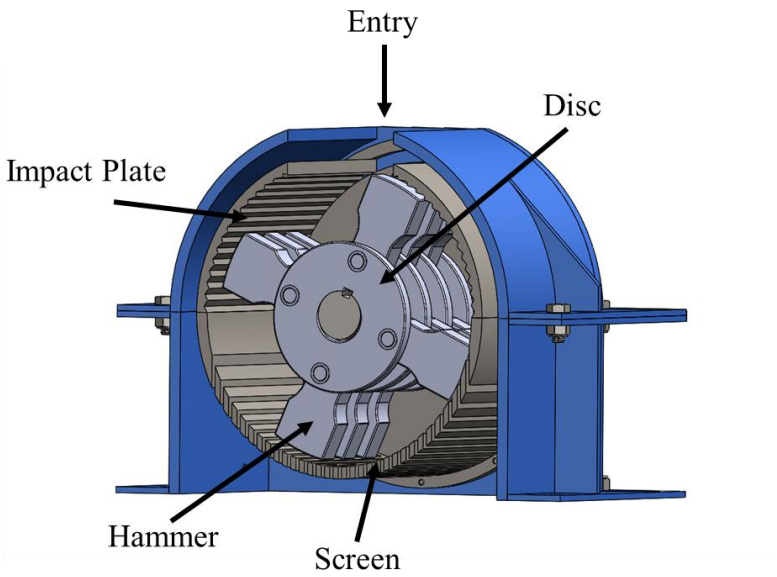

Figure 20. Hammer Mill Crusher Concept 2

5.3 Subsystem 3 - Sand Dryer

Developing the Concept for the sand dryer was straightforward, given the successful prototype previously conducted by an engineer at the Blue Lagoon, as detailed in Section 4.3. The Concept uses three heating elements instead of just one, allowing for uniform heat distribution across the sand in the container. These elements are supported by two rods that go through holes in the walls of the container, instead of the elements being inserted in the sand horizontally they are set up vertically, making it easy to detach the water hoses connected to each element if needed.

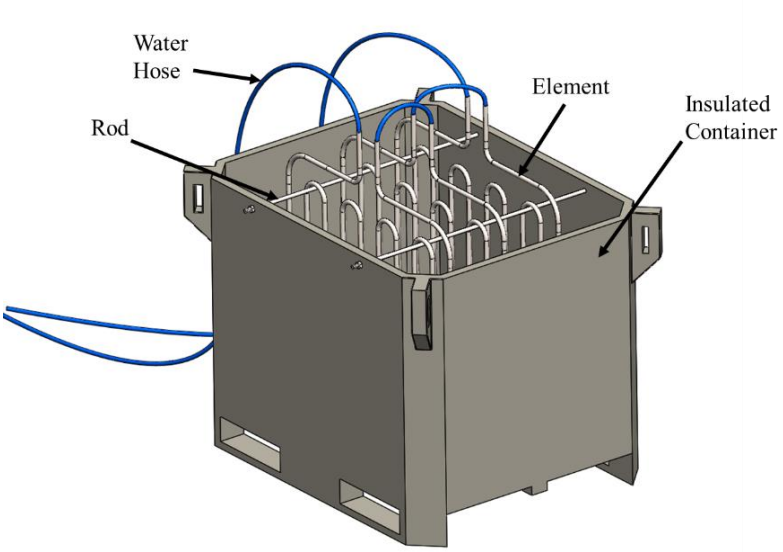

Figure 21. Sand Dryer Concept

6 Testing

For testing, a sample lava rock from the lava field where project materials will be sourced was selected. This rock was broken down into three smaller samples. Traditionally, to assess the compressive strength of a rock, the sample is shaped into a cylinder with flat surfaces to ensure uniform load application during testing with a compression testing machine. This conventional method guarantees the even distribution of pressure across the specimen.

In this experiment, however, the selected sample was chosen specifically for its flat surface to simulate as uniform a load as possible during testing, while also resembling the typical rocks targeted by this project. There was initial concern that the non-uniform nature of lava rocks, characterized by their rough surfaces and nibs, might affect the test results. As pressure was applied during testing, these nibs broke down, and the specimen slowly flattened, suggesting that the load was becoming more uniformly distributed across the sample's surface, which was a positive outcome and indication of a reliable test results.

Figure 22. Sample Before being Broken into Three Smaller Samples

6.1 Primary Crusher

To test the force needed for the primary crusher each of the three samples was weighed, and their volume was determined by water displacement method, by measuring the amount of water each rock displaced when submerged. The density of the rocks was then calculated by dividing the mass by the volume. Measurements of the average thickness and surface area of the samples were also taken to prepare for testing.

The samples were then subjected to a compressive strength test, where a machine applied load until the samples fractured into smaller pieces. The maximum load sustained by each sample before failure was recorded, and the compressive strength was calculated by dividing this load by the contact area of each sample. The average compressive strength of the samples was 1529 kPa. This testing approach, while unusual, provided insights into the structural properties of the rocks, and important information for the next steps, which involve calculations and stress analysis for the final design of the crushers.

Table 1. Test Results for Primary Crusher

	Sample 1	Sample 2	Sample 3	Average	[units]
Weight	140.00	105.00	68.00	**104**	g
Volume	97.00	64.00	41.00	**67.3**	cm^3
Density	1.44	1.64	1.66	**1.58**	g/cm^3
Thickness	3.35	4.20	3.70	**3.75**	cm
Area	52.0	34.5	31.2	**39.2**	cm^2
Max load until failure	6.77	8.51	2.55	**5.94**	*kN*
Cross Sectional area	0.00520	0.00345	0.00312	**0.00392**	m^2
Compressive strength	1302	2470	816	**1529**	*kPa*

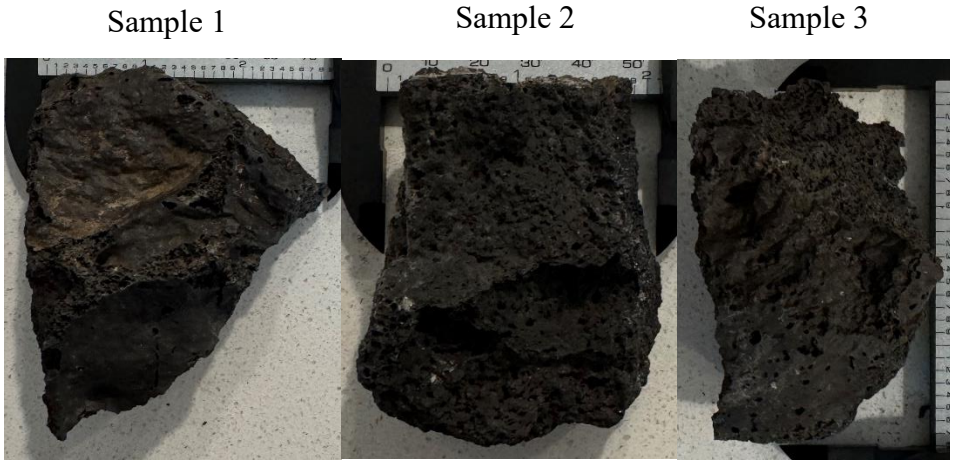

Figure 23. Samples 1, 2 and 3 Before Testing

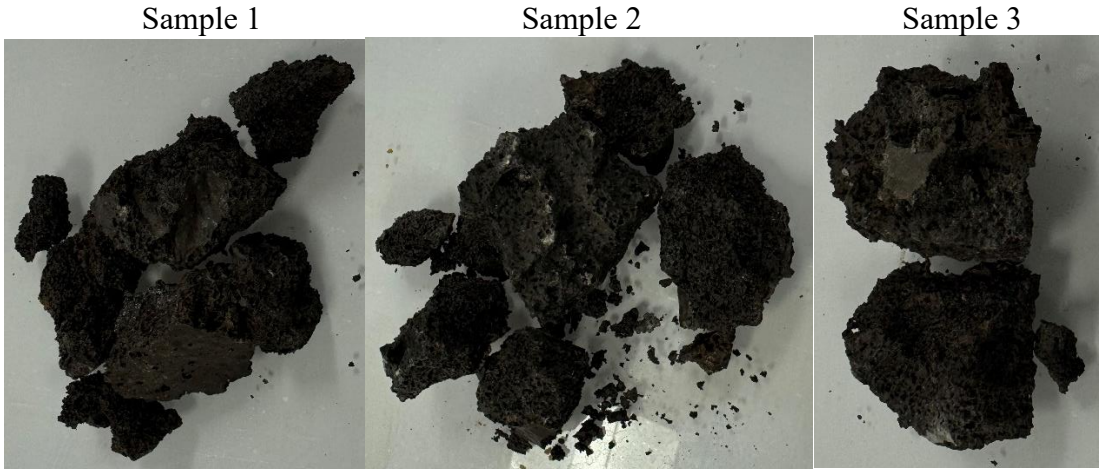

Figure 24. Samples 1,2 and 3 After Testing

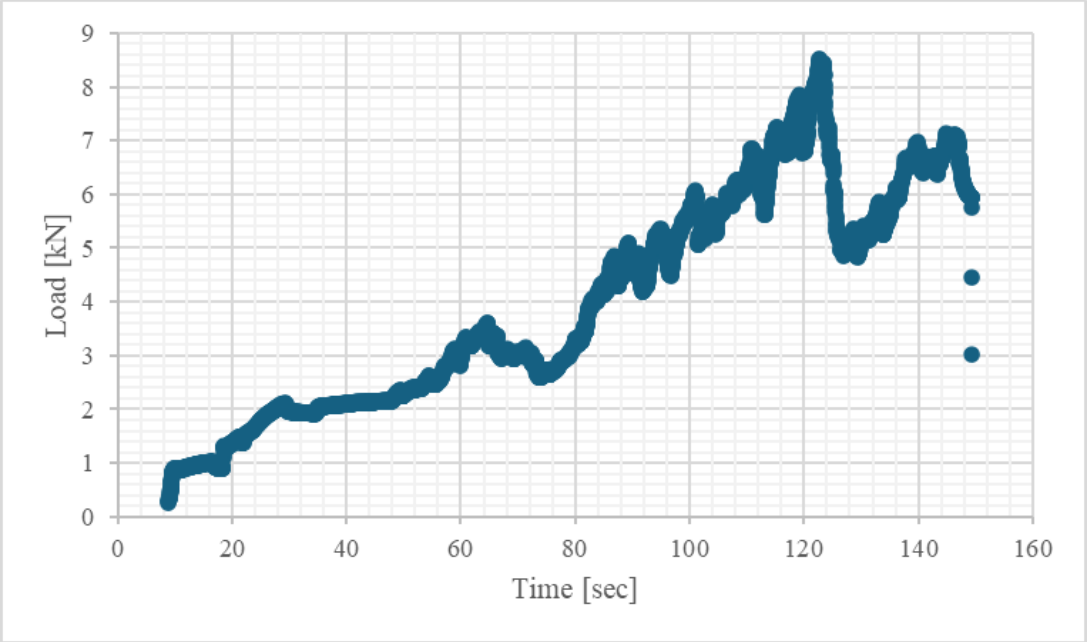

Figure 25. Plot from Testing of Sample 2

6.2 Secondary Crusher

For the secondary crusher, four samples were tested to determine the force needed to crush them to sand. These samples were collected from the pieces of the three samples used in testing for the primary crusher and were specifically chosen because they matched the size of the rocks that will be processed in the secondary crusher. The same preparatory methods used for the primary crusher samples were applied, including weighing, volume measurement via water displacement, and density calculations. The crucial difference in testing these samples was that compressive strength was not the focus, instead, the maximum load until failure was the focus area. This is due to the fact that Hammer Mills, which are used in the secondary crushing stage, operate on a principle of impact force rather than compressive force. The results from these tests showed that a force of 2.29 kN was required to crush the samples into sand.

Table 2.Test Results for Secondary Crusher

	Sample 4	Sample 5	Sample 6	Sample 7	Average	[units]
Weight	16	11	7	7	**10.25**	g
Volume	3	2	2	2	**2.25**	cm^3
Density	5.33	5.50	3.50	3.50	**4.46**	g/cm^3
Thickness	2.27	1.93	1.74	1.81	**1.94**	cm
Area	1.32	1.04	1.15	1.10	**1.15**	cm2
Max load until failure	2.72	2.52	1.46	2.46	**2.29**	kN

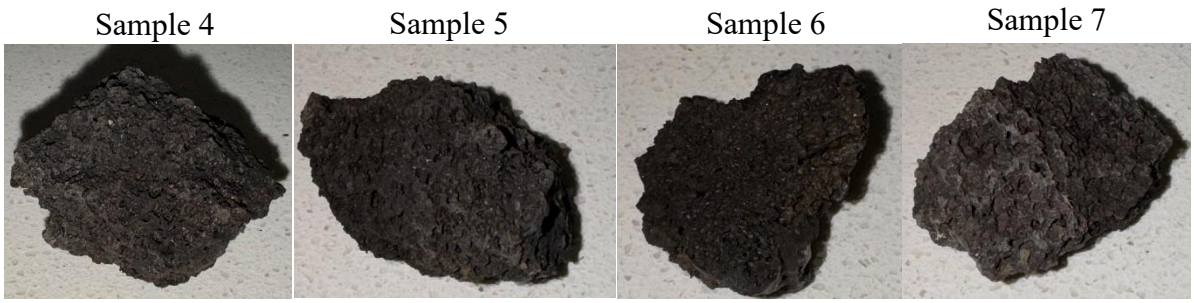

Figure 26. Samples 4, 5, 6 and 7 Before Testing

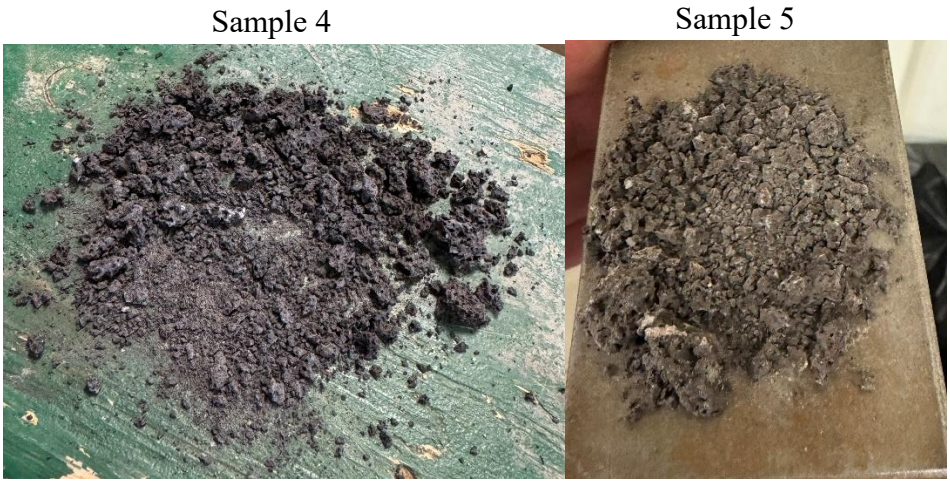

Figure 27. Samples 4 and 5 After Testing

7 Final Design

This section provides a comprehensive overview of the final design for all the subsystems included in this project, including the Primary Crusher, Secondary Crusher, Support for the Crushers, and the Sand Dryer.

7.1 Primary Crusher

This section provides an overview of the calculations and final design for the Primary Crusher.

7.1.1 Crushing Stages

The initial step in the calculations for the Jaw Crusher involves determining the required output force. This process begins by estimating the impact areas within the crusher, referred to as crushing stages. These stages are crucial for predicting where on the swinging jaw the rocks will be crushed. As the rocks are broken down, they fall to the next crushing stage, where they are further reduced before moving to subsequent stages. This process continues through the five crushing stages of the Jaw Crusher.

To accurately determine the output force needed at each crushing stage, the area of each stage was estimated. This estimated area was then used to calculate the force required to crush the rocks at each stage based on the compressive strength of the lava rocks. The compressive strength of the lava rocks was determined through experiments and detailed in Section 6.1. However, since only one rock sample was used in the experiment, and considering the variable porosity of lava rocks which can significantly affect their compressive strength, the results may not accurately represent the average property of lava rocks. Given this variability in porosity of lava rocks, it was decided to assume the compressive strength to be 25% higher than the experimental results for safety and reliability in design calculations. The new compressive strength of the lava rocks was calculated to be 1911kPa after adding 25% to the experimental compressive strength of 1529kPa.

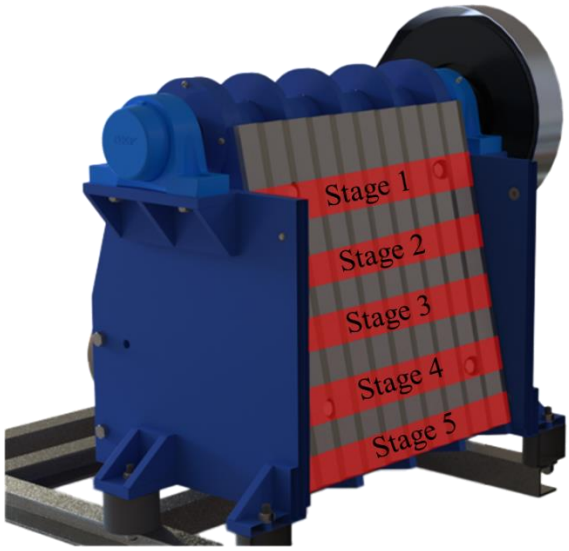

Figure 28. Estimated Crushing Stages of the Jaw Crusher

The calculation involves dividing the area of each crushing stage by the adjusted compressive strength of the lava rocks. This division provides an estimate of the force required at each stage to effectively break down the rocks. The estimated force needed per stage, with this adjusted compressive strength, was found to be approximately 46 kN. This value represents the targeted force that the Jaw Crusher needs to exert at each stage to ensure crushing and processing of the lava rock into smaller pieces suitable for further processing.

7.1.2 Calculations

This section outlines the calculations performed to assess the mechanical limits and stresses acting on the components of the primary crusher. These calculations include evaluating the joint forces, the drive shaft durability, the maximum output force, and the shaking force. Each of these calculations are important for ensuring the crusher's reliability and effectiveness in processing lava rocks.

7.1.2.1Joint Forces

To calculate the joint forces of the Jaw Crusher, four-bar linkage calculations were used. The length of the links was determined using SolidWorks sketches for the two primary crusher Concepts. Initially, a global coordinate system was established for the entire system, followed by a local coordinate system designated specifically for the four-bar linkage calculations of each

Concept. In the local system, the x-axis extends from where link 2 is grounded to where link 4 is grounded, simplifying the calculations. The results were then translated back to the global coordinate system.

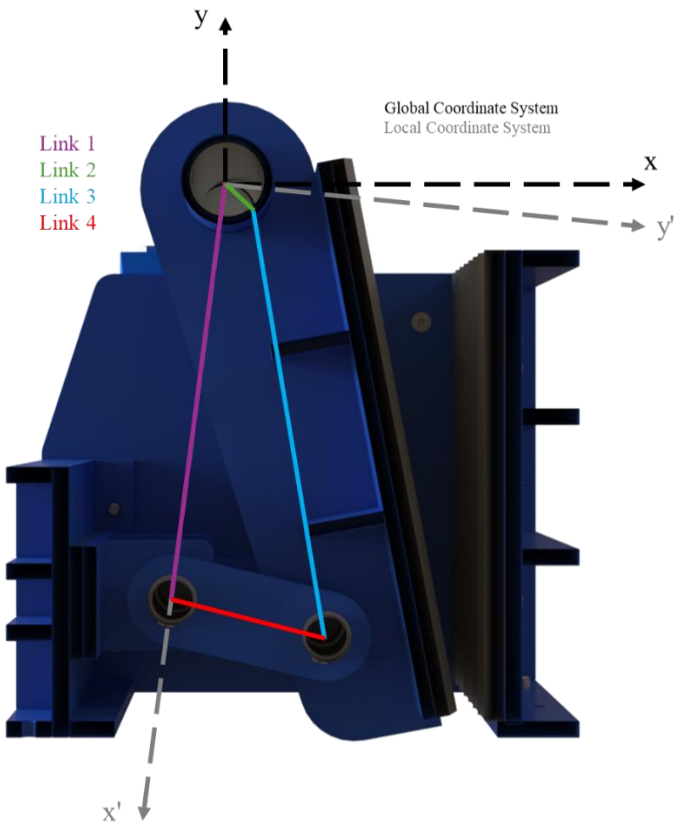

Figure 29. Cross Sectional View of Concept 1 Jaw Crusher Showing the Four Links

What was different about the calculations for Jaw Crushers from the standard four bar linkage calculations is that the length of the link 3 was not constant as the length varies as the eccentric shaft rotates. This variation is due to the joint between link 2 and link 3 being located on the edge of the eccentric shaft that is furthest from the center of the shaft, however the lengths of links 1, 2 and 4 were constant. The varying length of link 3 affected other dimensions needed to perform the four bar linkage calculations, for both Concepts the necessary dimensions needed to be measured as the shaft rotated and that was done using the SolidWorks drawings for Concepts. The necessary dimensions were recorded for every 30 degree rotation of the shaft and MATLAB was used to keep record of these numbers and to perform the calculations, calculations for one scenario can be seen in appendix A.

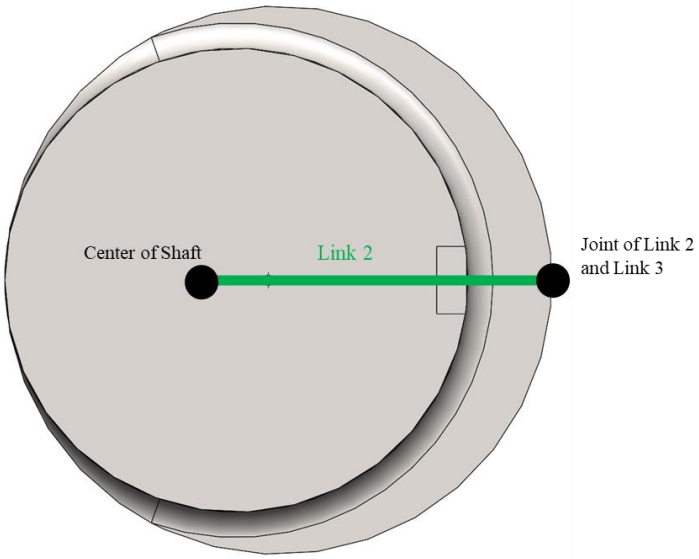

Figure 30. Figure Showing the Joint of Link 2 and Link 3

With all the dimensions recorded there only few more details were needed. The details that needed to be added were thickness and material selection, the thickness of each link was initially estimated, as the exact stress in each links was not yet known and the thickness would likely require adjustment in later stages of the design process. The material chosen for the initial design was medium carbon steel. This selection was made because the specific type of carbon steel had not yet been decided, and the variations in density between the different types of carbon steel would not have much effect on the results.

With all dimensions and the material specified, determining the center of gravity, moment of inertia, and mass of each link was straightforward using SolidWorks mass property Table. The only remaining element needed to complete the joint force calculations was the torque applied to link 2. To calculate this torque, it was decided to set the pulley ratio between the Jaw Crusher and the motor at 3:1, with the driven pulley being larger than the driving pulley. This configuration increases the torque output at the driven pulley since Torque = Force x Radius. The system will be powered by a 3 hp motor and the angular velocity of the shaft will be 200rpm. The angular velocity for the shaft was chosen based on research that showed the optimal running speed was between 120rpm to 300rpm [22].

To accurately simulate the crushing process, the velocity along the x-axis at each of the five crushing stages was calculated. This was done to determine whether the swinging jaw was

moving backward or forward. By calculating the velocity in the x-direction for each stage, it was possible to predict if an external force was acting on that stage, caused by a rock pushing back as it was being compressed in the crusher. This played a crucial role in accurately determining the joint forces.

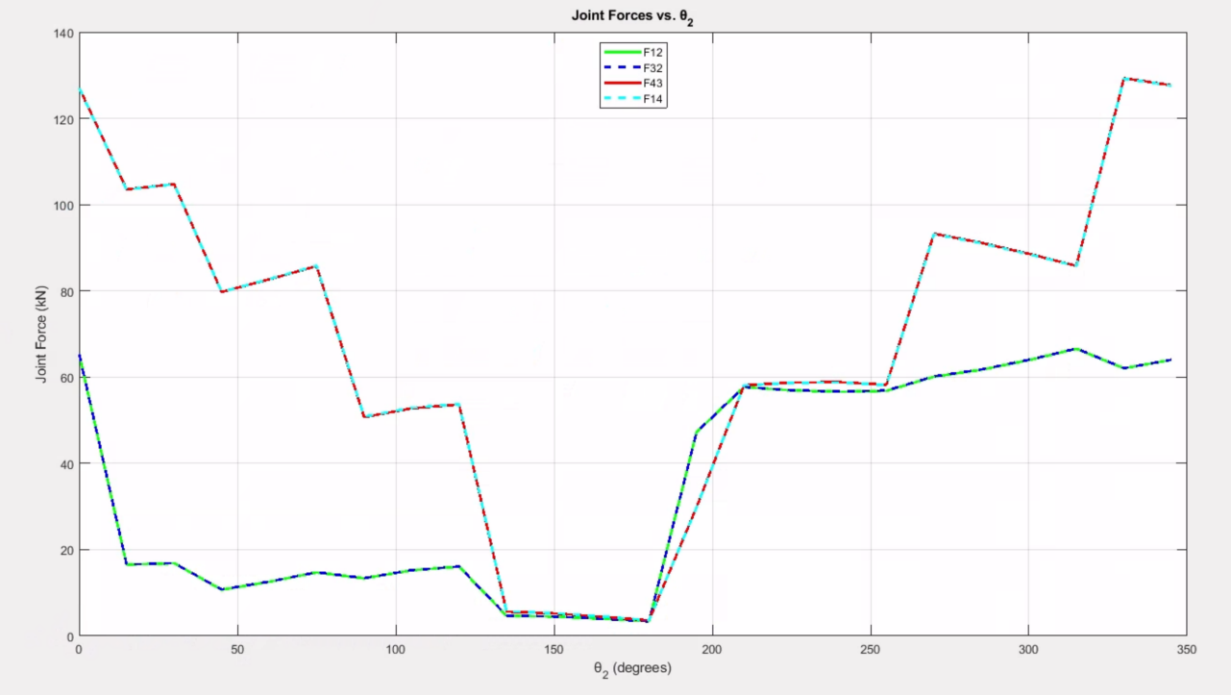

Figure 31. Graph Showing the Joint Forces as the Shaft Rotates in Global Coordinates

The components of each joint force can be seen in the Table below, these components will be used to determine the stress in each part of the Jaw Crusher by using SolidWorks Simulation.

Explanation of the Joint forces:

- F12: This force is exerted by link 1 on link 2. In the context of the Jaw Crusher, this is the force exerted on the crusher's shaft by the bearings.
- F32: This is the force exerted on link 2 by link 3, this is the force exerted on the shaft by the swinging jaw.
- F43: Is the force exerted on the swinging jaw by the toggle plate.
- F14: This force is exerted on the back plate by the toggle plate.

The MATLAB files for the joint force calculations can be found on the flash drive "JawCrusherConceptTwoJointForces.m," "JawCrusherConceptOneJointForces.m,"

Table 3. Components of each Joint Force For the Global Coordinate System

	x-component	y-component	
F12	65.94	-9.17	kN
F32	-66	9.12	kN
F43	82.64	-23.14	kN
F14	82.54	-23.13	kN

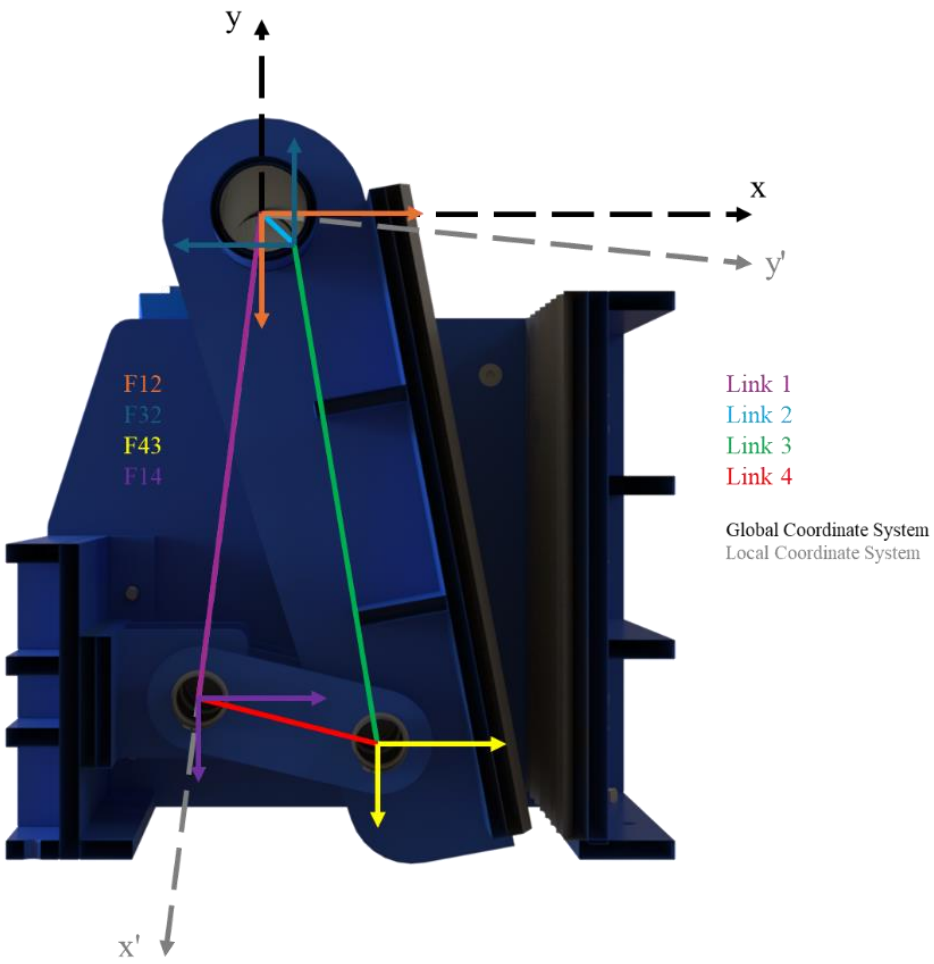

Figure 32. Free Body Diagram of the Joint Forces

7.1.2.3 Drive Shaft Durability

After determining the joint forces, the next step involved calculating the durability of the driving shaft. To ensure the shaft's reliability under load, the Goodman Factor of Safety was calculated at the points where the shaft's diameter changes, which are the area's most susceptible to stress concentrations. The Goodman Factor of Safety is used to evaluate the fatigue failure potential of components subjected to varying stress cycles like the driving shaft of the Jaw Crusher.

Figure 33. Electric Shaft, Highlighted Areas were the Diameter Changes

Several shaft diameters were tested for both of the Concepts for the Jaw Crusher to determine the most suitable dimensions. It was found that crusher Concept 2 imposed much higher loads on the shaft, which in turn would require significantly larger bearings. Accommodating these bearings would require larger housing for the Jaw Crusher, complicating the design and potentially increasing costs and maintenance complexity.

Therefore, Jaw Crusher Concept 1 was chosen as more suitable option of the two Jaw Crusher Concepts. This design proved to be more feasible as it placed less stress on the shaft and allowed for the use of smaller sized bearings and smaller diameter shaft than Jaw Crusher Concept 2. Calculations are in Appendix A and also in MATLAB files "JawCrusherConceptOneGoodmanFOS.m," "JawCrusherConceptTwoGoodmanFOS.m" on the flash drive.

Table 4. Jaw Crusher Concept 1 vs Concept 2 Shaft Diameter Comparison

	Concept 1	**Concept 2**	
Force Acting on Shaft	66.85	167.18	kN
Changes in Shaft Diameter	50→60→50	90→100→90	mm
Goodman FOS	1.11 1.15	0.99 1.08	

7.1.2.4 Geometry and Material Selection

After determining all the joint forces, the next crucial step was selecting the appropriate material for the project. Upon consulting with an engineer who has 8 years of experience working at the Blue Lagoon, it was recommended to use EN 10025 steel, a type of low carbon structural steel, for the crusher's construction. However, concerns were raised regarding the material selection, particularly because EN 10025 steel does not possess corrosion resistance properties. Addressing these concerns, the engineer shared positive experiences with this type of steel in other projects at the Blue Lagoon where it was sandblasted, primed, and painted.

Since the material had been selected, SolidWorks Simulation was used to calculate the required thickness for each component, to ensure they can withstand the loads previously calculated in the joint force analysis. To find the optimal thickness trial and error method was used. Initially, a material thickness of 10mm was selected, and the MATLAB code was updated to reflect the changes based on the geometry and properties of the material. Following this update, a new set of joint forces was calculated, and static SolidWorks simulation was conducted. The results indicated that 10mm of EN 10025 steel was insufficient. Subsequently, simulations were performed using 12mm steel, but the results indicated that a thicker material was necessary. The simulations revealed that there were spots in the design where the stress was close to or exceeded the yield strength of the material. After conducting simulations with 15mm steel, it was determined that this thickness was sufficient to withstand the static loads. To further evaluate its durability under operational conditions, a SolidWorks fatigue simulation was performed to assess whether the material could also handle the dynamic loads, which it did. Therefore, 15mm steel was ultimately selected for the design.

7.1.2.5 Force Output

With one Concept eliminated, the focus shifted to calculating the output force of Jaw Crusher Concept 1. To calculate the output force, the principle of power conservation was applied as shown below:

$$P_{in} = P_{out} \rightarrow T_{in} \cdot \omega_{in} = F_{out} \cdot v_n \rightarrow F_{out} = \frac{T_{in} \cdot \omega_{in}}{v_n} \quad (1)$$

To achieve more accurate output force and joint force results, additional dimensions were recorded at finer intervals. Instead of recording the dimensions for the four-bar linkage model every 30-degree rotation of the shaft, dimensions were now recorded every 15-degree rotation. With all the calculations needed from the MATLAB code used in the joint force calculations to perform the output force calculations, no extra work was needed. The calculations can be found on the flash drive in the file "JawCrusherConceptOneForces.m."

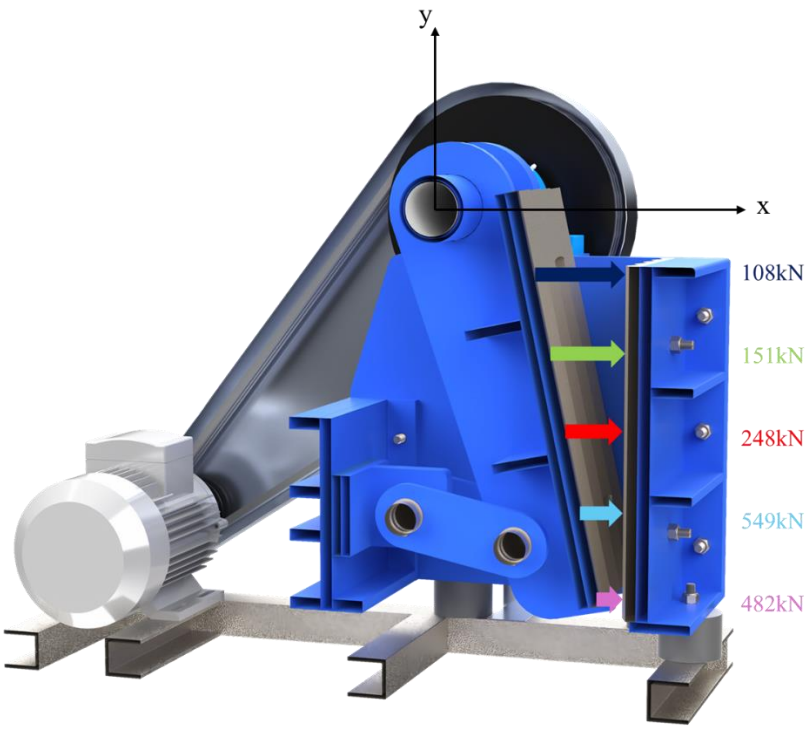

Figure 34. Cross Sectional View of Jaw Crusher Concept 1 Showing the Maximum Output Force along the x-axis

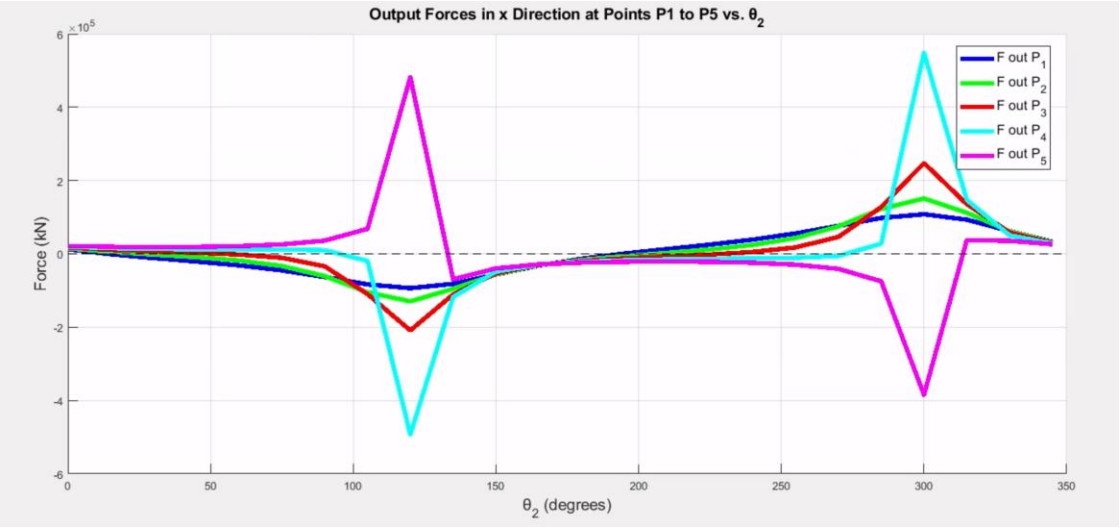

Figure 35. Graph Showing the Maximum Output Force Along the x-axis as the Driving Shaft Rotates

7.1.2.6 Updated Drive Shaft Durability

After updating the geometry of the design and the joint forces, it was necessary to recalculate the Goodman Factor of Safety. This recalculation was important because the initial values used in the calculations had changed due to adjustments in material thickness, which altered the geometry of the links. This step was critical for determining the final geometry of the driving shaft required to handle the dynamic load of the crushing process. Additionally, recalculating the Goodman Factor of Safety was crucial for estimating the life expectancy of the shaft at the critical points, where the shaft diameter changes, also known as shoulders.

Figure 36. Jaw Crusher Driving Shaft, Shoulders Highlighted

The updated calculations indicated that the Goodman Factor of Safety for the shaft's shoulder 1 was 1.48, with an estimated life of approximately 8.88 million cycles. For shoulder 2, the Factor of Safety was calculated at 1.54, with a calculate life of about 11.18 million cycles. These numbers translate into a minimum running time of 733 hours when the crusher operates at a speed of 200 rpm.

The change is vertical deflection (slope) of the shaft was calculated to ensure proper alignment and function of the bearings. The calculations showed that the slope was within acceptable limits. To secure the shaft within the housing, two deep groove ball bearings are used, and additionally, two cylindrical roller bearings are inserted in the swinging jaw. Analysis of the slope plot below revealed that the slope values are below the maximum allowable slope for both types of bearings along the entire length of the shaft. The calculations to prove this can be found on the Flash Drive in the file "JawCrusherConceptOneGoodmanFOS.m."

Table 5. Max Slope for Bearings **[23]**

Slopes	
Tapered roller	0.0005–0.0012 rad
Cylindrical roller	0.0008–0.0012 rad
Deep-groove ball	0.001–0.003 rad
Spherical ball	0.026–0.052 rad
Self-align ball	0.026–0.052 rad
Uncrowned spur gear	<0.0005 rad

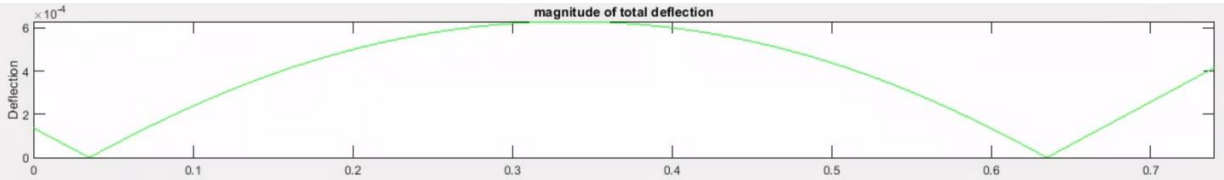

Figure 37. Slope Graph for the Jaw Crushers Driving Shaft

7.1.3 Unique Design Features

This section outlines the unique features of this single toggle Jaw Crusher design.

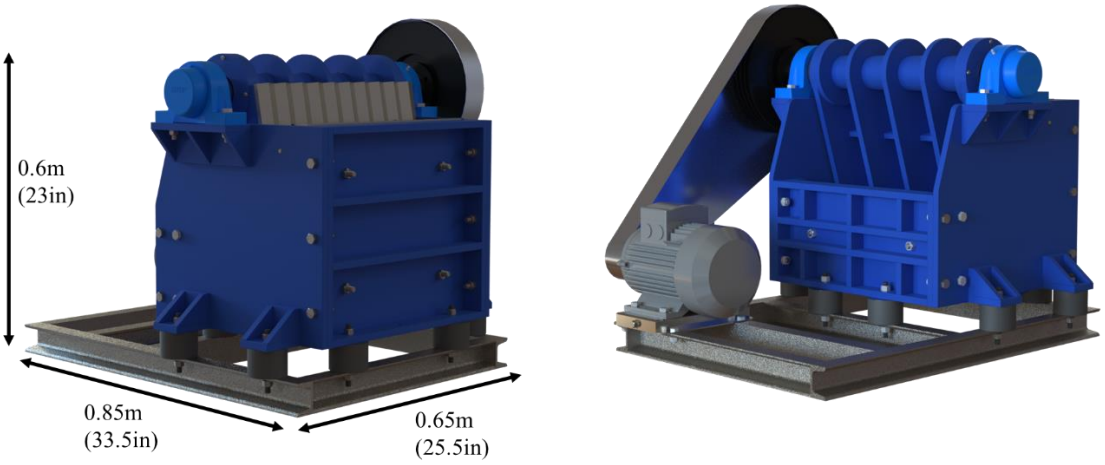

Figure 38. Final Design of the Jaw Crusher

7.1.3.1 Housing

The housing design of this Jaw Crusher is different from standard designs primarily because it uses bolted connections instead of the traditional welded joints to assemble the front plate, side plates, and back plates. This choice enhances the overall maintainability of the crusher. Bolted connections allow for easier disassembly of the housing, which is beneficial in the corrosive environment where the crusher will operate. This feature helps when performing routine inspections and maintenance, as components can be removed and reattached without the need for cutting and re-welding, thereby simplifying the maintenance process.

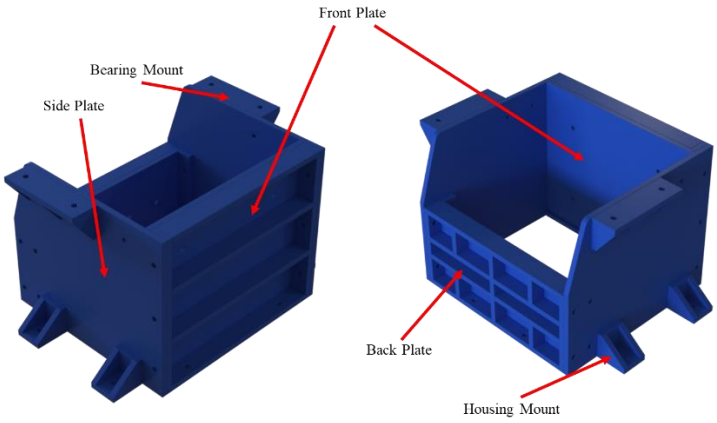

Figure 39. Housing Components

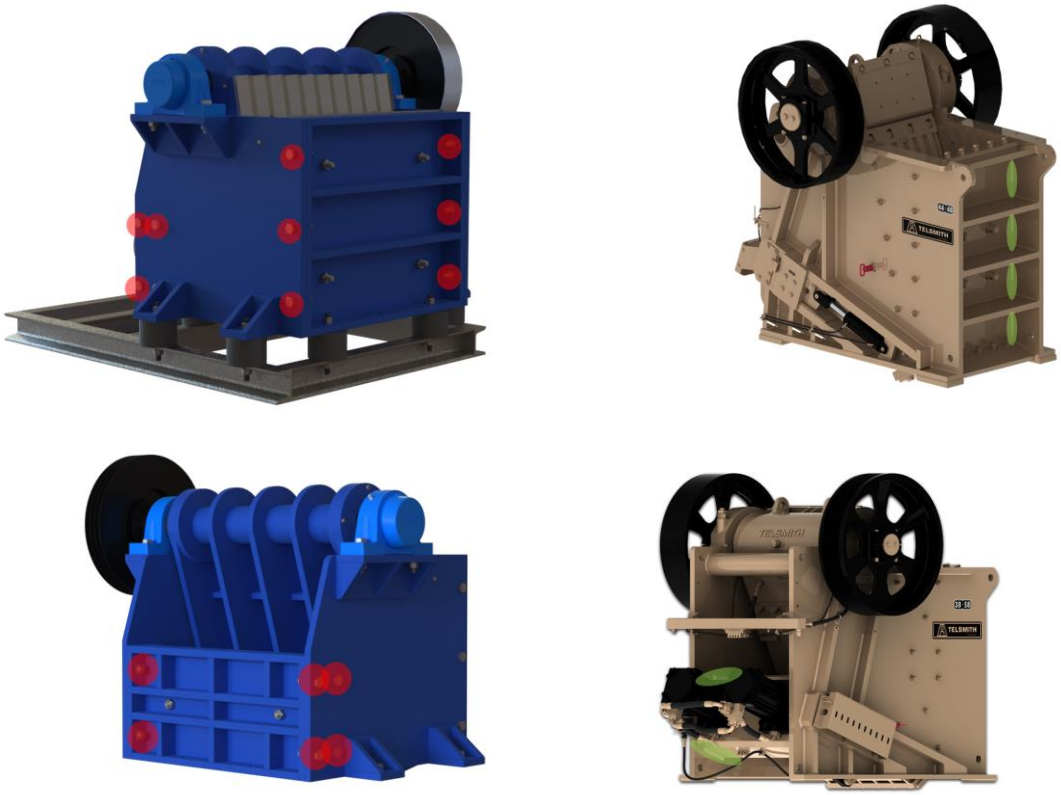

Figure 40. Bolted Connections of Jaw Crusher Concept(left) shown in red and Welded Connections of Typical Jaw Crusher(right) shown in green **[24]**

7.1.3.2 Toggle Mechanism

What distinguishes the toggle mechanism in this design is its lack of an adjustment screw or hydraulic system, as discussed in Section 5.1.2. Instead, it employs four plates that are secured to two shafts using external retaining rings. These shafts are also connected to the swinging jaw,

inserted through holes on the swinging jaw as shown in the Figure 42. The toggle plate is then linked to the housing via the back plate. Attached to this back plate is a bracket with holes, allowing one of the shafts from the toggle plate to pass through. This bracket is bolted onto the back plate of the housing rather than welded. The bolted connection is used so that spacers can be placed between the back plate and the bracket, thus enabling adjustment of the Jaw Crusher's output gap.

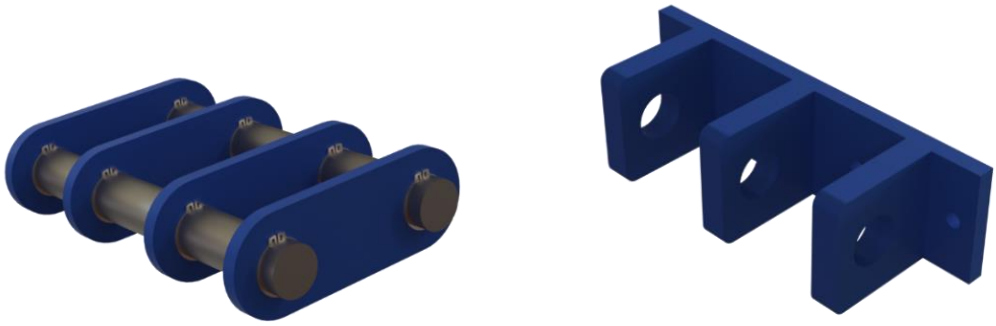

Figure 41. Toggle Plates, Shafts and Bracket

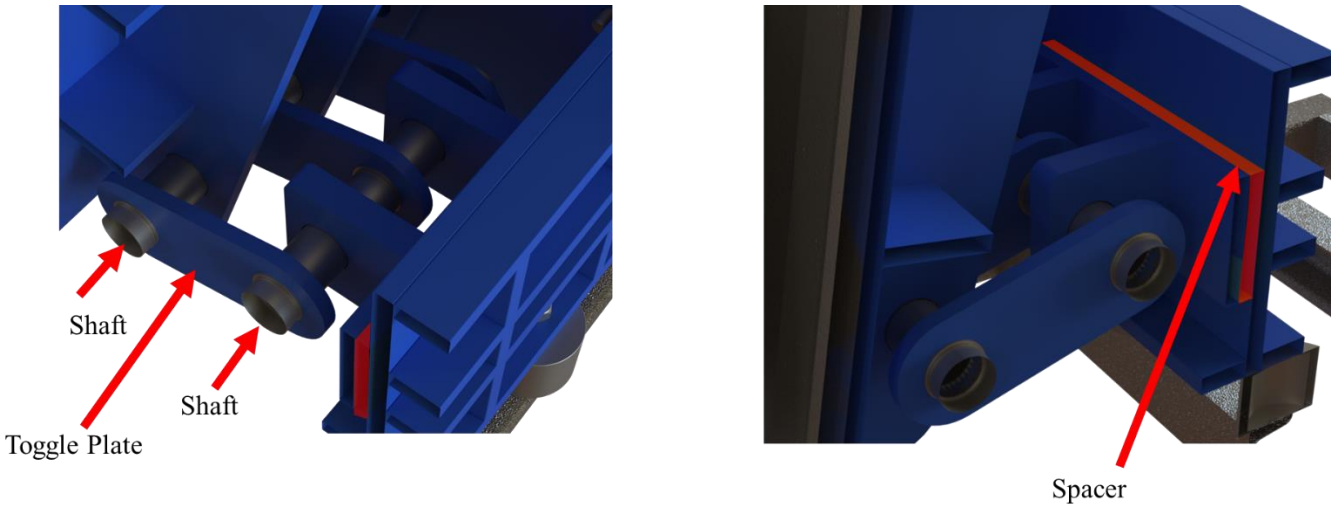

Figure 42. Toggle Plates, Shafts and Bracket

7.1.3.3 Flywheel

Another unique feature of this design is the lack of a flywheel. The reason is due to the specific characteristics of the processed material, since lava rocks have low compression strength, the additional torque and momentum provided by a flywheel is not necessary for this crusher. Efforts to compare the compression strength of lava rocks from my experiments with similar testing method of iron ore which is a common material processed by Jaw Crushers were unsuccessful due to the unconventional testing methods as discussed in Section 6.1. Although a direct comparison of compressive strengths could not be made, it is still relevant to note the significant difference in strength. Medium hardness iron ore typically has a compressive strength of 110-200 Mpa **[25]**, compared to only 1.5 MPa for the lava rock tested in my experiment.

7.1.4 Stress in Components

This section will discuss the stress analysis performed on the components of the Jaw Crusher. It will demonstrate how each component is capable of withstanding the loads encountered during the crushing operation. The analysis will detail the loading and boundary condition set for the stress and fatigue simulations in SolidWorks. The static simulation will demonstrate that the components can withstand the maximum static load they will encounter during the crushing process. This ensures that the parts are robust enough to handle the highest forces expected under normal operations without failure. Following this, fatigue simulations are conducted to confirm that the components can endure the repeated loading of the crushing process. These simulations assess the durability of the parts over time, ensuring they can perform reliably through multiple cycles of stress, which is important for the longevity and safety of the crusher.

7.1.4.1 Housing

- Boundary Condition: Holes where motor mounts would be bolted were fixed, total of six holes.
- Loading condition:
    - Bearing Mount: 66kN(downward) and 9kN(left)
    - Back Plate: 124kN(left) and 36kN(upward)
    - Front Plate: 125kN(right)

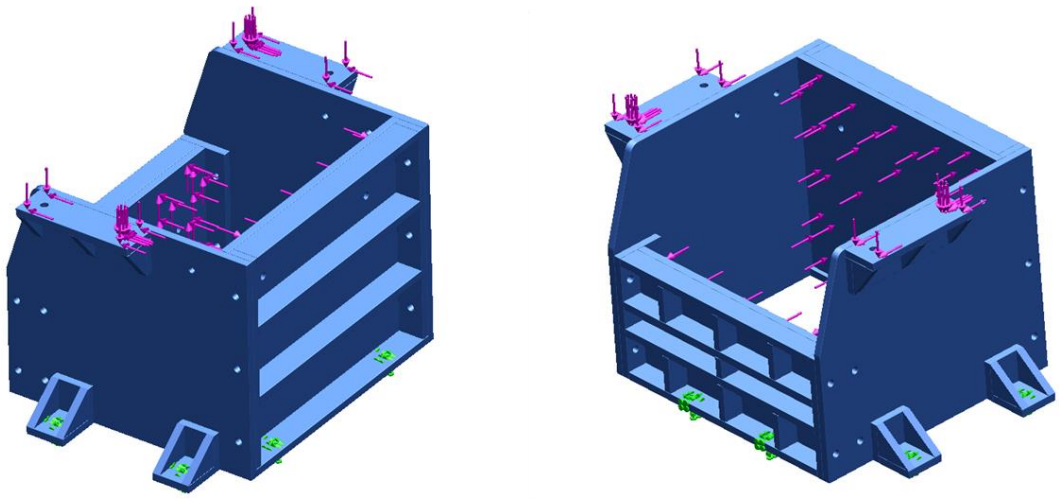

Figure 43. Boundary and Loading Condition for SolidWorks Simulations

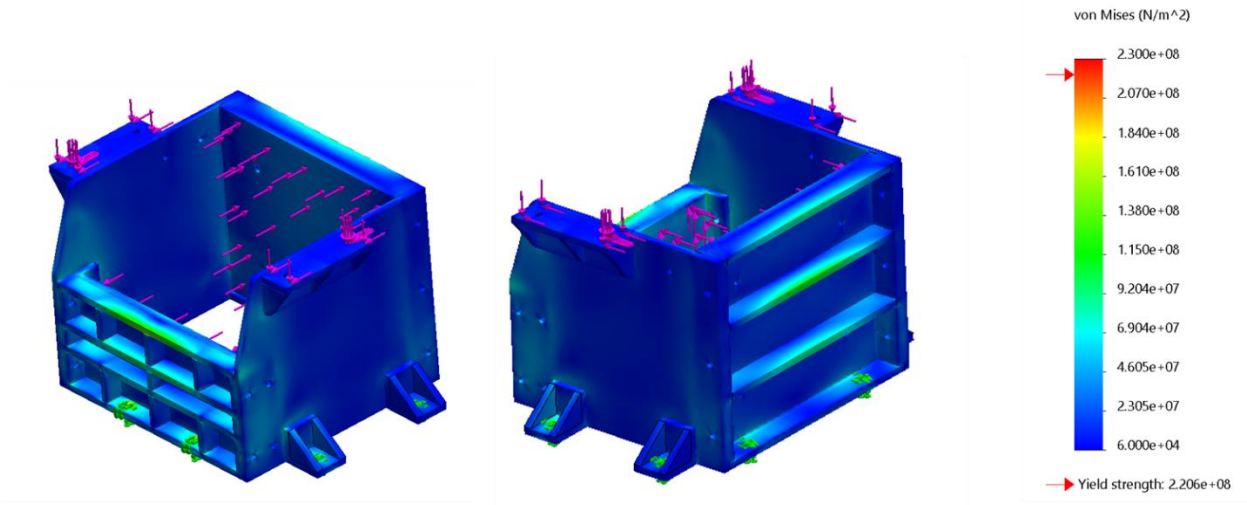

Figure 44. Von Mises Stress Plot from SolidWorks Simulation

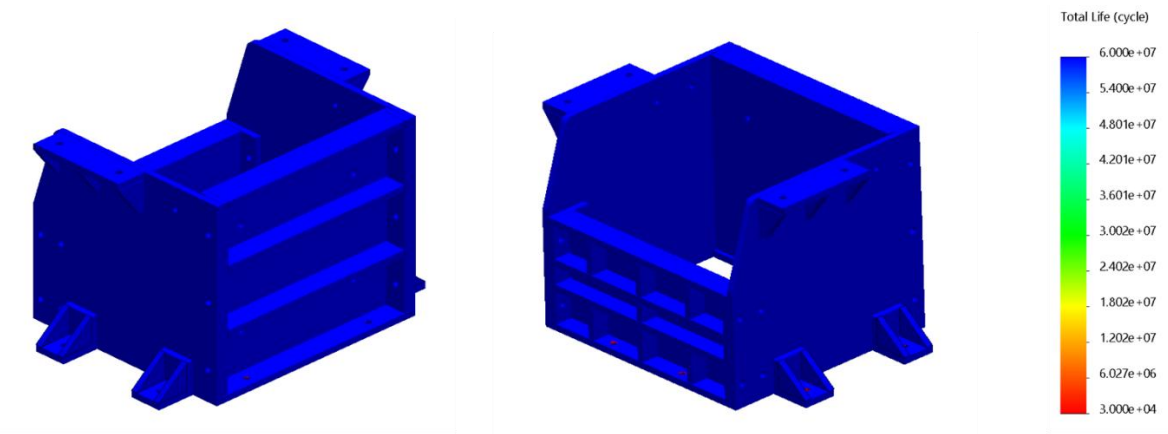

Figure 45. Fatigue Plot from SolidWorks Simulation,

The results show that the housing can withstand the maximum static load applied during operations. Specifically, the areas experiencing the highest loads were found to be significantly below the material's yield strength, approximately 1.0e+8 $^{N}/_{m^2}$under the yield limit. However, the fully reversed fatigue simulation indicates minor wear around the bolt holes, where the model was fixed, this wear starts to show after approximately 30,000 loading cycles.

7.1.4.2 Swinging Jaw and Toggle Mechanism

- Boundary Condition: Back of bracket and inserted bearings on swinging jaw
- Loading condition:
    - Front Plate: 125kN

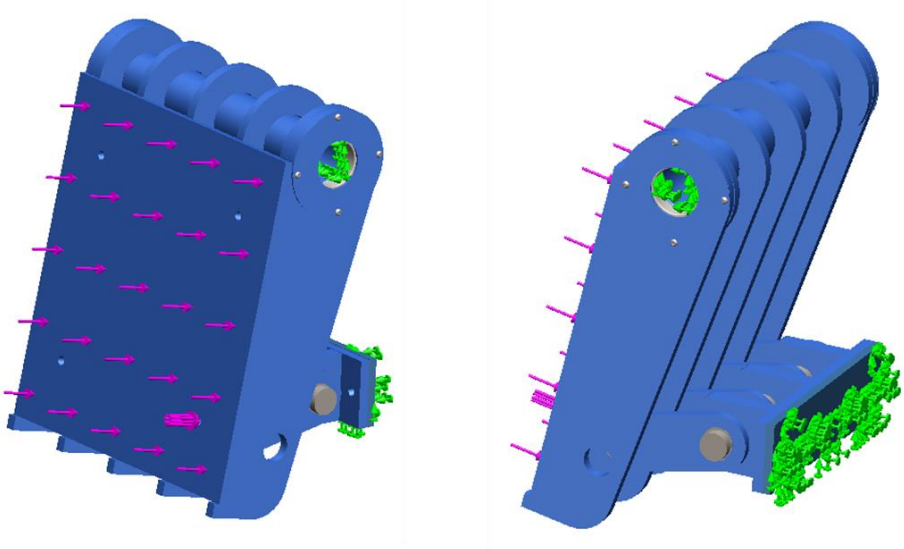

Figure 46.Boundary and Loading Condition for SolidWorks Simulations

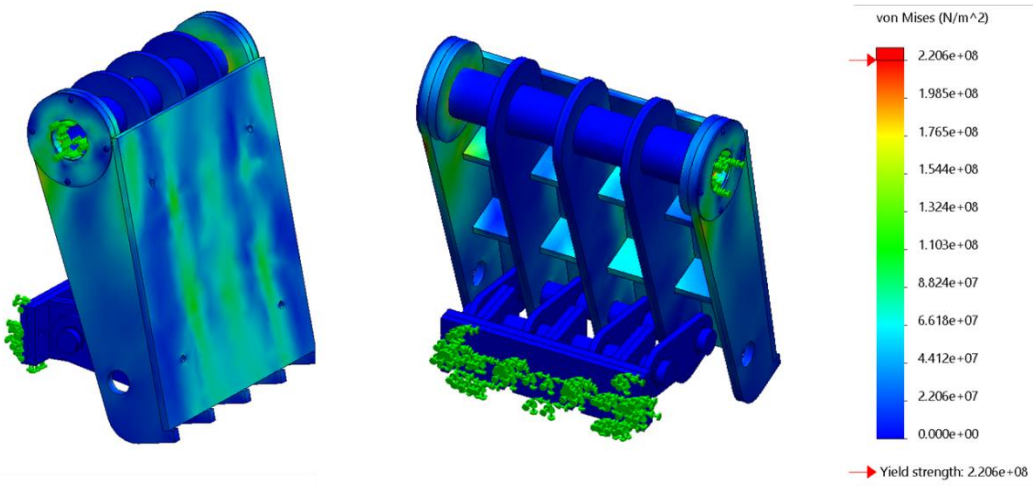

Figure 47. Von Mises Stress Plot from SolidWorks Simulation

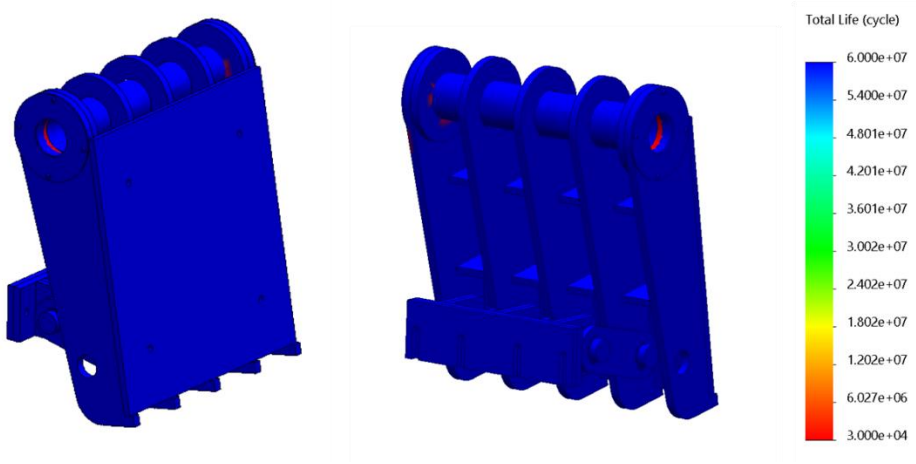

Figure 48.Fatigue Plot from SolidWorks Simulation

The results show that the swinging jaw and the toggle mechanism can withstand the maximum static load applied during operations. However, the fully reversed fatigue simulation indicates minor wear where the inserted bearings are located, this wear starts to show after approximately 30,000 loading cycles.

7.1.4.3 Impact Plate

- Boundary Condition: Back of plate
- Loading condition:
    - Front Plate: 125 kN total

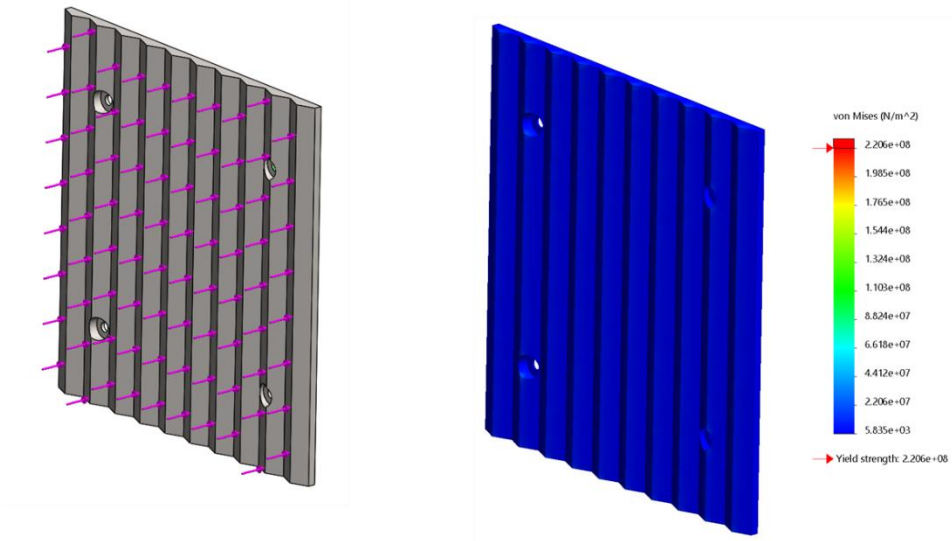

Figure 49. Loading Condition and Static Simulation Results

Static simulation was conducted for the impact plate on the swinging jaw. Since the load on the impact plates for both the fixed and swinging jaws is similar, only one simulation was necessary. The static simulation revealed no wear points on the impact plates, the stress on the plate was too minimal for SolidWorks to run fatigue simulation. This finding suggests that the impact plate is sufficiently tough to handle the operational loads without significant wear or failure under normal conditions. Initially there was concern that using the same structural steel for the impact plates would cause problem with the durability of the plates, that has now been shown to not be the case.

7.1.5 Jaw Crusher Overview

The calculations and simulations have demonstrated that the Jaw Crusher is capable of crushing rocks with a cross-section of 20cm x 50cm. This maximum size is dictated by the fixed input gap of the crusher, which also acts as a safety feature to ensure that all components can withstand the crushing process's load. The output gap of the crusher is adjustable, with spacers allowing it to be modified to as narrow as 2cm or even smaller, as previously mentioned.

Another requirement for the crusher is to have at least a 3-year resistance to corrosion. This will be achieved by painting each component. However, it is expected that the paint on the impact plates will wear off and they will rust over time. Fortunately, since these plates are only secured by four bolts each, they are easily removable. This allows for straightforward maintenance where the plates can be sandblasted to remove rust and then repainted.

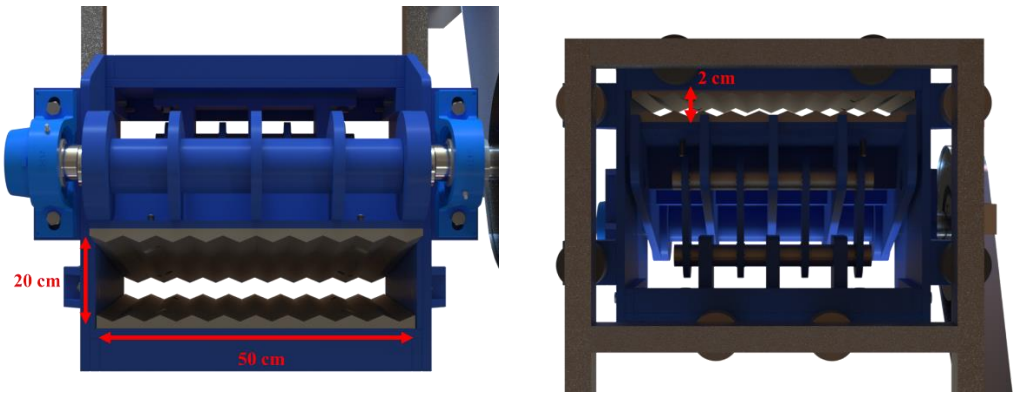

Figure 50. Input and Output Gap of the Jaw Crusher

7.2 Subsystem 2 – Secondary Crusher

This section provides an overview of the calculations and final design for the Hammer Mill Crusher, including unique design features, calculations, and stresses in components.

7.2.1 Unique Design Features

This section outlines the unique features of this Hammer Mill Crusher design.

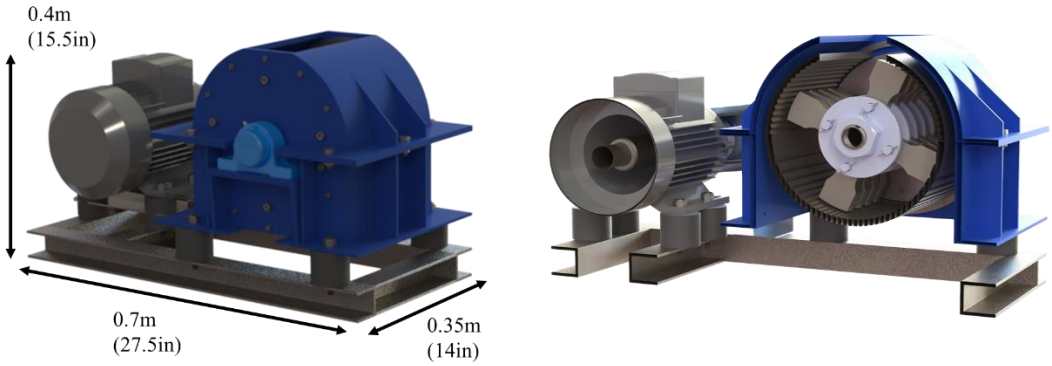

Figure 51. Final Design of the Hammer Mill Crusher

7.2.1.1 Crushing Chamber

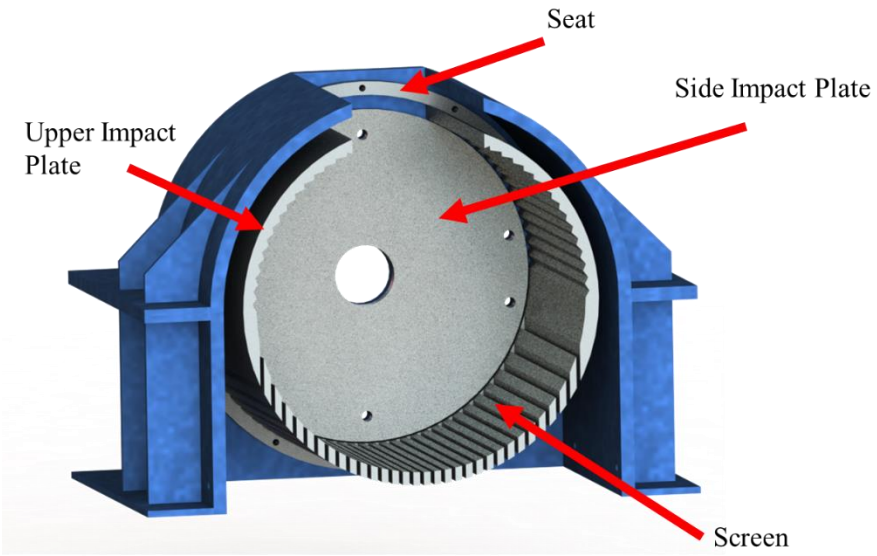

Figure 52. Hammer Mill Crusher Crushing Chamber

What makes the design of the crushing chamber unique is its fully disassemblable without the need to cut any welds. By unbolting the highlighted bolts shown in Figure 53, all components of the crushing chamber can be removed from the housing. The upper impact plates and the screen are secured in a 11mm groove between the seat and the side impact plates, preventing movement. However, once the housing is disassembled as illustrated in Figure 53, and the side impact plates are unbolted, both the screen and the upper impact plates can be easily removed. This design simplifies inspection and maintenance, eliminating the need to cut welds for disassembly.

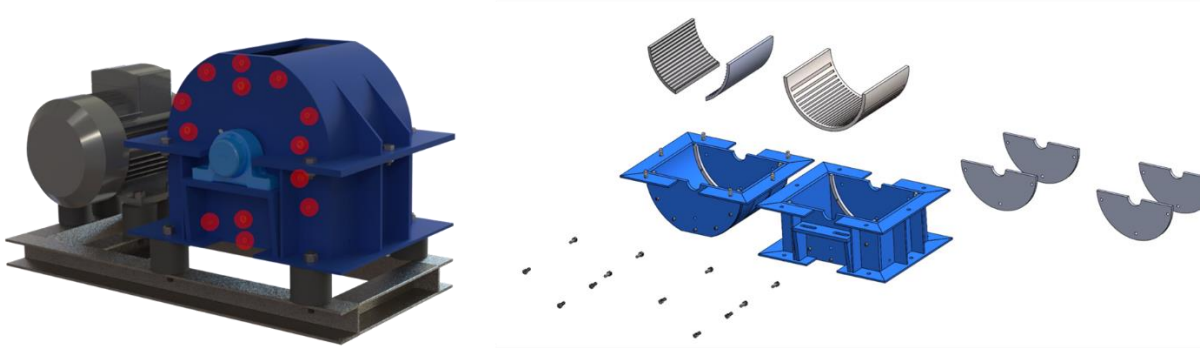

Figure 53. Hammer Mill Crusher Crushing Chamber Disassembling, highlighted on the left Figure are the bolts needed to be unbolted before components of the crushing chamber can be removed. On the right image is the components of the crushing chamber after being removed.

7.2.1.2 Hammer and Shaft Connection

Similar to the crushing chamber, the design goal for the hammer and shaft assembly in the Hammer Mill Crusher was to create a mechanism that avoids the need for cutting welds during maintenance. Unlike standard designs where the discs that hold the hammers and the shaft are typically welded together, in this design, the discs and shaft are connected by a key inserted into keyways on both the discs and the shaft. To secure the assembly and prevent the key from coming loose during operation, two nuts on either end of the shaft are tightened. This setup ensures that the shaft can rotate at 600 rpm without any issues, while also making maintenance easier.

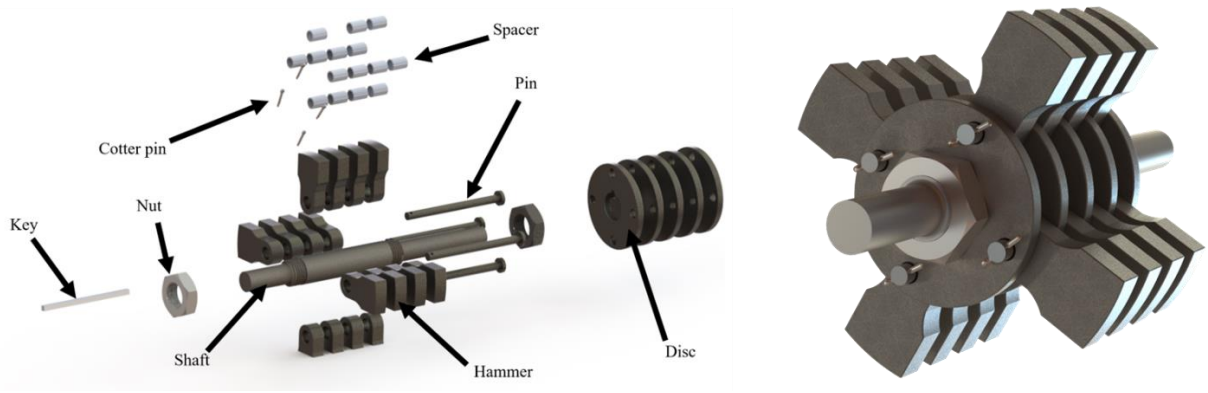

Figure 54. Hammer Mill Crusher Shaft and Hammer

7.2.2 Calculations

The design of the Hammer Mill Crusher was less complex compared to the Jaw Crusher since it required fewer calculations. For the Hammer Mill Crusher, attempting to simulate the crushing process through calculations was not pursued, as no calculations were found that could simulate the process. Therefore, the design validation relied on observational data from videos of similar machines in operation and an engineering logic since the Hammer Mill Crusher operates with the hammers rotating at a speed of 600 rpm. Each hammer weighs 520 grams, which is significantly more than the rocks it impacts, which only weigh about 10 grams. This weight difference ensures that the hammers exert the necessary force to break the rocks.

Calculations to assess the durability of the drive shaft for the Hammer Mill Crusher were performed in the same manner as those for the Jaw Crusher. The Goodman Factor of Safety was calculated at the shoulders of the shaft where the diameter changes. These areas are critical as it typically experiences the highest stress concentration, making it an important point for evaluating the shaft's ability to withstand operational stresses.

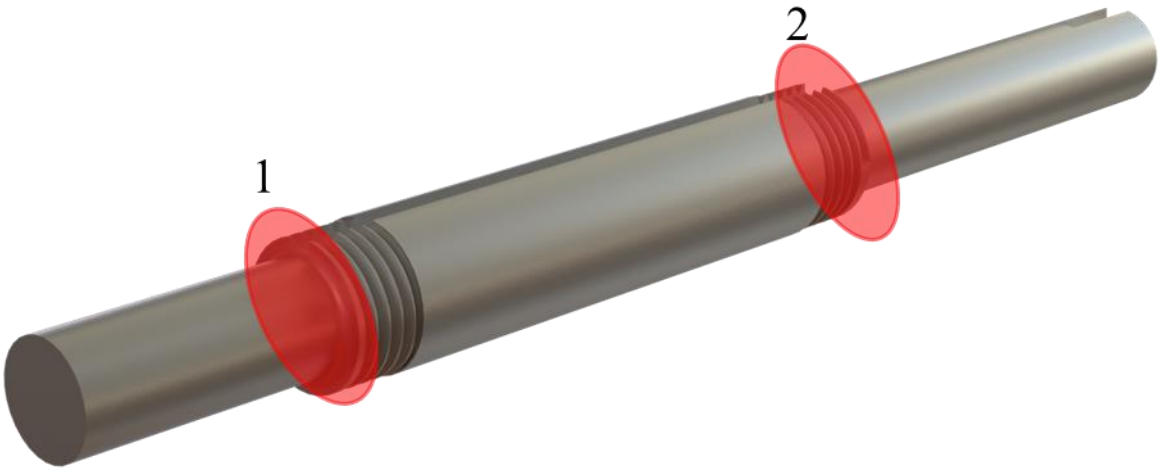

Figure 55. The Driving Shaft for the Hammer Mill Crusher

The calculations revealed that the Goodman Factor of Safety for Shoulder 1 of the Hammer Mill Crusher shaft was remarkably high at 12.17, predicting an infinite operational life. Similarly, for Shoulder 2, the Factor of Safety was calculated at 5.57, also suggesting an infinite lifecycle. The calculations indicated that the shaft's diameter could be reduced since they Factor of Safety values was higher than needed, doing so would necessitate a corresponding reduction in the keyway size. This change would increase stress concentrations within the keyway, for that reason it was decided to keep the diameter unchanged.

Two deep groove ball bearings are used to attach the shaft to the housing, requiring slope calculations to ensure good alignment. The calculations confirmed that the slope of the shaft remained below the maximum allowable limit of 0.003 radians as shown in Table 5 for the selected bearings across the entire length of the shaft. The Calculations to prove this can be found on the flash drive on the file "HammerMillGoodmanFOS.m"

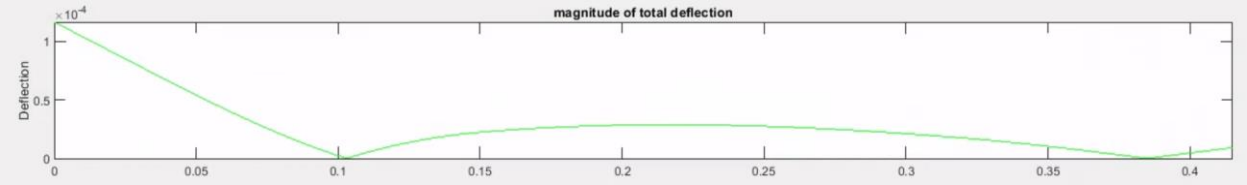

Figure 56. Slope Graph for Hammer Mill Crusher Driving Shaft

7.2.3 Stress in Components

Static simulations were conducted for the screen and the upper impact plate. The static simulation results indicated minimal wear on both the upper impact plates and the screen. Given the minimal wear observed in the static simulation, a fatigue simulation was deemed unnecessary.

- Boundary Condition: Back of plates
- Loading condition:
    - Front Plate: 3 kN

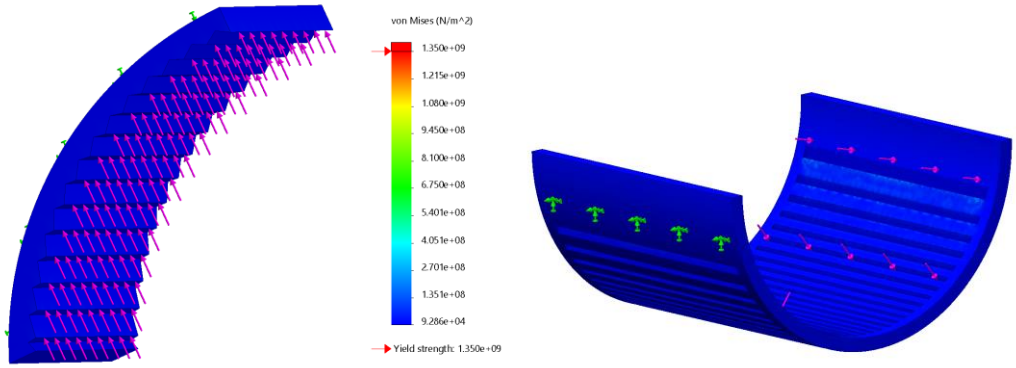

Figure 57. Static and Fatigue Results for Hammer Mill Impact Plates

Similarly, static and fatigue simulations were performed on a hammer. The static simulation revealed some wear on the corner subjected to load. The fatigue simulation was conducted and showed that the hammer sustained no damage after 60 million cycle loads.

- Boundary Condition: Walls of hole
- Loading condition:
    - Corner: 3 kN

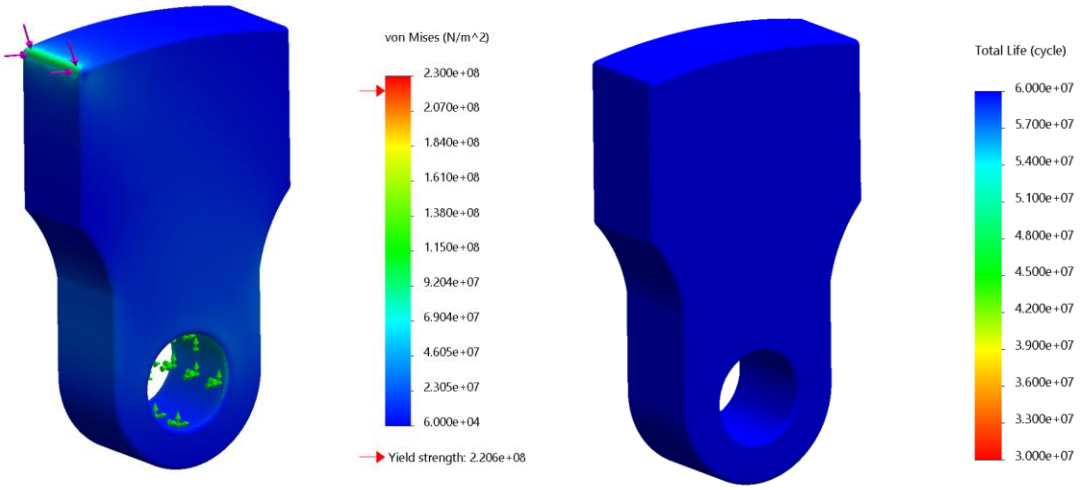

Figure 58. Von Mises Stress and Fatigue Results for a Hammer

The Hammer Mill Crusher design has shown it can theoretically crush lava rocks with a cross-sectional area of 2cm x 5cm. However, as noted in Section 5.2.1, there is a concern that clogging of the screen could be an issue. To mitigate potential clogging, the gaps on the screen will be set to 3000 micrometers instead of the initial 500 micrometers. This adjustment is made because the sand retains some moisture from the initial cleaning stage, which increases the likelihood of clogging.

To achieve the required grain size of 500 micrometers, a Sand Screening Machine will be used as the final step in the Lava Rock Crushing System. Any rocks that are larger than 500 micrometers after the initial pass through the system will be routed back through the crusher for further size reduction. This ensures that the final product consistently meets the specified grain size requirements.

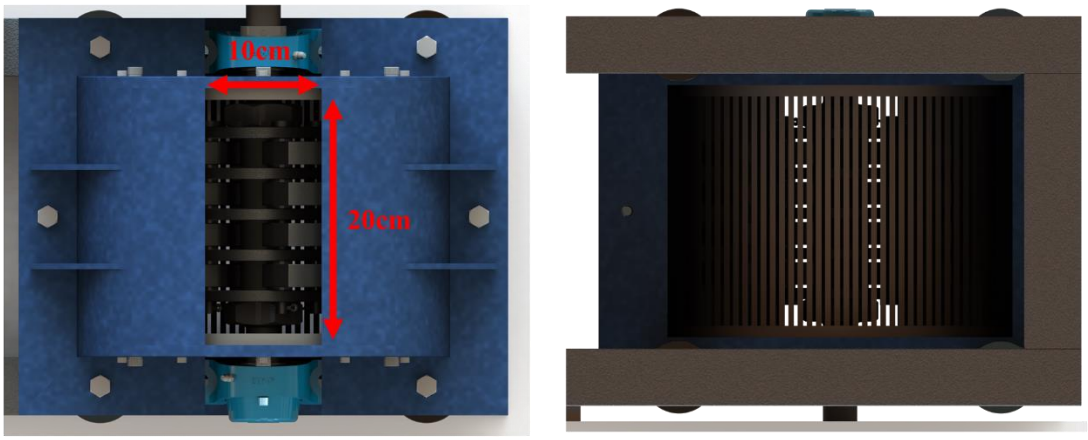

Figure 59. Top and Bottum view of the Hammer Mill Crusher showing the Max Input Size and the Screen

To direct the rocks from the Jaw Crusher to the Hammer Mill Crusher, a funnel will be mounted on top of the crusher. This funnel will be bolted to the Hammer Mill Crusher using existing holes that currently hold the seat. Similarly, another funnel will be installed beneath the Hammer Mill Crusher to channel the output directly into a collection container positioned below it. The sand collected in this container will then be manually loaded into the Sand Dryer for the final drying stage.

Just like the Jaw Crusher, all components of the Hammer Mill Crusher will be made from EN 10025 steel. However, given that the Hammer Mill Crusher experiences less force compared to the Jaw Crusher, its components will be fabricated from 10mm thick steel, except for the hammers, which will be made from 15mm thick EN 10025 steel.

All components will undergo sandblasting, priming, and painting to protect against corrosion. It is expected that the paint will eventually wear off inside the crushing chamber and that rust will develop over time. Given that the final product of the system must not include any rust, any components showing signs of rust will be disassembled, sandblasted, and repainted, as necessary. This maintenance procedure ensures the longevity of the Crusher while maintaining the quality of the processed sand.

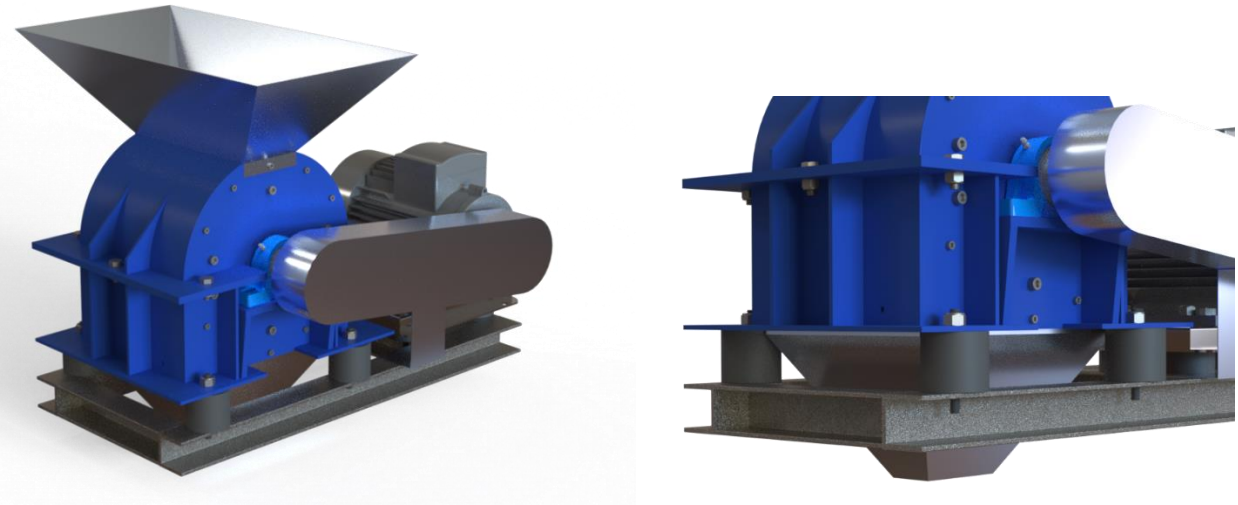

Figure 60. The Funnels Located on Top and Underneath the Hammer Mill Crusher

7.3 Crushers Support

The support structure for the crusher has two levels: the upper level is designed to hold the Jaw Crusher, while the lower level supports the Hammer Mill Crusher, positioned directly beneath the Jaw Crusher. This layout allows material exiting the Jaw Crusher to directly enter the Hammer Mill Crusher. The support structure is constructed from steel UPN 100 U channels, selected after a process of trial and error using SolidWorks static and fatigue simulations that are explained in the next paragraph. Previous iterations using UPN 50, UPN 65, and UPN 80 U channels were tested before settling on UPN 100, which provided the strength required for the structure.

To validate the design of this support system, the shaking force generated by the Jaw Crusher was calculated using the same four bar linkage calculations as for the Jaw Crusher calculations. The maximum shaking force was calculated to be 46kN at -16 degrees, to validate the design static and fatigue simulations were used.

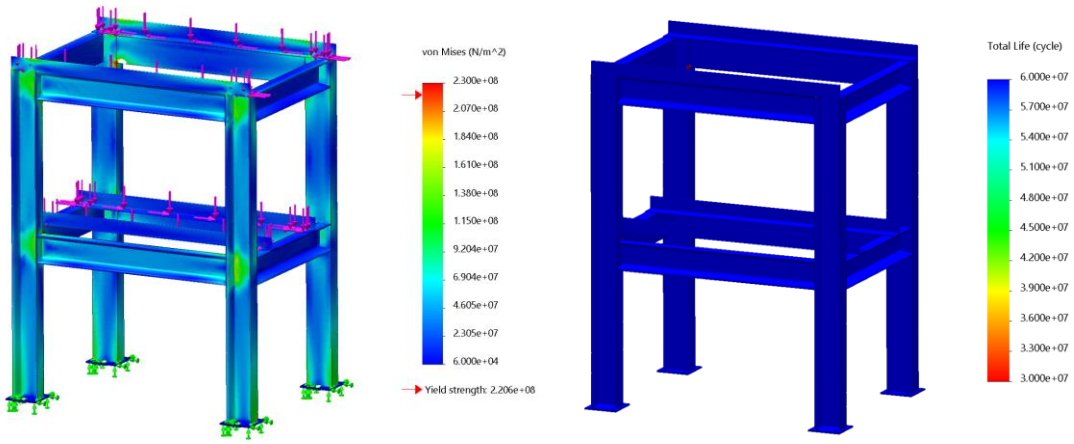

Figure 61. Static and Fatigue Plot of Crushers Support

The static analysis of the crusher support structure revealed that the highest stress concentrations occurred at the points where the U channels were welded together. Given the signs of wear indicated by the static load plot, a fatigue simulation was also performed to assess wear of the structure .The fatigue analysis showed some minimal wear after 30 million cycles of fully reversed loading.

7.4 Subsystem 3 – Sand Dryer

As outlined in Section 4.3, the design of the sand dryer for this system is inspired by the existing sand drying method used at the Blue Lagoon. The focus of this redesign is to enhance the efficiency of the current method, aiming to increase the capacity for drying more sand in a shorter amount of time.

7.4.1 Design

The redesign of the sand dryer uses the insulated container currently in use and three heating elements. These elements are hollow and designed to be heated by running hot water at approximately 80°C through them. Given the proximity of the Blue Lagoon to a geothermal power plant, which supplies the Blue Lagoon with hot water, there is no need for an additional boiler in this setup.

The heating elements will be made from 316 stainless steel, chosen for its excellent corrosion resistance properties. This material selection eliminates the need for any additional protective coatings.

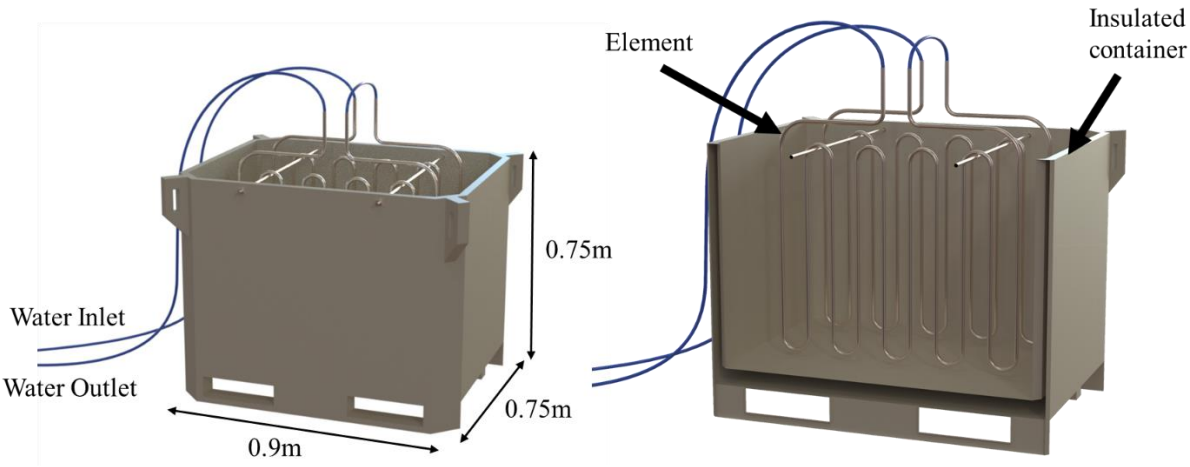

Figure 62. Final Design of the Sand Dryer

7.4.2 Calculations

To determine the drying time for the redesigned sand dryer, a model of the container was divided into 400 sections, as shown in Figure 63. The initial moisture level of the sand was estimated to be 10% from the initial process step where the raw lava rocks are pressure washed.

First the temperature distribution from the three heating elements to each section over a 24-hour period was calculated, results from the calculation can be seen in Figure 64. The results show that the sections furthest away from the element only heat up to 64°C after 24 hours and uniform temperature for the whole container theoretically not possible within that time frame.

Following this, the heat delivered to each section was calculated, this was done to see if the heat radiated from the element would be enough to evaporate the moisture from the sand in each section. The heat in each section was then compared to the amount of heat required to evaporate water from the sand, considering the volume of each section. Calculations to show this can be found in Appendix C

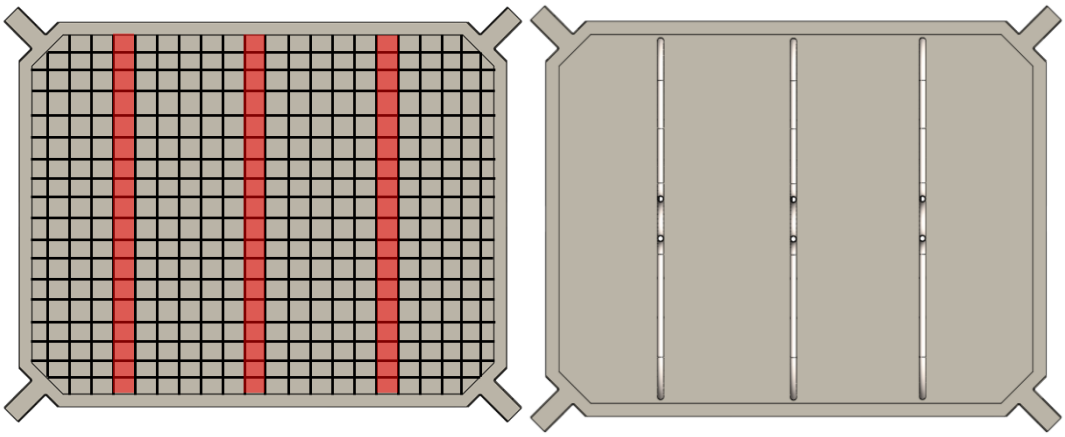

Figure 63. Sections of the Container and Placement of the Elements in the Container

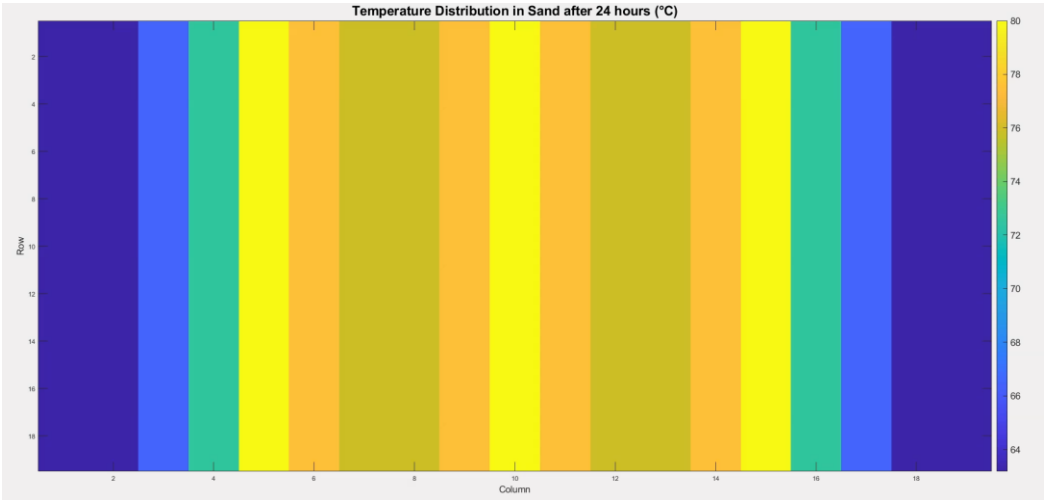

Figure 64. Temperature Distribution Across the Container in 24 Hours

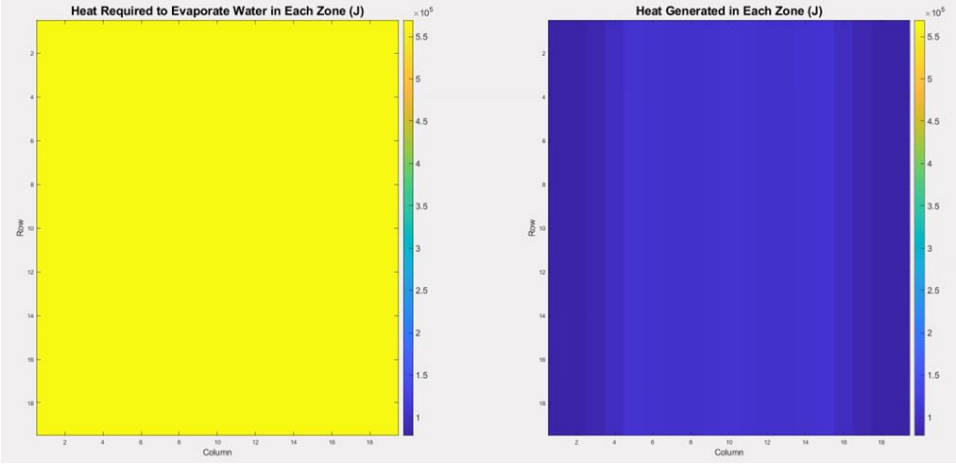

Figure 65. Heat Required per Section and Calculated Heat per Section

As indicated by the plot in Figure 65, the heat distributed to each section was theoretically insufficient to vaporize the moisture from the sand. Interestingly, the current operational method, which uses a single heating element inserted directly into the sand, has been effective. Although it was not proven through theoretical calculations that the redesigned system with three elements will be more efficient, it is reasonable to assume that it could enhance the drying process given the increased number of heat sources. However, without further experimental data it is not possible to accurately calculate the time required to dry the entire container with the new design.

8 Budget

A rough estimation of the cost to build each subsystem was calculated. Notably, this estimate does not include the expenses related to welding and assembly work. The exclusion of these costs is due to the fact that the maintenance department at the Blue Lagoon already has a welder who will handle all welding and assembly tasks. What is also not included in this estimate is a sand screening machine, and a pressure washer. The sand screening machine is already available, as it is being used in the current method and there are several pressure washers available for use in this project at the Blue Lagoon. As for the conveyor, after reviewing options from various vendors, the cost of a suitable conveyor for the project was estimated at around $6,000.00.

Table 6. Jaw Crusher Cost

Part	Qty	Total Price
EN 10025 15mm Steel Sheet - 1,000x2,000mm	1	$ 900.00
Water Cutting	1	$ 400.00
Impact Plate Fabrication	2	$ 400.00
65mm Shaft - 800mm	1	$ 235.00
Driving Shaft Fabrication	1	$ 250.00
40mm Shaft - 350mm	2	$ 45.00
Shaft Fabrication	2	$ 50.00
55mm Bearing - Housed Deep Groove Ball Bearing	2	$ 200.00
65mm Bearing - Roller Bearing	2	$ 240.00
Hardware (Bolts, Nuts and Retainer Rings)	1	$ 50.00
300mm Pulley and Taper Bush	1	$ 70.00
100mm Pulley and Taper Bush	1	$ 50.00
Motor	1	$ 800.00
M12 Motor Mount	8	$ 240.00
Motor Base	1	$ 80.00
U Beam - 4,200mm	1	$ 300.00
Sandblasting	1	$ 100.00
Primer and Paint	1	$ 100.00
		$ 4,510.00

Table 7. Hammer Mill Crusher Cost

Part	Qty	Total Price
EN 10025 10mm Steel Sheet - 1,000x2,000mm	1	$ 440.00
Water Cutting	1	$ 400.00
Impact Plate Fabrication	2	$ 400.00
30mm Shaft - 450mm	1	$ 80.00
Driving Shaft Fabrication	1	$ 250.00
20mm Shaft - 200mm	4	$ 40.00
Shaft Fabrication	4	$ 200.00
30mm Bearing - Housed Deep Groove Ball Bearing	2	$ 70.00
Hardware (Bolts, Nuts, Cotter Pin, Key)	1	$ 50.00
100mm Pulley and Taper Bush	2	$ 50.00
Motor	1	$ 800.00
M12 Motor Mount	4	$ 120.00
Motor Base	1	$ 80.00
U Beam - 2,400mm	1	$ 200.00
Sandblasting	1	$ 100.00
Primer and Paint	1	$ 100.00
		$3,380.00

Table 8. Crusher Support Cost

Part	Qty	Total Price
U Beam - 10,200mm	1	$ 800.00
Angle Iron - 3,900mm	1	$ 150.00
Sandblasting	1	$ 200.00
Primer and Paint	1	$ 200.00
		$1,350.00

Table 9. Sand Dryer Cost

Part	Qty	Total Price
20mm 316 Stainless Steel Tube - 6,000mm	1	$ 700.00
Element Fabrication	3	$ 200.00
Water Hose	1	$ 150.00
Hose Fittings	6	$ 100.00
316 Stainless Steel M10 Partially Threaded Rod - 1,200mm	2	$ 70.00
		$1,220.00

Table 10. Funnels and Shields Cost

Part	Qty	Total Price
2mm Aluminum Sheet	1	$ 200.00
Funnel Fabrication	4	$ 200.00
Shield Fabrication	2	$ 200.00
		$ 600.00

Table 11. Cost of the Designed System

Subsystem	Cost
Jaw Crusher	$ 4,510.00
Hammer Mill Crusher	$ 3,380.00
Crushers Support	$ 1,350.00
Sand Dryer	$ 1,220.00
Funnels and Shield	$ 600.00
	$ 11,060.00

Table 12. Total Cost of the Lava Rock Crushing System

Subsystem	**Cost**
Jaw Crusher	$ 4,510.00
Hammer Mill Crusher	$ 3,380.00
Crushers Support	$ 1,350.00
Sand Dryer	$ 1,220.00
Funnels and Shield	$ 600.00
Screen Machine	$ -
Pressure Washer	$ -
Coveyor	$ 6,000.00
	$ 17,060.00

As shown in Table 12, the total cost of the system was under the $30,000.00 budget requirement. Considering this was a rough estimate, it is reasonable to add an extra $2,000.00 to cover unforeseen expenses, such as higher fabrication costs or the need to purchase more expensive parts if the originally planned ones are unavailable, making the total cost $19,060.00 for Lava Rock Crushing System.

9 Feasibility Study

To assess the economic viability of the project, an economic analysis was performed. First, the cost of the current process over a ten-year period was calculated. This included the cost and shipping per kilogram of sand which was determined to be $0.47 per kilogram. Given that approximately 1500 kilograms of lava sand are used annually in production, this rate was multiplied by 1500 kilograms to estimate the annual cost.

For the proposed design, the $19,060.00 setup cost of the system was considered the first-year cost. An additional $300.00 was projected for each subsequent year to cover estimated maintenance expenses, including repainting, bearing replacements, and other potential part failures.

The results from the economic analysis revealed that the return on investment period for the proposed design is approximately 7.5 years. These findings are detailed in Table 13, which compares the total costs for both the current process, which involves purchasing sand, and the proposed system over 10 years.

Table 13. Cost per Year Over a 10 Year Period

Year	Cost of Current Process	Cost of Proposed Design
1	$ 2,784.97	$ 19,060.00
2	$ 5,569.94	$ 19,360.00
3	$ 5,569.94	$ 19,660.00
4	$ 11,139.89	$ 19,960.00
5	$ 13,924.86	$ 20,260.00
6	$ 16,709.83	$ 20,560.00
7	$ 19,494.80	$ 20,860.00
8	$ 22,279.77	$ 21,160.00
9	$ 25,064.74	$ 21,460.00
10	$ 27,849.71	$ 21,760.00

10 System Overview

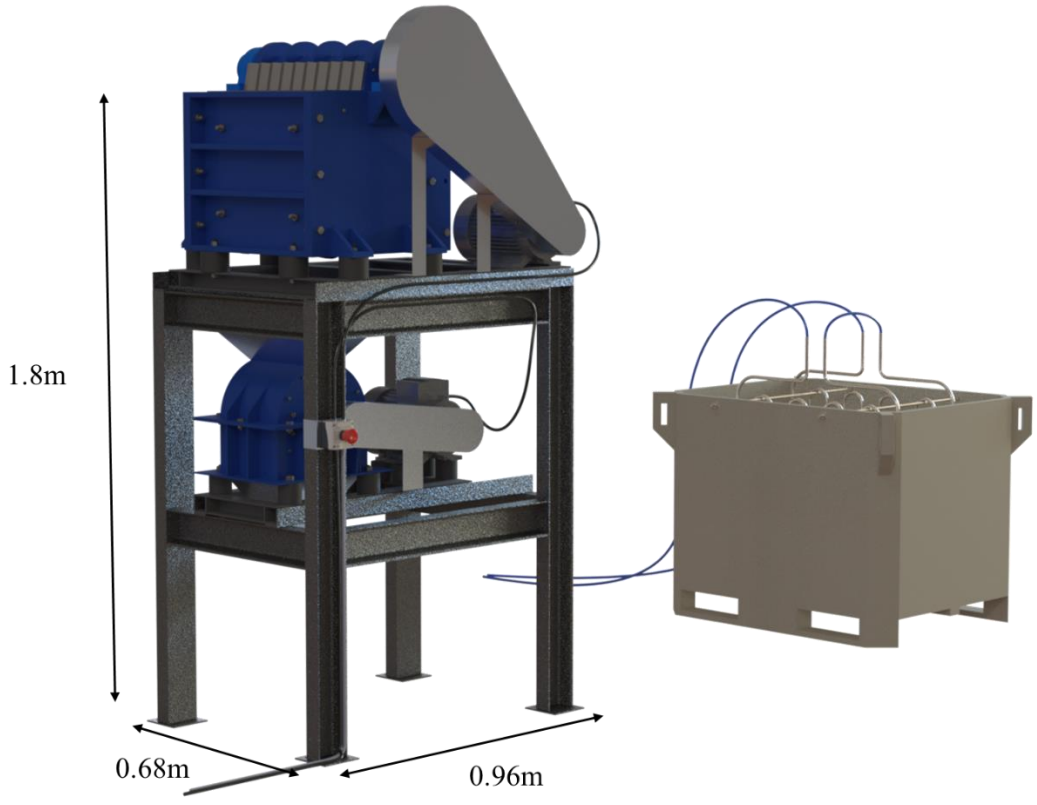

Figure 66. Figure Showing the Jaw Crusher, Hammer Mill Crusher, Crushers Support, and the Sand Dryer

The initial design requirement for the system was to process lava rocks with a cross-section of 20cm x 50cm. This specification has been successfully met, as the opening gap of the Jaw Crusher is fixed to 20cm x 50cm, as detailed in Figure 50. Furthermore, to address the output size requirements and prevent clogging issues, the screen on the Hammer Mill Crusher was designed with gap 3000 micrometers width, rather than the initially specified 500 micrometers.

Instead of achieving the final desired size directly from the Hammer Mill Crusher, the output will be processed through a sand screening machine as the final step in the system. This decision was influenced by the availability of an existing sand screening machine at the Blue Lagoon, which currently screens the sand used in their operations.

An important requirement, given the corrosive nature of the area, was to ensure that the subsystems are resistant to corrosion for at least three years. This was achieved by sandblasting, priming, and painting all steel components. To maintain this level of protection, the paint will need to be reapplied every three years, or more frequently if necessary.

For operational safety, the system includes shields covering the belts and pulleys to prevent accidental entanglement and also an emergency stop button to quickly stop all operation of the Crushers in case of emergency. Additionally, the Hammer Mill Crusher is equipped with funnels over the input and output areas. The Jaw Crusher's opening is situated at a height of 1.8 meters, making it difficult to accidentally place hands near the crushing mechanism. It has also been shown both by simulations and calculations that all systems are capable of performing under the loads acting on them.

Concerning the Sand Dryer, the top parts of the heating elements are exposed and not covered by sand, posing a risk of burning. To mitigate this, the exposed parts of the elements will be insulated to prevent any potential heat-related hazards. This ensures that all components of the system adhere to safety standards and reduce the risk of operational accidents.

As for the operational efficiency the system is semi-autonomous since it involves some manual labor but also mechanical systems and gravity. The initial step involves manually pressure washing the lava rocks. Once cleaned, the rocks are loaded onto a conveyor that transports them to the crushers. Using gravity, the rocks pass through both the Jaw Crusher and

the Hammer Mill Crusher and then fall into a collection container positioned below the Hammer Mill Crusher.

The next step requires manual labor to transfer the sand from the collection container to the sand dryer. The final step in the process involves manually loading the dried sand from the sand dryer into the sand screening machine.

The final requirement for the project was to keep the total cost of the system under $30,000.00. This target was successfully met, as detailed in Section 8 of the documentation. It was also demonstrated that the return on investment period for the system is approximately 7.5 years.

11 Conclusion

In conclusion, this theoretical design for Blue Lagoon to internally produce lava sand from local lava rocks has successfully met the project's outlined objectives. Designed to improve sustainability and operational efficiency, this semi-autonomous system combines washing, crushing, and drying processes to ensure a consistent supply of lava sand and reduce reliance on external sources.

The design process was carefully documented, detailing every step from Concept sketches to the final design. Several engineering challenges were addressed with innovative solutions, including the unique designs of the Jaw and Hammer Mill Crushers, such as bolted connection for ease of maintenance and replaceable discs and hammers. These designs were specifically adapted to handle the corrosive conditions of the Blue Lagoon environment.

Moreover, the project demonstrated financial feasibility, achieving a calculated return on investment within 7.5 years. Additionally, the total cost of the system was under the allocated budget of $30,000.

References

[1] "Blue Lagoon Skin Care: Söguágrip." *Blue Lagoon Iceland*, 30 Oct. 2019, https://www.bluelagoon.com/is/sogur/blue-lagoon-skin-care-soguagrip. Accessed 3 Oct. 2023.

[2] "Sjálfbærni í Bláa Lóninu." *Blue Lagoon Iceland*, 2 Mar. 2022, www.bluelagoon.com/is/sogur/sjalfbaerni-i-blaa-loninu. Accessed 3 Oct. 2023.

[3] "Bláa Lónið." *Blue Lagoon Iceland*, www.bluelagoon.com/is/heimsokn/blaa-lonid. Accessed 3 Oct. 2023.

[4] "American Fire Glass 10-Pound Black Lava Rock, XXL 4-6 Inch." *Fireplacesdirect.com*, www.fireplacesdirect.com/american-fire-glass-10-pound-black-lava-rock-xxl-4-6-inch.html?msclkid=75d922bb5a67153dde4747a428fd63b0&utm_source=bing&utm_medium=cpc&utm_campaign=**LP%20-%20Shop%20-%20Accessories&utm_term=4587299958867974&utm_content=Fireplace%20Enhancements. Accessed 5 Oct. 2023.

[5] "Zealous Photography." *Zealousphotography.Wordpress.Com*, 17 Mar. 2014, zealousphotography.wordpress.com/2014/03/17/lava-field-formation-over-the-blue-lagoon-iceland/. Accessed 5 Oct. 2023.

[6] "ISO 12100:2010, Safety of Machinery - General Principles for Design - Risk Assessment and Risk Reduction." *International Organization for Standardization*, Nov. 2010, www.iso.org/standard/51528.html.

[7] "What Type of Crusher Is Best for Primary Crushing?" *Mclanahan*, 25 Mar. 2021, www.mclanahan.com/blog/what-type-of-crusher-is-best-for-primary-crushing. Accessed 29 Mar. 2024.

[8] Moore, Paul. "FLSmidth to Provide Gyratory Crushers and Apron Feeders to Copper and Gold Mine in Chile." *International Mining*, 25 Mar. 2021, im-mining.com/2021/03/25/flsmidth-provide-gyratory-crushers-apron-feeders-copper-gold-mine-chile/. Accessed 29 Mar. 2024.

[9] "Everything You Need to Know About Rock Crushers." *Kemper Equipment*, n.d., www.kemperequipment.com/blog/rock-crushers-everything-you-need-to-know/. Accessed 29 Mar. 2024.

[10] "Cone Crusher Applications." *Blue Group*, 19 Nov. 2019, blue-group.com/news/news-articles/cone-crusher-applications/. Accessed 29 Mar. 2024.

[11] "The Difference Between Single Toggle and Double Toggle Jaw Crushers." *Recycling Equipment Reviews*, n.d., recyclingequipmentreviews.com/blog/the-difference-between-single-toggle-and-double-toggle-jaw-crushers/. Accessed 29 Mar. 2024.

[12] Michaud, David. "Difference Between Single & Double Toggle Jaw Crusher." *911 Metallurgist*, 20 Sept. 2014, www.911metallurgist.com/blog/difference-between-single-double-toggle-jaw-crusher. Accessed 29 Mar. 2024.

[13] "Downstream Crushing Options for Secondary, Tertiary and Quaternary Crushing." *Mclanahan*, 12 Apr. 2021, www.mclanahan.com/blog/downstream-crushing-options-for-secondary-tertiary-and-quaternary-crushing. Accessed 29 Mar. 2024.

[14] Rajput, Sunderveer. "Should Know All About Stone Crusher Plant." *Machine Thug*, n.d., machinethug.com/stone-crusher-plant/. Accessed 29 Mar. 2024.

[15] "Hammer Mill Crushers." *Stedman Machine*, n.d., www.stedman-machine.com/hammer-mill-crushers.html. Accessed 29 Mar. 2024.

[16] Jordan. "Hammer Mill Crushers." *FTM Machinery*, 15 Feb. 2023, www.ftmmachinery.com/blog/what-are-the-differences-between-the-7-types-of-crushers.html. Accessed 29 Mar. 2024.

[17] "Full Circle Hammer Mill." *Stedman Machine*, n.d., https://www.stedman-machine.com/full-circle-hammer-mill.html. Accessed 29 Mar. 2024.

[18] Cindy. "How To Choose A Suitable Sand Dryer?" *Mortar Plant*, 11 Aug. 2023, www.mortarplant.com/choose-suiTable-sand-dryer/. Accessed 29 Mar. 2024.

[19] "Jaw Crusher." *Cement Plant Equipment*, n.d., www.cementplantequipment.com/products/crushing-mill/jaw-crusher/. Accessed 5 Apr. 2024.

[20] "HOW KEESTRACK JAW CRUSHERS WORK." *Equip2 Processing Solution*, 24 Sept. 2019, www.equip2.co.nz/post/how-a-keestrack-jaw-crusher-works. Accessed 5 Apr. 2024.

[21] "Hammer Crusher." *HXJQ*, n.d., www.hxjqchina.com/pro/hammer_crusher.html. Accessed 7 Apr. 2024.

[22] Deepak, B. "Optimum Design and Analysis of (the) Swinging Jaw Plate of a Single Toggle Jaw Crusher." ResearchGate, 2010, p. 10, doi:10.13140/RG.2.1.1369.2880.

[23] Budynas, R. G., Nisbett, J. K., & Shigley, J. E. (2020). Shigley's Mechanical Engineering Design 6th ED. McGraw-Hill Education

[24] "Telsmith Stationary Jaw Crushers." *Manuquipinc*, n.d., manuquipinc.com/en/produit/telsmith-stationary-jaw-crushers/. Accessed 7 Apr. 2024.

[25] Clout, J.M.F., and J.R. Manuel. "2 - Mineralogical, Chemical, and Physical Characteristics of Iron Ore." Iron Ore, edited by Liming Lu, Woodhead Publishing, 2015, pp. 45-84, ISBN 9781782421566. https://doi.org/10.1016/B978-1-78242-156-6.00002-2.

[26] Norton, Robert L. (2020). Design of machinery : an introduction to the synthesis and analysis of mechanisms and machines 6th ED. McGraw-Hill Education.

.

APPENDIX

Appendix A: Four-bar Linkage Calculations

Appendix B: Four-bar Linkage Calculations MATLAB code - "JawCrusherConceptOneForces.m."

Appendix C: Jaw Crusher Goodman Factor of Safety Calculations MATLAB code – "JawCrusherConceptOneGoodmanFOS.m"

Appendix D: Hammer Mill Crusher Goodman Factor of Safety Calculations MATLAB code: "HammerMillGoodmanFOS.m"

Appendix E: Sand Dryer Heat Calculations MATLAB code – "SandDryerHeat.m"

Appendix F: Free Body Diagram of Jaw Crusher Shaft

Appendix G: Free Body Diagram of Hammer Mill Crusher Shaft

Appendix H: Weight Table

Appendix I: Functional Block Diagram

Appendix J: ABET Outcome 2, Design Factor Considerations

APPENDIX A

Four Bar Linkage Calculations

Following equations and Figures are from the book DESIGN OF MACHINERY: AN INTRODUCTION TO THE SYNTHESIS AND ANALYSIS OF MECHANISMS AND MACHINES **[25]**

For when $\theta_{2,local} = 207.4°$

$a = Length\ of\ Link\ 1 = 37.5\text{mm}$

$b = Length\ of\ Link\ 2 = 447.1mm$

$c = Length\ of\ Link\ 3 = 140mm$

$d = Length\ of\ Link\ 4 = 360.5mm$

$\theta_{2,local} = 207.4° = 3.62rad$

$\omega_2 = -20\ {}^{rad}/_{s}$

$\alpha_2 = 0\ {}^{rad}/_{s^2}$

$R_{PA1} = 176.6mm$

$R_{PA1} = 260mm$

$R_{PA1} = 352.2mm$

$R_{PA1} = 447.7mm$

$R_{PA1} = 544.8mm$

$\theta_3 + \delta_{3,P1} = 59.8° = 1.04rad$

$\theta_3 + \delta_{3,P2} = 45° = 0.78rad$

$\theta_3 + \delta_{3,P3} = 37.6° = 0.66rad$

$\theta_3 + \delta_{3,P4} = 33.3° = 0.58rad$

$$\theta_3 + \delta_{3,P5} = 30.6° = 0.53rad$$

$$K_1 = \frac{d}{a} = \frac{360.5}{37.5} = 9.61 \tag{1}$$

$$K_2 = \frac{d}{c} = \frac{360.5}{140} = 2.58 \tag{2}$$

$$K_3 = \frac{a^2 - b^2 + c^2 + d^2}{2ac} = \frac{37.5^2 - 447.1^2 + 140^2 + 360.5^2}{2 * 37.5 * 140} = -4.66 \tag{3}$$

$$K_4 = \frac{d}{b} = \frac{360.5}{447.1} = 0.81 \tag{4}$$

$$K_5 = \frac{c^2 - d^2 - a^2 - b^2}{2ab} = \frac{140^2 - 360.5^2 - 37.5^2 - 447.1^2}{2 * 37.5 * 447.1} = -9.29 \tag{5}$$

$$A = \cos(\theta_2) - K_1 - K_2\cos(\theta_2) + K_3 = \cos(3.62) - 9.61 - 2.58 * \cos(3.62) - 4.66 = -12.87 \tag{6}$$

$$B = -2\sin(\theta_2) = -2 * \sin(3.62) = 0.92 \tag{7}$$

$$C = K_1 - (K_2 + 1)\cos(\theta_2) + K_3 = 9.61 - (2.58 + 1) * \cos(3.62) - 4.66 = 8.12 \tag{8}$$

$$D = \cos(\theta_2) - K_1 + K_4\cos(\theta_2) + K_5 = \cos(3.62) - 9.61 + 0.81 * \cos(3.62) - 9.29 = -20.51 \tag{9}$$

$$E = -2\sin(\theta_2) = -2 * \sin(3.62) = 0.92 \tag{10}$$

$$F = K_1 + (K_4 - 1)\cos(\theta_2) + K_5 = 9.61 + (0.81 - 1) * \cos(3.62) - 9.29 = 0.49 \tag{11}$$

$$\theta_4 = 2\arctan\left(\frac{-B - \sqrt{B^2 - 4AC}}{2A}\right) = 2\arctan\left(\frac{-0.92 - \sqrt{0.92^2 - 4 * (-12.87) * 8.12}}{2 * (-12.87)}\right) = 1.39rad \tag{12}$$

$$\theta_3 = 2\arctan\left(\frac{-E - \sqrt{E^2 - 4DF}}{2D}\right) = 2\arctan\left(\frac{-0.92 - \sqrt{0.92^2 - 4 * (-20.51) * 0.49}}{2 * (-20.51)}\right) = 0.35rad \tag{13}$$

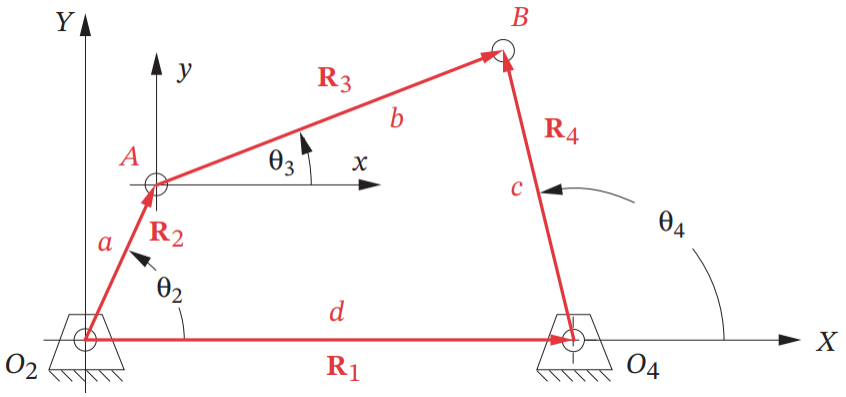

$$\omega_3 = \frac{a\omega_2}{b} * \frac{\sin(\theta_4 - \theta_2)}{\sin(\theta_3 - \theta_4)} = \frac{37.5 * (-20)}{447.1} * \frac{\sin(1.39 - 3.62)}{\sin(0.35 - 1.39)} = -1.54\,{}^{rad}/_{s}$$

$$\omega_4 = \frac{a\omega_2}{c} * \frac{\sin(\theta_2 - \theta_3)}{\sin(\theta_4 - \theta_3)} = \frac{37.5 * (-20)}{140} * \frac{\sin(3.62 - 0.35)}{\sin(1.39 - 0.35)} = 0.77\,{}^{rad}/_{s}$$

$$V_A = a\omega_2(-sin\theta_2 + jcos\theta_2) = 37.5 * (-20) * \left(-sin(3.62) + jcos(3.62)\right)$$
$$= -345.15 + 665.86j\ mm/s$$

$$V_{BA} = b\omega_3(-sin\theta_3 + jcos\theta_3) = 447.1 * (-1.54) * \left(-sin(0.35) + jcos(0.35)\right)$$
$$= 238.58 - 646.03j\ mm/s$$

$$V_B = c\omega_2(-sin\theta_4 + jcos\theta_4) = 140 * (-20) * \left(-sin(1.39) + jcos(1.39)\right)$$
$$= -106.57 + 19.84j\ mm/s$$

$$V_{PA1} = R_{PA1}\omega_3\left(-\sin\left(\theta_3 + \delta_{3,P1}\right) + jcos\left(\theta_3 + \delta_{3,P1}\right)\right)$$
$$= 176.6 * (-1.54) * \left(-sin(1.04) + jcos(1.04)\right) = 235.1 - 136.83j\ mm/s$$

$$V_{P1} = V_{PA1} + V_A = -110.05 + 529.03j\ mm/s$$

$$V_{PA2} = R_{PA2}\omega_3\left(-\sin\left(\theta_3 + \delta_{3,P2}\right) + jcos\left(\theta_3 + \delta_{3,P2}\right)\right)$$
$$= 260 * (-1.54) * \left(-sin(0.78) + jcos(0.78)\right) = 283.18 - 283.18j\ mm/s$$

$$V_{P2} = V_{PA2} + V_A = -61.96 + 382.67j\ mm/s$$

$$V_{PA3} = R_{PA3}\omega_3\left(-\sin\left(\theta_3 + \delta_{3,P3}\right) + jcos\left(\theta_3 + \delta_{3,P3}\right)\right)$$
$$= 352.2 * (-1.54) * \left(-sin(0.66) + jcos(0.66)\right) = 331.0 - 429.81j\ mm/s$$

$$V_{P3} = V_{PA3} + V_A = -14.14 + 236.04j\ mm/s$$

$$V_{PA4} = R_{PA4}\omega_3\left(-\sin(\theta_3 + \delta_{3,P4}) + jcos(\theta_3 + \delta_{3,P4})\right)$$
$$= 447.7 * (-1.54) * \left(-sin(0.58) + jcos(0.58)\right) = 378.60 - 576.37j\ mm/s$$

$$V_{P4} = V_{PA4} + V_A = 33.45 + 89.49j\ mm/s$$

$$V_{PA5} = R_{PA5}\omega_3\left(-\sin(\theta_3 + \delta_{3,P5}) + jcos(\theta_3 + \delta_{3,P5})\right)$$
$$= 544.8 * (-1.54) * \left(-sin(0.53) + jcos(0.53)\right) = 427.16 - 722.30j\ mm/s$$

$$V_{P5} = V_{PA5} + V_A = 82.01 - 56.44j\ mm/s$$

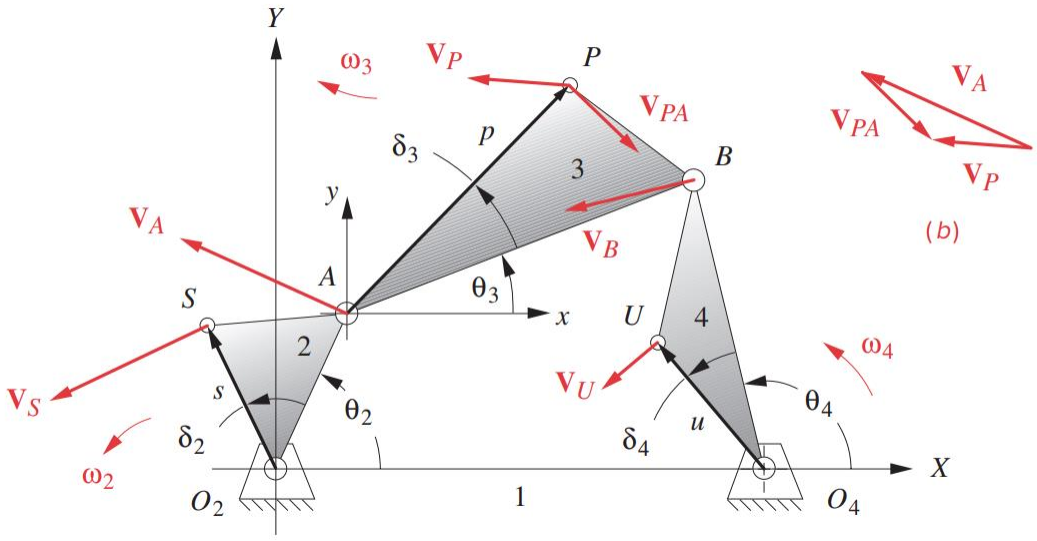

$$A = c\ sin(\theta_4) = 140 * sin(1.39) = 137.63$$

$$B = b\ sin(\theta_3) = 447.1 * sin(0.35) = 154.89$$

$$C = a\alpha_2\sin\theta_2 + a\omega_2^2 cos\theta_2 + b\omega_3^2 cos\theta_3 - c\omega_4^2 cos\theta_4$$
$$= 37.5 * 0 * sin(3.62) + 37.5 * (-20)^2 * cos(3.62) + 447.1 * (-1.54)^2$$
$$* cos(0.35) - 140 * (0.77)^2 * cos(1.39) = -12{,}338$$

$$D = c\ cos(\theta_4) = 140 * sin(1.39) = 25.62$$

$$E = b\ cos(\theta_3) = 447.1 * cos(0.35) = 419.41$$

$$F = a\alpha_2\cos\theta_2 - a\omega_2^2 sin\theta_2 - b\omega_3^2 sin\theta_3 + c\omega_4^2 sin\theta_4$$
$$= 37.5 * 0 * cos(3.62) - 37.5 * (-20)^2 * sin(3.62) - 447.1 * (-1.54)^2$$
$$* sin(0.35) + 140 * (0.77)^2 * sin(1.39) = 6{,}618$$

$$\alpha_3 = \frac{CD - AF}{AE - BD} = \frac{-12{,}338 * 25.62 - 137.63 * 6{,}618}{137.63 * 419.41 - 154.89 * 25.62} = -22.82\,{}^{rad}/_{s^2}$$

$$\alpha_4 = \frac{CE - BF}{AE - BD} = \frac{-12{,}338 * 419.41 - 154.89 * 6{,}618}{137.63 * 419.41 - 154.89 * 25.62} = -115.32\,{}^{rad}/_{s^2}$$

$$A_A = a\alpha_2(-sin\theta_2 + jcos\theta_2) - a\omega_2^2(cos\theta_2 + jsin\theta_2)$$
$$= 37.5 * 0 * \big(-sin(3.62) + jcos(3.62)\big) - 37.5 * (-20)^2$$
$$* \big(cos(3.62) + jsin(3.62)\big) = 13{,}317 + 6{,}903j$$

$$A_{BA} = b\alpha_3(-sin\theta_3 + jcos\theta_3) - b\omega_3^2(cos\theta_3 + jsin\theta_3)$$
$$= 447.1 * (-22.82) * \big(-sin(0.35) + jcos(0.35)\big) - 447.1 * (-1.54)^2$$
$$* \big(cos(0.35) + jsin(0.35)\big) = 2{,}540 - 9{,}940j$$

$$A_B = c\alpha_4(-sin\theta_4 + jcos\theta_4) - c\omega_4^2(cos\theta_4 + jsin\theta_4)$$
$$= 140 * (-115.32) * \big(-sin(1.39) + jcos(1.39)\big) - 140 * (0.77)^2$$
$$* \big(cos(1.39) + jsin(1.39)\big) = 15{,}857 - 3{,}037j$$

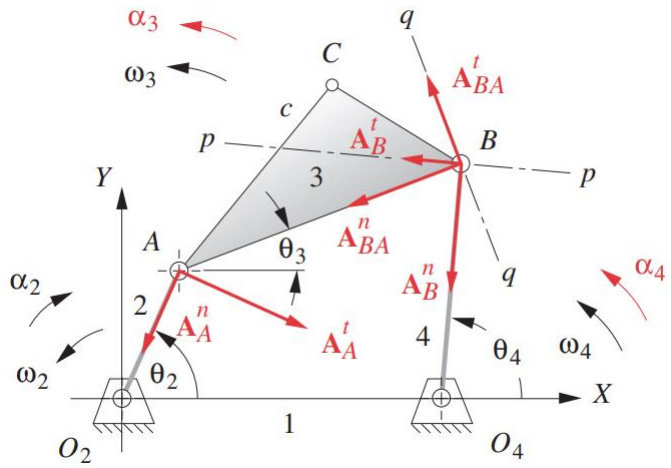

$$a_{tG2} = \alpha_2 * R_{CG2} = 0 * 8.5 = 0\,{}^{m}/_{s^2}$$

$$a_{rG2} = \omega_2^2 * R_{CG2} = -20^2 * 0.0085 = 3.4\,{}^{m}/_{s^2}$$

$$a_{G2x} = a_{tG2} * \cos\theta_2 - a_{rG2} * \sin\theta_2 = 0 * \cos(3.62) - 3.4 * \sin(3.62) = 1.56\,{}^{m}/_{s^2}$$

$$a_{G2y} = a_{tG2} * \sin\theta_2 + a_{rG2} * \sin\theta_2 = 0 * \sin(3.62) + 3.4 * \cos(3.62) = -3.02\,{}^{m}/_{s^2}$$

$$a_{tG3} = \alpha_3 * R_{CG3} = -22.82 * 0.26 = -5.95\,{}^{m}/_{s^2}$$

$$a_{rG3} = \omega_3^2 * R_{CG3} = -1.54^2 * 0.26 = 0.62\,{}^{m}/_{s^2}$$

$$a_{G3x} = a_{tG3} * \cos\theta_3 - a_{rG3} * \sin\theta_3 = -5.95 * \cos(0.35) - 0.62 * \sin(0.35) = -4.17\,{}^{m}/_{s^2}$$

$$a_{G3y} = a_{tG3} * \sin\theta_3 + a_{rG3} * \sin\theta_3 = -5.95 * \sin(0.35) + 0.62 * \cos(0.35) = -4.28\,{}^{m}/_{s^2}$$

$$a_{tG4} = \alpha_4 * R_{CG4} = -115.32 * 0.07 = -8.07\,{}^{m}/_{s^2}$$

$$a_{rG4} = \omega_4^2 * R_{CG4} = 0.77^2 * 0.07 = 0.04\,{}^{m}/_{s^2}$$

$$a_{G4x} = a_{tG4} * \cos\theta_4 - a_{rG4} * \sin\theta_4 = -8.07 * \cos(1.39) - 0.04 * \sin(1.39) = -1.52\,{}^{m}/_{s^2}$$

$$a_{G4y} = a_{tG4} * \sin\theta_4 + a_{rG4} * \sin\theta_4 = -8.07 * \sin(1.39) + 0.04 * \cos(1.39) = -7.93\,{}^{m}/_{s^2}$$

$$F_{12x} + F_{32x} = m_2 a_{G_{2x}}$$

$$F_{12y} + F_{32y} = m_2 a_{G_{2y}}$$

$$(R_{12x}F_{12y} - R_{12y}F_{12x}) + (R_{32x}F_{32y} - R_{32y}F_{32x}) = I_{G_2}\alpha_2 - T_{12}$$

$$F_{43x} - F_{23x} = m_3 a_{G_{3x}} - F_{P1x} - F_{P2x} - F_{P3x} - F_{P4x} - F_{P5x}$$

$$F_{43y} - F_{32y} = m_3 a_{G_{3y}} - F_{P1y} - F_{P2y} - F_{P3y} - F_{P4y} - F_{P5y}$$

$$(R_{43x}F_{43y} - R_{43y}F_{43x}) - (R_{32x}F_{32y} - R_{32y}F_{32x}) = I_{G_3}\alpha_3 - (R_{P1x}F_{P1y} - R_{P1y}F_{P1x}) - (R_{P2x}F_{P2y} - R_{P2y}F_{P2x}) - (R_{P3x}F_{P3y} - R_{P3y}F_{P3x}) - (R_{P4x}F_{P4y} - R_{P4y}F_{P4x}) - (R_{P5x}F_{P5y} - R_{P5y}F_{P5x}$$

$$F_{14x} + F_{43x} = m_4 a_{G_{4x}}$$

$$F_{14y} + F_{43y} = m_4 a_{G_{4y}}$$

$$(R_{14x}F_{14y} - R_{14y}F_{14x}) + (R_{34x}F_{34y} - R_{34y}F_{34x}) = I_{G_4}\alpha_4$$

$$\begin{bmatrix} 1 & 0 & 1 & 0 & 0 & 0 & 0 & 0 & 0 \\ 0 & 1 & 0 & 1 & 0 & 0 & 0 & 0 & 0 \\ -R_{12y} & R_{12x} & -R_{32y} & R_{32x} & 0 & 0 & 0 & 0 & 0 \\ 0 & 0 & -1 & 0 & 1 & 0 & 0 & 0 & 0 \\ 0 & 0 & 0 & -1 & 0 & 1 & 0 & 0 & 0 \\ 0 & 0 & R_{32y} & -R_{32x} & -R_{43y} & R_{43x} & 0 & 0 & 0 \\ 0 & 0 & 0 & 0 & -1 & 0 & 1 & 0 & 0 \\ 0 & 0 & 0 & 0 & 0 & -1 & 0 & 1 & 0 \\ 0 & 0 & 0 & 0 & R_{34y} & -R_{34x} & -R_{14y} & R_{14x} & 0 \end{bmatrix} \begin{bmatrix} F_{12x} \\ F_{12y} \\ F_{32x} \\ F_{32y} \\ F_{43x} \\ F_{43y} \\ F_{14x} \\ F_{14y} \\ 0 \end{bmatrix} =$$

$$\begin{bmatrix} m_2 a_{G_{2x}} \\ m_2 a_{G_{2y}} \\ I_{G_2}\alpha_2 - T_{12} \\ m_3 a_{G_{3x}} - F_{P1x} - F_{P2x} - F_{P3x} - F_{P4x} - F_{P5x} \\ m_3 a_{G_{3y}} - F_{P1y} - F_{P2y} - F_{P3y} - F_{P4y} - F_{P5y} \\ I_{G_3}\alpha_3 - (R_{P1x}F_{P1y} - R_{P1y}F_{P1x}) - (R_{P2x}F_{P2y} - R_{P2y}F_{P2x}) - (R_{P3x}F_{P3y} - R_{P3y}F_{P3x}) - (R_{P4x}F_{P4y} - R_{P4y}F_{P4x}) - (R_{P5x}F_{P5y} - R_{P5y}F_{P5x}) \\ m_4 a_{G_{4x}} \\ m_4 a_{G_{4y}} \\ I_{G_4}\alpha_4 \end{bmatrix}$$

$$\rightarrow \begin{bmatrix} 1 & 0 & 1 & 0 & 0 & 0 & 0 & 0 & 0 \\ 0 & 1 & 0 & 1 & 0 & 0 & 0 & 0 & 0 \\ -0.0039 & 0.0075 & 0.0156 & -0.0302 & 0 & 0 & 0 & 0 & 0 \\ 0 & 0 & -1 & 0 & 1 & 0 & 0 & 0 & 0 \\ 0 & 0 & 0 & -1 & 0 & 1 & 0 & 0 & 0 \\ 0 & 0 & -0.1357 & 0.2223 & -0.0190 & 0.1971 & 0 & 0 & 0 \\ 0 & 0 & 0 & 0 & -1 & 0 & 1 & 0 & 0 \\ 0 & 0 & 0 & 0 & 0 & -1 & 0 & 1 & 0 \\ 0 & 0 & 0 & 0 & 0.0688 & -0.0128 & 0.0688 & -0.0128 & 0 \end{bmatrix} \begin{bmatrix} F_{12x} \\ F_{12y} \\ F_{32x} \\ F_{32y} \\ F_{43x} \\ F_{43y} \\ F_{14x} \\ F_{14y} \\ 0 \end{bmatrix} =$$

$$\begin{bmatrix} 18.13 * 1.56 \\ 18.13 * (-3.02) \\ 0.0093 * 0 + 110 \\ 103.08 * (-4.17) + 4{,}131 + 4{,}131 + 4{,}131 + 4{,}131 + 4{,}131 \\ 103.08 * (-4.17) + 41{,}310 + 41{,}310 + 41{,}310 + 41{,}310 + 41{,}310 \\ 0.094 * (-22.82) - (-0.11 * (-38{,}026) + 0.01 * (-4{,}131)) - (-0.27 * (-38{,}026) - 0.047 * (-4{,}131)) - (0.58 * (-38{,}026) - 0.1 * (-4{,}131)) - (0.14 * (-38{,}026) - 0.15 * (-4{,}131)) - (0.23 * (-38{,}026) - 0.21 * (-4{,}131) \\ 12.05 * (-1.52) \\ 12.05 * (-7.93) \\ 0.093 * (-115.32) \end{bmatrix}$$

$$F_{12x} = 726.59N$$
$$F_{12y} = 63{,}943N$$
$$F_{32x} = -689.26N$$
$$F_{32y} = -64{,}15N$$
$$F_{43x} = 15{,}422N$$
$$F_{43y} = 87{,}231N$$
$$F_{14x} = 15{,}411N$$
$$F_{14y} = 87{,}134N$$

$$F_{12} = \sqrt{F_{12x}^2 + F_{12y}^2} = 63{,}947N, \qquad \theta_{F_{12}} = \arctan\left(\frac{F_{12y}}{F_{12x}}\right) = 89.34°$$

$$F_{32} = \sqrt{F_{32x}^2 + F_{32y}^2} = 64{,}018N, \qquad \theta_{F_{32}} = \arctan\left(\frac{F_{32y}}{F_{32x}}\right) = -90.61°$$

$$F_{43} = \sqrt{F_{43x}^2 + F_{43y}^2} = 88{,}584N, \qquad \theta_{F_{43}} = \arctan\left(\frac{F_{43y}}{F_{43x}}\right) = 79.97°$$

$$F_{14} = \sqrt{F_{14x}^2 + F_{14y}^2} = 88{,}487N, \qquad \theta_{F_{14}} = \arctan\left(\frac{F_{14y}}{F_{14x}}\right) = 79.97°$$

$$Global\ \theta_{F_{12}} = 89.34° - 96.2° = -6.85°$$

$$Global\ \theta_{F_{32}} = -90.61° - 96.2° = -186.81°$$

$$Global\ \theta_{F_{43}} = 79.97° - 96.2° = -16.22°$$

$$Global\ \theta_{F_{14}} = 79.97° - 96.2° = -16.22°$$

$$Global\ F_{12x} = F_{12} * \cos\left(Global\ \theta_{F_{12}}\right) = 63{,}490N$$

$$Global\ F_{12y} = F_{12} * \sin\left(Global\ \theta_{F_{12}}\right) = -7{,}628N$$

$$Global\ F_{32x} = F_{32} * \cos\left(Global\ \theta_{F_{32}}\right) = -63{,}566N$$

$$Global\ F_{32y} = F_{32} * \sin\left(Global\ \theta_{F_{32}}\right) = 7{,}599N$$

$$Global\ F_{43x} = F_{43} * \cos\left(Global\ \theta_{F_{43}}\right) = 85{,}055N$$

$$Global\ F_{43y} = F_{43} * \sin\left(Global\ \theta_{F_{43}}\right) = -24{,}753N$$

$$Global\ F_{14x} = F_{14} * \cos\left(Global\ \theta_{F_{14}}\right) = 84{,}960N$$

$$Global\ F_{14y} = F_{14} * \sin\left(Global\ \theta_{F_{14}}\right) = -24{,}731N$$

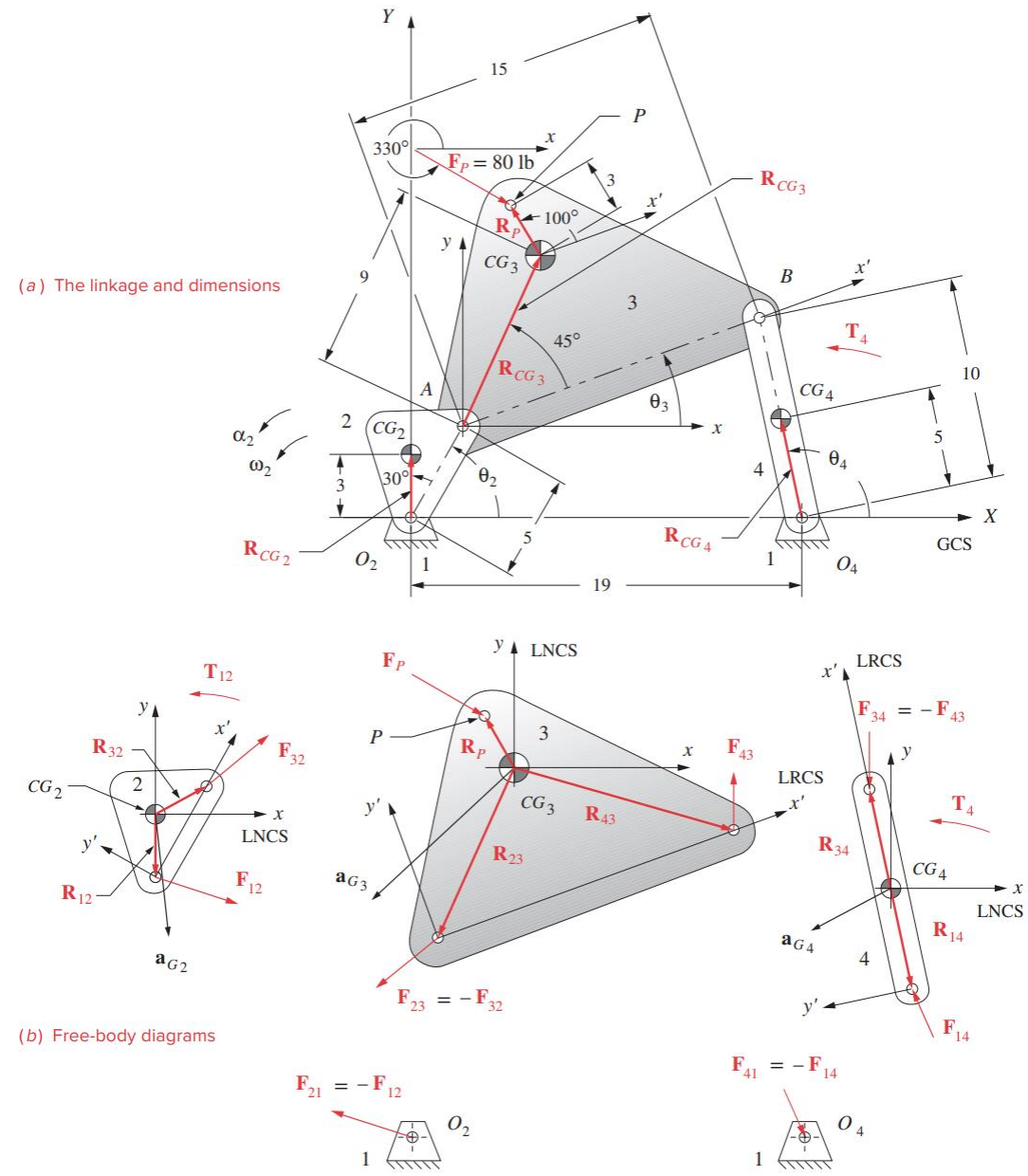

$$F_{Shaking} = F_{21} + F_{41} = -F_{12} - F_{14}$$

$$Global\ F_{Shaking,x} = -Global\ F_{12x} - Global\ F_{14x} = -148{,}450N$$

$$Global\ F_{Shaking,y} = -Global\ F_{12y} - Global\ F_{14y} = 32{,}359N$$

$$\theta_{V_{P_1}} = \arctan\left(\frac{V_{P1y}}{V_{P1x}}\right) = 101.75°$$

$$\theta_{V_{P_2}} = \arctan\left(\frac{V_{P2y}}{V_{P2x}}\right) = 99.2°$$

$$\theta_{V_{P_3}} = \arctan\left(\frac{V_{P3y}}{V_{P3x}}\right) = 93.43°$$

$$\theta_{V_{P_4}} = \arctan\left(\frac{V_{P4y}}{V_{P4x}}\right) = 69.5°$$

$$\theta_{V_{P_5}} = \arctan\left(\frac{V_{P5y}}{V_{P5x}}\right) = 325.46°$$

$$Global\ \theta_{V_{P_1}} = 101.75° - 96.2° = 5.55°$$

$$Global\ \theta_{V_{P_2}} = 99.2° - 96.2° = 2.99°$$

$$Global\ \theta_{V_{P_3}} = 93.43° - 96.2° = -2.77°$$

$$Global\ \theta_{V_{P_4}} = 69.5° - 96.2° = -26.69°$$

$$Global\ \theta_{V_{P_5}} = 325.46° - 96.2v = 229.26°$$

$$P_{in} = P_{out} \rightarrow T_{in} \cdot \omega_{in} = F_{out} \cdot v_n \rightarrow F_{out} = \frac{T_{in} \cdot \omega_{in}}{v_n}$$

$$F_{out,P1} = \frac{T_2 \cdot \omega_2}{V_{P1}/1000} = 108{,}570N$$

$$F_{out,P2} = \frac{T_2 \cdot \omega_2}{V_{P2}/1000} = 151{,}330N$$

$$F_{out,P3} = \frac{T_2 \cdot \omega_2}{V_{P3}/1000} = 248{,}090N$$

$$F_{out,P4} = \frac{T_2 \cdot \omega_2}{V_{P4}/1000} = 614{,}060N$$

$$F_{out,P5} = \frac{T_2 \cdot \omega_2}{V_{P5}/1000} = 589{,}240N$$

$$Global\ F_{out,P1x} = 108{,}570N * cos\left(Global\ \theta_{V_{P_1}}\right) = 108{,}060N$$

$$Global\ F_{out,P2x} = 151{,}330N * cos\left(Global\ \theta_{V_{P_2}}\right) = 151{,}130N$$

$$Global\ F_{out,P3x} = 248{,}090N * cos\left(Global\ \theta_{V_{P3}}\right) = 247{,}800N$$

$$Global\ F_{out,P4x} = 614{,}060N * cos\left(Global\ \theta_{V_{P4}}\right) = 548{,}590N$$

$$Global\ F_{out,P5x} = 589{,}240N * cos\left(Global\ \theta_{V_{P5}}\right) = -384{,}510N$$

APPENDIX B

Four-bar Linkage Calculations MATLAB code - "JawCrusherConceptOneForces.m."

```
close all
clear
clc

% Parameters
CompressiveStrength = 1530*1000; %Pa, Compressive strengtn of lava rock
CrushingArea = 0.4 * 0.05; % m^2, Area of contact at each point
Overestimating = 1.25; % adding 25% strength to rocks as an overestimation
Force = CompressiveStrength * CrushingArea * Overestimating ; % N, Force acting on each point

Correction_angle = -96.2; % Changing from Local to Global coordinates

Global_theta2_deg_values = [0, 15, 30, 45, 60, 75, 90, 105, 120, 135, 150, 165, 180, 195, 210, 225, 240, 255, 270, 285, 300, 315, 330, 345]; % degrees

theta2_deg_values =       [267.4, 282.4, 297.4, 312.4, 327.4, 342.4, 357.4, 12.4, 27.4, 42.4, 57.4, 72.4, 87.4, 102.4, 117.4, 132.4, 147.4, 162.4, 177.4, 192.4, 207.4, 222.4, 237.4, 252.4]; % degress

b_values =                [428.4, 420.8, 411.8, 403.4, 395.7, 389.3, 384.8, 382.6, 382.8, 385.4, 390.1, 396.6, 404.3, 412.7, 421.1, 428.9, 435.8, 441.3, 445.2, 447.1, 447.1, 445, 441.1, 435.4]; % mm

R23_values =              [248.2, 241.1, 233.1, 224.5, 216.1, 208.3, 202, 197.6, 195.7, 196.4, 199.6, 205, 212, 220.1, 228.5, 236.7, 244.2, 250.7, 255.7, 259, 260.5, 260.2, 257.9, 253.9]/1000; % m

theta_R23_values =        [-141.5, -140.5, -139.9, -139.8, -140.4, -141.7, -143.5, -145.8, -148.4, -151.1, -153.5, -155.4, -156.7, -157.3, -157.3, -156.7, -155.6, -154.2, -152.5, -150.6, -148.6, -146.6, -144.7, -143]; % degrees

theta_R43_values =        [5.8, 5.7, 5.6, 5.5, 5.3, 5, 4.8, 4.6, 4.4, 4.3, 4.2, 4.2, 4.2, 4.3, 4.4, 4.5, 4.7, 4.9, 5.1, 5.3, 5.5, 5.7, 5.8, 5.8]; % degrees


R_AP1_values =            [180.9, 177.5, 172.5, 166, 158.4, 150, 141.4, 133.2, 126.1, 120.8, 118, 118, 120.7, 125.8, 132.7, 140.6, 149, 157.2, 164.8, 171.3, 176.6, 180.3, 182.3, 182.5];

R_AP2_values =            [255.1, 249.4, 242.3, 234.3, 225.7, 217.3, 209.5, 203.1, 198.8, 196.8, 197.5, 200.6, 205.9, 212.9, 220.9, 229.2, 237.5, 245, 251.5, 256.6, 260, 261.6, 261.3, 259.1];

R_AP3_values =            [342.6, 336, 328.2, 319.7, 311.2, 303.1, 296.3, 291.2, 288.3, 287.9, 289.9, 294.2, 300.4, 307.9, 316.1, 324.5, 332.5, 339.6, 345.5, 349.7, 352.2, 352.7, 351.2, 347.8];

R_AP4_values =            [435.6, 428.4, 420.3, 411.8, 403.3, 395.7, 389.5, 385.1, 383, 383.4, 386.1, 391, 397.6, 405.3, 413.7, 422, 429.8, 436.6, 442.1, 445.8, 447.7, 447.6, 445.4, 441.4];

R_AP5_values =            [531.1, 523.7, 515.4, 506.8, 498.6, 491.2, 485.4, 481.5, 479.9, 480.8, 483.9, 489.1, 495.9, 503.8, 512.1, 520.4, 528.1, 534.8, 539.9, 543.4, 544.8, 544.3, 541.7, 537.2];

theta_AP1_values =        [70.3, 72.8, 74.9, 76.7, 77.9, 78.4, 78.1, 76.8, 74.5, 71.2, 67.2, 63.1, 59.2, 56.2, 54.1, 53.2, 53.1, 54, 55.4, 57.4, 59.8, 62.3, 65, 67.7];

theta_AP2_values =        [52.4, 53.8, 54.8, 55.3, 55.3, 54.7, 53.5, 51.7, 49.4, 46.9, 44.3, 42, 40.1, 38.9, 38.3, 38.3, 38.9, 40, 41.4, 43.1, 45, 46.9, 48.9, 50.7];

theta_AP3_values =        [43, 43.8, 44.3, 44.4, 44.1, 43.3, 42.1, 40.5, 38.7, 36.9, 35.2, 33.7, 32.6, 31.9, 31.7, 31.9, 32.6, 33.5, 34.7, 36.1, 37.6, 39.1, 40.6, 41.9];

theta_AP4_values =        [37.5, 38.1, 38.3, 38.2, 37.8, 37, 35.9, 34.6, 33.2, 31.8, 30.5, 29.4, 28.7, 28.2, 28.2, 28.5, 29.1, 29.9, 30.9, 32.1, 33.3, 34.6, 35.7, 36.7];

theta_AP5_values =        [34, 34.4, 34.5, 34.3, 33.9, 33.2, 32.3, 31.1, 29.9, 28.7, 27.7, 26.9, 26.3, 26, 26, 26.3, 26.9, 27.6, 28.5, 29.5, 30.6, 31.6, 32.6, 33.4];


% Constants
a = 37.5; % mm,   R2,  length of the input link
c = 140; % mm,    R3,  length of the output link
d = 360.5; % mm, R1,  length of the ground link
omega2 = -20; % rad/s, angular velocity of link 2
alpha2 = 0; % rad/s^2, angular acceleration of link 2


omega3_values = zeros(1, length(theta2_deg_values));
omega4_values = zeros(1, length(theta2_deg_values));

alpha3_values = zeros(1, length(theta2_deg_values));
alpha4_values = zeros(1, length(theta2_deg_values));

F_P1_values = zeros(1, length(theta2_deg_values));
F_P2_values = zeros(1, length(theta2_deg_values));
F_P3_values = zeros(1, length(theta2_deg_values));
F_P4_values = zeros(1, length(theta2_deg_values));
F_P5_values = zeros(1, length(theta2_deg_values));
```

```
F12_values = zeros(1, length(theta2_deg_values));
F32_values = zeros(1, length(theta2_deg_values));
F43_values = zeros(1, length(theta2_deg_values));
F14_values = zeros(1, length(theta2_deg_values));

Ms_values = zeros(1, length(theta2_deg_values));

F_out_P1_values = zeros(1, length(theta2_deg_values));
F_out_P2_values = zeros(1, length(theta2_deg_values));
F_out_P3_values = zeros(1, length(theta2_deg_values));
F_out_P4_values = zeros(1, length(theta2_deg_values));
F_out_P5_values = zeros(1, length(theta2_deg_values));

Global_F_out_P1_x_value = zeros(1, length(theta2_deg_values));
Global_F_out_P2_x_value = zeros(1, length(theta2_deg_values));
Global_F_out_P3_x_value = zeros(1, length(theta2_deg_values));
Global_F_out_P4_x_value = zeros(1, length(theta2_deg_values));
Global_F_out_P5_x_value = zeros(1, length(theta2_deg_values));


for i = 1:length(theta2_deg_values)
```

```
% Changing parameters
theta2_deg = theta2_deg_values(i);
Global_theta2_deg = Global_theta2_deg_values(i);
b = b_values(i); % mm, update the length of the output link
R_23 = R23_values(i) ; % m, update the distance from pivot 2 to the CG of Link 3
theta_R23_deg = theta_R23_values(i); % degrees, update theta_R23
theta_R43_deg = theta_R43_values(i); % degrees, update theta_R43
theta_RCG3_deg = theta_R23_deg + 180; % degrees, update theta_R43
F_P1 = F_P1_values(i); % N, force magnitude at point P1
F_P2 = F_P2_values(i); % N, force magnitude at point P2
F_P3 = F_P3_values(i); % N, force magnitude at point P3
F_P4 = F_P4_values(i); % N, force magnitude at point P4
F_P5 = F_P5_values(i); % N, force magnitude at point P5
R_AP1 = R_AP1_values(i); % m, distance from A to P1
R_AP2 = R_AP2_values(i); % m, distance from A to P2
R_AP3 = R_AP3_values(i); % m, distance from A to P3
R_AP4 = R_AP4_values(i); % m, distance from A to P4
R_AP5 = R_AP5_values(i); % m, distance from A to P5
theta_AP1_deg = theta_AP1_values(i);
theta_AP2_deg = theta_AP2_values(i);
theta_AP3_deg = theta_AP3_values(i);
theta_AP4_deg = theta_AP4_values(i);
theta_AP5_deg = theta_AP5_values(i);
```

Position Analysis - (Example 4-1)

```
theta2_rad = theta2_deg * pi/180;

K1 = d/a;
K2 = d/c;
K3 = (a.^2 - b.^2 + c.^2 + d.^2)/(2 .* a .* c);
K4 = d/b;
K5 = (c.^2 - d.^2 - a.^2 - b.^2)/(2 .* a .* b);

A_matrix = cos(theta2_rad) - K1 - K2 .* cos(theta2_rad) + K3;
B = -2 .* sin(theta2_rad);
C = K1 - (K2+1) .* cos(theta2_rad) + K3;
D = cos(theta2_rad) - K1 + K4 .* cos(theta2_rad) + K5;
E = -2 .* sin(theta2_rad);
F = K1 + (K4-1) .* cos(theta2_rad) + K5;

theta3_rad = 2 .* atan((-E - sqrt(E.^2 - 4 .* D .* F)) / (2 .* D)); % radians, angle of link 3
theta3_deg = theta3_rad .* 180/pi(); % degrees, angle of link 3
theta4_rad = 2 .* atan((-B - sqrt(B.^2 - 4 .* A_matrix .* C)) / (2 .* A_matrix)); % radians, angle of link 4
theta4_deg = theta4_rad .* 180/pi(); % degrees, angle of link 4
```

```
omega3 = ((a.*omega2)/b) .* ((sin(theta4_rad - theta2_rad)/(sin(theta3_rad - theta4_rad)))); % rad/s, angular velocity of link 3
omega4 = ((a.*omega2)/c) .* ((sin(theta2_rad - theta3_rad)/(sin(theta4_rad - theta3_rad)))); % rad/s, angular velocity of link 4

VA_x = a .* omega2 .* (-sin(theta2_rad)); % mm/s, velocity component in x-direction at A
VA_y = a .* omega2 .* (cos(theta2_rad)); % mm/s, velocity component in y-direction at A
VA = sqrt(VA_x.^2 + VA_y.^2); % mm/s, magnitude of velocity at A
VA_angle_rad = atan2(VA_y, VA_x); % radians, angle of velocity vector at A
VA_angle_deg =mod(VA_angle_rad * 180/pi(), 360); % degrees, angle of velocity vector at A in degrees

VBA_x = b .* omega3 .* (-sin(theta3_rad)); % mm/s, velocity component in x-direction at B relative to A
VBA_y = b .* omega3 .* (cos(theta3_rad)); % mm/s, velocity component in y-direction at B relative to A
VBA = sqrt(VBA_x.^2 + VBA_y.^2); % mm/s, magnitude of velocity at B relative to A
VBA_angle_rad = atan2(VBA_y, VBA_x); % radians, angle of velocity vector at B relative to A
VBA_angle_deg = mod(VBA_angle_rad * 180/pi(), 360); % degrees, angle of velocity vector at B relative to A in degrees

VB_x = c .* omega4 .* (-sin(theta4_rad)); % mm/s, velocity component in x-direction at B
VB_y = c .* omega4 .* (cos(theta4_rad)); % mm/s, velocity component in y-direction at B
VB = sqrt(VB_x.^2 + VB_y.^2); % mm/s, magnitude of velocity at B
VB_angle_rad = atan2(VB_y, VB_x); % radians, angle of velocity vector at B
VB_angle_deg = mod(VB_angle_rad * 180/pi(), 360); % degrees, angle of velocity vector at B in degrees


% Velocity at P1, P2, P3, P4, P5
theta_AP1_rad = theta_AP1_deg * pi/180;
theta_AP2_rad = theta_AP2_deg * pi/180;
theta_AP3_rad = theta_AP3_deg * pi/180;
theta_AP4_rad = theta_AP4_deg * pi/180;
theta_AP5_rad = theta_AP5_deg * pi/180;

VAP1_x = -R_AP1 * omega3 * sin(theta_AP1_rad); % mm/s, Velocity component in x-direction
VAP1_y = R_AP1 * omega3 * cos(theta_AP1_rad); % mm/s, Velocity component in y-direction
VAP1 = sqrt(VAP1_x.^2 + VAP1_y.^2); % mm/s, magnitude of velocity at A

VAP2_x = -R_AP2 * omega3 * sin(theta_AP2_rad); % mm/s, Velocity component in x-direction
VAP2_y = R_AP2 * omega3 * cos(theta_AP2_rad); % mm/s, Velocity component in y-direction
VAP2 = sqrt(VAP2_x.^2 + VAP2_y.^2); % mm/s, magnitude of velocity at A

VAP3_x = -R_AP3 * omega3 * sin(theta_AP3_rad); % mm/s, Velocity component in x-direction
VAP3_y = R_AP3 * omega3 * cos(theta_AP3_rad); % mm/s, Velocity component in y-direction
VAP3 = sqrt(VAP3_x.^2 + VAP3_y.^2); % mm/s, magnitude of velocity at A

VAP4_x = -R_AP4 * omega3 * sin(theta_AP4_rad); % Velocity component in x-direction
VAP4_y = R_AP4 * omega3 * cos(theta_AP4_rad); % Velocity component in y-direction
VAP4 = sqrt(VAP4_x.^2 + VAP4_y.^2); % mm/s, magnitude of velocity at A

VAP5_x = -R_AP5 * omega3 * sin(theta_AP5_rad); % mm/s, Velocity component in x-direction
VAP5_y = R_AP5 * omega3 * cos(theta_AP5_rad); % mm/s, Velocity component in y-direction
VAP5 = sqrt(VAP5_x.^2 + VAP5_y.^2); % mm/s, magnitude of velocity at A
```

```
VP1_x = VA_x + VAP1_x; % mm/s, Velocity component in x-direction at P
VP1_y = VA_y + VAP1_y; % mm/s, Velocity component in y-direction at P
VP1 = sqrt(VP1_x.^2 + VP1_y.^2); % mm/s, magnitude of velocity
VP1_angle_rad = atan2(VP1_y, VP1_x); % Angle in radians
VP1_angle_deg = mod(VP1_angle_rad * 180/pi, 360); % Angle in degrees
if VP1_y > 0
    F_P1 = Force; % N, force magnitude at point P1
else
    F_P1 = 0; % No force applied if the velocity component in y-direction at P1 is negative
end


VP2_x = VA_x + VAP2_x; % mm/s, Velocity component in x-direction at P2
VP2_y = VA_y + VAP2_y; % mm/s, Velocity component in y-direction at P2
VP2 = sqrt(VP2_x.^2 + VP2_y.^2); % mm/s, magnitude of velocity
VP2_angle_rad = atan2(VP2_y, VP2_x); % Angle in radians
VP2_angle_deg = mod(VP2_angle_rad * 180/pi, 360); % Angle in degrees
if VP2_y > 0
    F_P2 = Force; % N, force magnitude at point P2
else
    F_P2 = 0; % No force applied if the velocity component in y-direction at P2 is negative
end


VP3_x = VA_x + VAP3_x; % mm/s, Velocity component in x-direction at P3
VP3_y = VA_y + VAP3_y; % mm/s, Velocity component in y-direction at P3
VP3 = sqrt(VP3_x.^2 + VP3_y.^2); % mm/s, magnitude of velocity
VP3_angle_rad = atan2(VP3_y, VP3_x); % Angle in radians
VP3_angle_deg = mod(VP3_angle_rad * 180/pi, 360); % Angle in degrees
if VP3_y > 0
    F_P3 = Force; % N, force magnitude at point P3
else
    F_P3 = 0; % No force applied if the velocity component in y-direction at P3 is negative
end


VP4_x = VA_x + VAP4_x; % mm/s, Velocity component in x-direction at P4
VP4_y = VA_y + VAP4_y; % mm/s, Velocity component in y-direction at P4
VP4 = sqrt(VP4_x.^2 + VP4_y.^2); % mm/s, magnitude of velocity
VP4_angle_rad = atan2(VP4_y, VP4_x); % Angle in radians
VP4_angle_deg = mod(VP4_angle_rad * 180/pi, 360); % Angle in degrees
if VP4_y > 0
    F_P4 = Force; % N, force magnitude at point P4
else
    F_P4 = 0; % No force applied if the velocity component in y-direction at P4 is negative
end


VP5_x = VA_x + VAP5_x; % mm/s, Velocity component in x-direction at P5
VP5_y = VA_y + VAP5_y; % mm/s, Velocity component in y-direction at P5
VP5 = sqrt(VP5_x.^2 + VP5_y.^2); % mm/s, magnitude of velocity
VP5_angle_rad = atan2(VP5_y, VP5_x); % Angle in radians
VP5_angle_deg = mod(VP5_angle_rad * 180/pi, 360); % Angle in degrees
if VP5_y > 0
    F_P5 = Force; % N, force magnitude at point P5
else
    F_P5 = 0; % No force applied if the velocity component in y-direction at P5 is negative
end
```

Acceleration Analysis - (Example 7-2)

```
AA = c .* sin(theta4_rad);
BB = b .* sin(theta3_rad);
CC = a .* alpha2 * sin(theta2_rad) + a .* omega2.^2 .* cos(theta2_rad) + b .* omega3.^2 .* cos(theta3_rad) - c .* omega4.^2 .* cos(theta4_rad);
DD = c .* cos(theta4_rad);
EE = b .* cos(theta3_rad);
FF = a .* alpha2 * cos(theta2_rad) - a .* omega2.^2 .* sin(theta2_rad) - b .* omega3.^2 .* sin(theta3_rad) + c .* omega4.^2 .* sin(theta4_rad);

alpha3 = (CC.*DD - AA.*FF)/(AA.*EE - BB.*DD); % rad/s^2, calculated angular acceleration of link 3
alpha4 = (CC.*EE - BB.*FF)/(AA.*EE - BB.*DD); % rad/s^2, calculated angular acceleration of link 4

AA_x = -a .* alpha2 .* sin(theta2_rad) - a .* omega2.^2 .* cos(theta2_rad); % m/s^2, acceleration component in x-direction at A
AA_y = a .* alpha2 .* cos(theta2_rad) - a .* omega2.^2 .* sin(theta2_rad); % m/s^2, acceleration component in y-direction at A
AA = sqrt(AA_x.^2 + AA_y.^2); % m/s^2, magnitude of acceleration at A
AA_angle_rad = atan2(AA_y, AA_x); % radians, angle of acceleration vector at A
AA_angle_deg = mod(AA_angle_rad * 180/pi(), 360); % degrees, angle of acceleration vector at A in degrees

ABA_x = -b .* alpha3 .* sin(theta3_rad) - b .* omega3.^2 .* cos(theta3_rad); % m/s^2, acceleration component in x-direction at B relative to A
ABA_y = b .* alpha3 .* cos(theta3_rad) - b .* omega3.^2 .* sin(theta3_rad); % m/s^2, acceleration component in y-direction at B relative to A
ABA = sqrt(ABA_x.^2 + ABA_y.^2); % m/s^2, magnitude of acceleration at B relative to A
ABA_angle_rad = atan2(ABA_y, ABA_x); % radians, angle of acceleration vector at B relative to A
ABA_angle_deg = mod(ABA_angle_rad * 180/pi(), 360); % degrees, angle of acceleration vector at B relative to A in degrees

AB_x = -c .* alpha4 .* sin(theta4_rad) - c .* omega4.^2 .* cos(theta4_rad); % m/s^2, acceleration component in x-direction at B
AB_y = c .* alpha4 .* cos(theta4_rad) - c .* omega4.^2 .* sin(theta4_rad); % m/s^2, acceleration component in y-direction at B
AB = sqrt(AB_x.^2 + AB_y.^2); % m/s^2, magnitude of acceleration at B
AB_angle_rad = atan2(AB_y, AB_x); % radians, angle of acceleration vector at B
AB_angle_deg = mod(AB_angle_rad * 180/pi(), 360); % degrees, angle of acceleration vector at B in degrees
```

Force Analysis (Example 11-3)

```
%Link 2 - Cranker
m2 = 18.131; % kg, mass of Link 2
I_G2 = 0.00925451; % kg*m^2, moment of inertia of Link 2 about its center of gravity
R_12 = 8.5/1000; % m, distance from CG to pivot 1 of Link 2
theta_R12_deg = theta2_deg + 180; % degress
theta_R12_rad = theta_R12_deg * pi/180; % radians
R_12x = R_12 * cos(theta_R12_rad); % m
R_12y = R_12 * sin(theta_R12_rad); % m
R_32 = 34/1000;  % m, distance from CG to pivot 3 of Link 2
theta_R32_deg = theta2_deg; % degrees
theta_R32_rad = theta2_rad; % degrees
R_32x = R_32 * cos(theta_R32_rad); % m
R_32y = R_32 * sin(theta_R32_rad); % m
R_CG2 = R_12; % m, radius to the CG of Link 2 from its rotation axis
a_tG2 = alpha2 * R_CG2;  % m/s^2, tangential acceleration of the CG of Link 2
a_rG2 = omega2^2 * R_CG2;  % m/s^2, radial (centripetal) acceleration of the CG of Link 2
a_G2 = sqrt(a_tG2^2 + a_rG2^2);  % m/s^2, magnitude of total acceleration at the CG of Link 2
a_G2x = a_tG2 * cos(theta2_rad) - a_rG2 * sin(theta2_rad);  % m/s^2, x-component of total acceleration
a_G2y = a_tG2 * sin(theta2_rad) + a_rG2 * cos(theta2_rad);  % m/s^2, y-component of total acceleration
theta_aG2_rad = atan2(a_G2y, a_G2x); % rad, angle of total acceleration vector from the x-axis
theta_aG2_deg = theta_aG2_rad * 180/pi; % degrees, angle of total acceleration vector in degrees
T2 = -110; % Nm, external torque applied on Link 2

%Link 3 - Coupler
m3 = 103.08256532; % kg, mass of Link 3
I_G3 = 47.71999417;  % kg*m^2, moment of inertia of Link 3 about its center of gravity
theta_R23_rad = theta_R23_deg .* pi/180; % radians
R_23x = R_23 .* cos(theta_R23_rad); % m
R_23y = R_23 .* sin(theta_R23_rad); % m
R_43 = 198/1000; % m, distance from pivot 4 to the CG of Link 3
theta_R43_rad = theta_R43_deg .* pi/180; % radians
R_43x = R_43 .* cos(theta_R43_rad); % m
R_43y = R_43 .* sin(theta_R43_rad); % m
R_CG3 = R_23; % m
theta_RCG3_rad = theta_RCG3_deg * pi/180;
a_tG3 = alpha3 .* R_CG3; % m/s^2, tangential acceleration of CG of Link 3
a_rG3 = omega3.^2 .* R_CG3; % m/s^2, radial (centripetal) acceleration of CG of Link 3
a_G3 = sqrt(a_tG3.^2 + a_rG3.^2); % m/s^2
a_G3x = a_tG3 .* cos(theta3_rad + theta_RCG3_rad) - a_rG3 .* sin(theta3_rad + theta_RCG3_rad); % m/s^2, x-component
a_G3y = a_tG3 .* sin(theta3_rad + theta_RCG3_rad) + a_rG3 .* cos(theta3_rad + theta_RCG3_rad); % m/s^2, y-component
theta_aG3_rad = atan2(a_G3y, a_G3x); % rad, angle of total acceleration vector
theta_aG3_deg = theta_aG3_rad * 180/pi; % degrees, angle in degrees

R_P1 = 111.55 / 1000; % m, distance from CG to point P1
R_P2 = 54.06 / 1000; % m, distance from CG to point P2
R_P3 = 115.81 / 1000; % m, distance from CG to point P3
R_P4 = 209.52 / 1000; % m, distance from CG to point P4
R_P5 = 307.21 / 1000; % m, distance from CG to point P5
```

```
thetaP1_deg = 182.87; % degrees
thetaP2_deg = 119.3; % degrees
thetaP3_deg = 59.69; % degrees
thetaP4_deg = 46.81; % degrees
thetaP5_deg = 42; % degrees

thetaP1_rad = thetaP1_deg * pi / 180; % radians
thetaP2_rad = thetaP2_deg * pi / 180; % radians
thetaP3_rad = thetaP3_deg * pi / 180; % radians
thetaP4_rad = thetaP4_deg * pi / 180; % radians
thetaP5_rad = thetaP5_deg * pi / 180; % radians

R_P1x = R_P1 * cos(thetaP1_rad); % m, x-component of distance to point P1 from CG
R_P1y = R_P1 * sin(thetaP1_rad); % m, y-component of distance to point P1 from CG
R_P2x = R_P2 * cos(thetaP2_rad); % m, x-component of distance to point P2 from CG
R_P2y = R_P2 * sin(thetaP2_rad); % m, y-component of distance to point P2 from CG
R_P3x = R_P3 * cos(thetaP3_rad); % m, x-component of distance to point P3 from CG
R_P3y = R_P3 * sin(thetaP3_rad); % m, y-component of distance to point P3 from CG
R_P4x = R_P4 * cos(thetaP4_rad); % m, x-component of distance to point P4 from CG
R_P4y = R_P4 * sin(thetaP4_rad); % m, y-component of distance to point P4 from CG
R_P5x = R_P5 * cos(thetaP5_rad); % m, x-component of distance to point P5 from CG
R_P5y = R_P5 * sin(thetaP5_rad); % m, y-component of distance to point P5 from CG

thetaF_deg = Correction_angle; % degrees, common angle for all external forces
thetaF_rad = thetaF_deg * pi() / 180; % radians

F_P1x = F_P1 * cos(thetaF_rad); % N, x-component of force at point P1
F_P1y = F_P1 * sin(thetaF_rad); % N, y-component of force at point P1
F_P2x = F_P2 * cos(thetaF_rad); % N, x-component of force at point P2
F_P2y = F_P2 * sin(thetaF_rad); % N, y-component of force at point P2
F_P3x = F_P3 * cos(thetaF_rad); % N, x-component of force at point P3
F_P3y = F_P3 * sin(thetaF_rad); % N, y-component of force at point P3
F_P4x = F_P4 * cos(thetaF_rad); % N, x-component of force at point P4
F_P4y = F_P4 * sin(thetaF_rad); % N, y-component of force at point P4
F_P5x = F_P5 * cos(thetaF_rad); % N, x-component of force at point P5
F_P5y = F_P5 * sin(thetaF_rad); % N, y-component of force at point P5

%Link 4 - Rocker
m4 = 12.050895; % kg, mass of Link 4
I_G4 = 0.093746; % kg*m^2, moment of inertia of Link 4 about its center of gravity
R_34 = 70 / 1000; % m, distance from pivot 3 to the CG of Link 4
theta_R34_deg = theta4_deg; % degress
theta_R34_rad = theta_R34_deg * pi/180; % radians
R_34x = R_34 * cos(theta_R34_rad); % m
R_34y = R_34 * sin(theta_R34_rad); % m
R_14 = 70 / 1000; % m, distance from pivot 1 to the CG of Link 4
theta_R14_deg = theta4_deg + 180; % degress
theta_R14_rad = theta_R14_deg * pi/180; % radians
R_14x = R_14 * cos(theta_R14_rad); % m
R_14y = R_14 * sin(theta_R14_rad); % m
R_CG4 = 70/1000; % m, radius to CG of Link 4 from its rotation axis, using R_14's magnitude
a_tG4 = alpha4 * R_CG4; % m/s^2, tangential acceleration of the CG of Link 4
a_rG4 = omega4^2 * R_CG4; % m/s^2, radial (centripetal) acceleration of the CG of Link 4
a_G4 = sqrt(a_tG4^2 + a_rG4^2); % m/s^2
a_G4x = a_tG4 * cos(theta4_rad) - a_rG4 * sin(theta4_rad); % m/s^2, x-component of total acceleration
a_G4y = a_tG4 * sin(theta4_rad) + a_rG4 * cos(theta4_rad); % m/s^2, y-component of total acceleration
theta_aG4_rad = atan2(a_G4y, a_G4x); % rad, angle of total acceleration vector from the x-axis
theta_aG4_deg = theta_aG4_rad * 180/pi; % degrees, angle of total acceleration vector in degrees
```

```
A_matrix = [1,         0,          1,          0,          0,          0,          0,          0,          0,         ;
     0,         1,          0,          1,          0,          0,          0,          0,          0,         ;
     -R_12y,    R_12x,      -R_32y,     R_32x,      0,          0,          0,          0,          0,         ;
     0,         0,          -1,         0,          1,          0,          0,          0,          0,         ;
     0,         0,          0,          -1,         0,          1,          0,          0,          0,         ;
     0,         0,          R_23y,      -R_23x,     -R_43y,     R_43x,      0,          0,          0,         ;
     0,         0,          0,          0,          -1,         0,          1,          0,          0,         ;
     0,         0,          0,          0,          0,          -1,         0,          1,          0,         ;
     0,         0,          0,          0,          R_34y,      -R_34x,     -R_14y,     R_14x,     ];

b_matrix = [m2*a_G2x;
     m2*a_G2y;
     I_G2*alpha2 - T2;
     m3*a_G3x - F_P1x - F_P2x - F_P3x - F_P4x - F_P5x;
     m3*a_G4y - F_P1y - F_P2y - F_P3y - F_P4y - F_P5y;
     I_G3*alpha3 - (R_P1x*F_P1y + R_P1y*F_P1x) - (R_P2x*F_P2y + R_P2y*F_P2x) - (R_P3x*F_P3y + R_P3y*F_P3x) - (R_P4x*F_P4y + R_P4y*F_P4x) - (R_P5x*F_P5y + R_P5y*F_P5x);
     m4*a_G4x;
     m4*a_G4y;
     I_G4*alpha4];

unknowns = A_matrix\b_matrix;

F12_x = unknowns(1);
F12_y = unknowns(2);
F32_x = unknowns(3);
F32_y = unknowns(4);
F43_x = unknowns(5);
F43_y = unknowns(6);
F14_x = unknowns(7);
F14_y = unknowns(8);

F12 = sqrt(F12_x^2 + F12_y^2);
F32 = sqrt(F32_x^2 + F32_y^2);
F43 = sqrt(F43_x^2 + F43_y^2);
F14 = sqrt(F14_x^2 + F14_y^2);

theta_F12 = atan2(F12_y, F12_x) * (180/pi); % degrees
theta_F32 = atan2(F32_y, F32_x) * (180/pi); % degrees
theta_F43 = atan2(F43_y, F43_x) * (180/pi); % degrees
theta_F14 = atan2(F14_y, F14_x) * (180/pi); % degrees

% Changing local coordinates to global coordinates
Global_theta_F12_deg = theta_F12 + Correction_angle; % degrees
Global_theta_F32_deg = theta_F32 + Correction_angle; % degrees
Global_theta_F43_deg = theta_F43 + Correction_angle; % degrees
Global_theta_F14_deg = theta_F14 + Correction_angle; % degrees

Global_F12_x = F12 * cosd(Global_theta_F12_deg);
Global_F12_y = F12 * sind(Global_theta_F12_deg);
Global_F32_x = F32 * cosd(Global_theta_F32_deg);
Global_F32_y = F32 * sind(Global_theta_F32_deg);
Global_F43_x = F43 * cosd(Global_theta_F43_deg);
Global_F43_y = F43 * sind(Global_theta_F43_deg);
Global_F14_x = F14 * cosd(Global_theta_F14_deg);
Global_F14_y = F14 * sind(Global_theta_F14_deg);
```

Shaking force

```
Fs_x = -Global_F12_x - Global_F14_x; %Shaking Force x-direction
Fs_y = -Global_F12_y - Global_F14_y; %Shaking Force x-direction
Ms = -T2 + ((d/1000) * (-1*F14)); %Shaking Moment
```

Mechanical Advanatge and Output Force

```
R_in = a/1000; % m, length of link 2
F_in = abs(T2 / R_in); % N, output force of link 2

MA_P1 = abs(omega2/(VP1/1000));
MA_P2 = abs(omega2/(VP2/1000));
MA_P3 = abs(omega2/(VP3/1000));
MA_P4 = abs(omega2/(VP4/1000));
MA_P5 = abs(omega2/(VP5/1000));

F_out_P1 = MA_P1 * F_in;
F_out_P2 = MA_P2 * F_in;
F_out_P3 = MA_P3 * F_in;
F_out_P4 = MA_P4 * F_in;
F_out_P5 = MA_P5 * F_in;

Global_VP1_angle_deg = VP1_angle_deg + Correction_angle;
Global_VP2_angle_deg = VP2_angle_deg + Correction_angle;
Global_VP3_angle_deg = VP3_angle_deg + Correction_angle;
Global_VP4_angle_deg = VP4_angle_deg + Correction_angle;
Global_VP5_angle_deg = VP5_angle_deg + Correction_angle;

Global_VP1_x = VP1 * cosd(Global_VP1_angle_deg);
Global_VP2_x = VP2 * cosd(Global_VP2_angle_deg);
Global_VP3_x = VP3 * cosd(Global_VP3_angle_deg);
Global_VP4_x = VP4 * cosd(Global_VP4_angle_deg);
Global_VP5_x = VP5 * cosd(Global_VP5_angle_deg);

Global_VP1_y = VP1 * sind(Global_VP1_angle_deg);
Global_VP2_y = VP2 * sind(Global_VP2_angle_deg);
Global_VP3_y = VP3 * sind(Global_VP3_angle_deg);
Global_VP4_y = VP4 * sind(Global_VP4_angle_deg);
Global_VP5_y = VP5 * sind(Global_VP5_angle_deg);

Global_F_out_P1_x = F_out_P1 * cosd(Global_VP1_angle_deg);
Global_F_out_P2_x = F_out_P2 * cosd(Global_VP2_angle_deg);
Global_F_out_P3_x = F_out_P3 * cosd(Global_VP3_angle_deg);
Global_F_out_P4_x = F_out_P4 * cosd(Global_VP4_angle_deg);
Global_F_out_P5_x = F_out_P5 * cosd(Global_VP5_angle_deg);
```

Plots

```
% Plotting omega vs theta2
figure;
plot(Global_theta2_deg_values, omega2_values, 'g-', 'LineWidth', 2);
hold on;
plot(Global_theta2_deg_values, omega3_values, 'b-', 'LineWidth', 2);
plot(Global_theta2_deg_values, omega4_values, 'r-', 'LineWidth', 2);

xLimits = get(gca, 'XLim');
plot(xLimits, [0 0], 'k--', 'LineWidth', 1);

title('ω vs. θ_2');
xlabel('θ_2 (degrees)');
ylabel('ω (rad/s)');
legend({'ω_2', 'ω_3', 'ω_4'}, 'Location', 'Best');
grid on;


% Plotting alpha vs theta2
figure;
plot(Global_theta2_deg_values, alpha2_values, 'g-', 'LineWidth', 2);
hold on;
plot(Global_theta2_deg_values, alpha3_values, 'b-', 'LineWidth', 2);
plot(Global_theta2_deg_values, alpha4_values, 'r-', 'LineWidth', 2);

title('α vs. θ_2');
xlabel('θ_2 (degrees)');
ylabel('α (rad/s^2)');
legend({'α_2', 'α_3', 'α_4'}, 'Location', 'Best');
grid on;


% Plotting Joint Forces vs theta2
figure;
plot(Global_theta2_deg_values, F12_values, 'g-', 'LineWidth', 2);
hold on;
plot(Global_theta2_deg_values, F32_values, 'b--', 'LineWidth', 2);
plot(Global_theta2_deg_values, F43_values, 'r-', 'LineWidth', 2);
plot(Global_theta2_deg_values, F14_values, 'c--', 'LineWidth', 2);

title('Joint Forces vs. θ_2');
xlabel('θ_2 (degrees)');
ylabel('Joint Force (kN)');
legend({'F12', 'F32', 'F43', 'F14'}, 'Location', 'Best');
grid on;
```

```
% Plotting Ms vs Theta2
figure;
plot(Global_theta2_deg_values, Ms_values, 'b-', 'LineWidth', 2);

title('Shaking Force vs. θ_2');
xlabel('θ_2 (degrees)');
ylabel('Shaking Force (kN)');
grid on;


% Plotting each F_Px value vs Theta2
figure;
hold on;
plot(Global_theta2_deg_values, F_P1_values / 1000, 'b--', 'LineWidth', 2);
plot(Global_theta2_deg_values, F_P2_values / 1000, 'g-', 'LineWidth', 2);
plot(Global_theta2_deg_values, F_P3_values / 1000, 'r--', 'LineWidth', 2);
plot(Global_theta2_deg_values, F_P4_values / 1000, 'c-', 'LineWidth', 2);
plot(Global_theta2_deg_values, F_P5_values / 1000, 'm--', 'LineWidth', 2);
hold off;

title('External Forces at Points P1 to P5 vs. θ_2');
xlabel('θ_2 (degrees)');
ylabel('Force (kN)');
legend({'F P1', 'F P2', 'F P3', 'F P4', 'F P5'}, 'Location', 'Best');
grid on;


% Plotting each Output force in x-direction vs Theta2
figure;
hold on;
plot(Global_theta2_deg_values, Global_F_out_P1_x_value, 'b-', 'LineWidth', 4);
plot(Global_theta2_deg_values, Global_F_out_P2_x_value, 'g-', 'LineWidth', 4);
plot(Global_theta2_deg_values, Global_F_out_P3_x_value, 'r-', 'LineWidth', 4);
plot(Global_theta2_deg_values, Global_F_out_P4_x_value, 'c-', 'LineWidth', 4);
plot(Global_theta2_deg_values, Global_F_out_P5_x_value, 'm-', 'LineWidth', 4);

xLimits = get(gca, 'XLim');
plot(xLimits, [0 0], 'k--', 'LineWidth', 1);
hold off;

title('Output Forces in x Direction at Points P1 to P5 vs. θ_2', 'FontSize', 14);
xlabel('θ_2 (degrees)', 'FontSize', 14);
ylabel('Force (kN)', 'FontSize', 14);
legend({'F out P_1', 'F out P_2', 'F out P_3', 'F out P_4', 'F out P_5'}, 'Location', 'Best', 'FontSize', 12);
grid on;
```

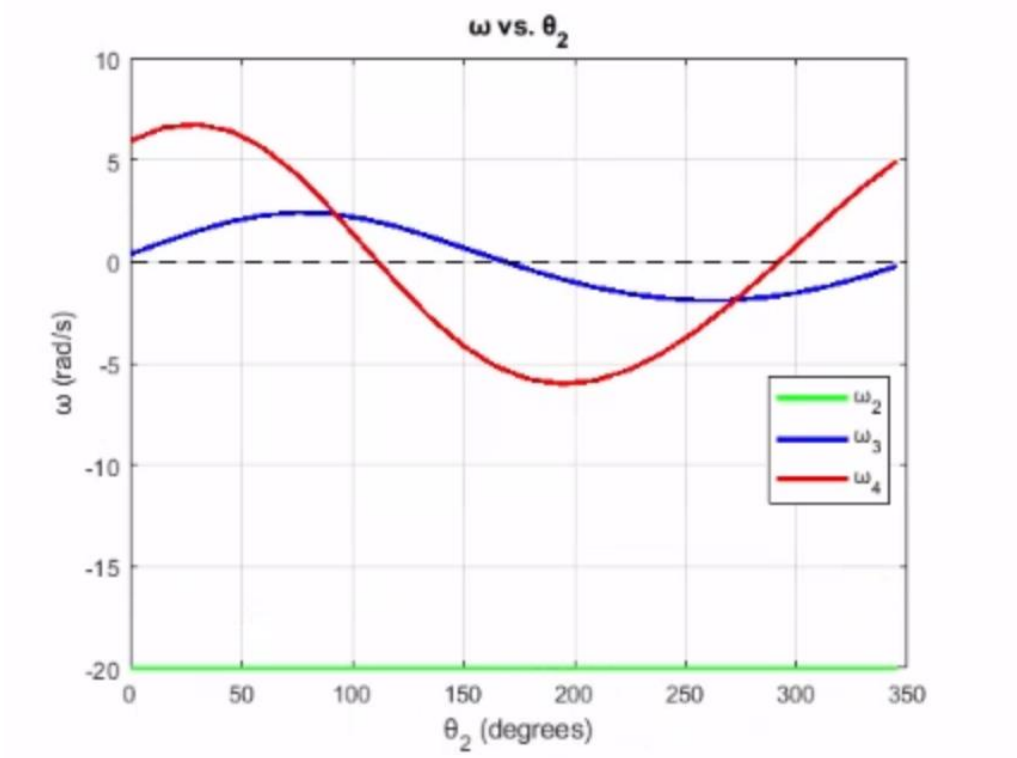
ω vs. θ2
ω (rad/s)
θ2 (degrees)
ω2
ω3
ω4

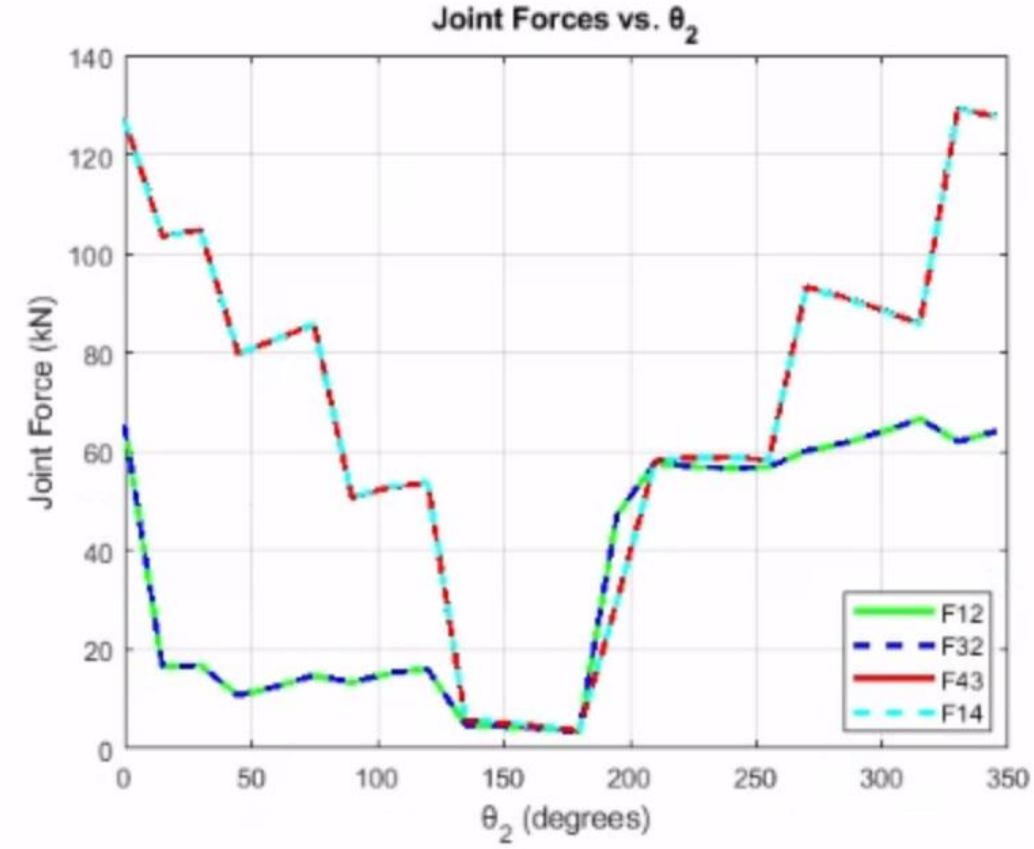
Joint Forces vs. θ2
Joint Force (kN)
θ2 (degrees)
F12
F32
F43
F14

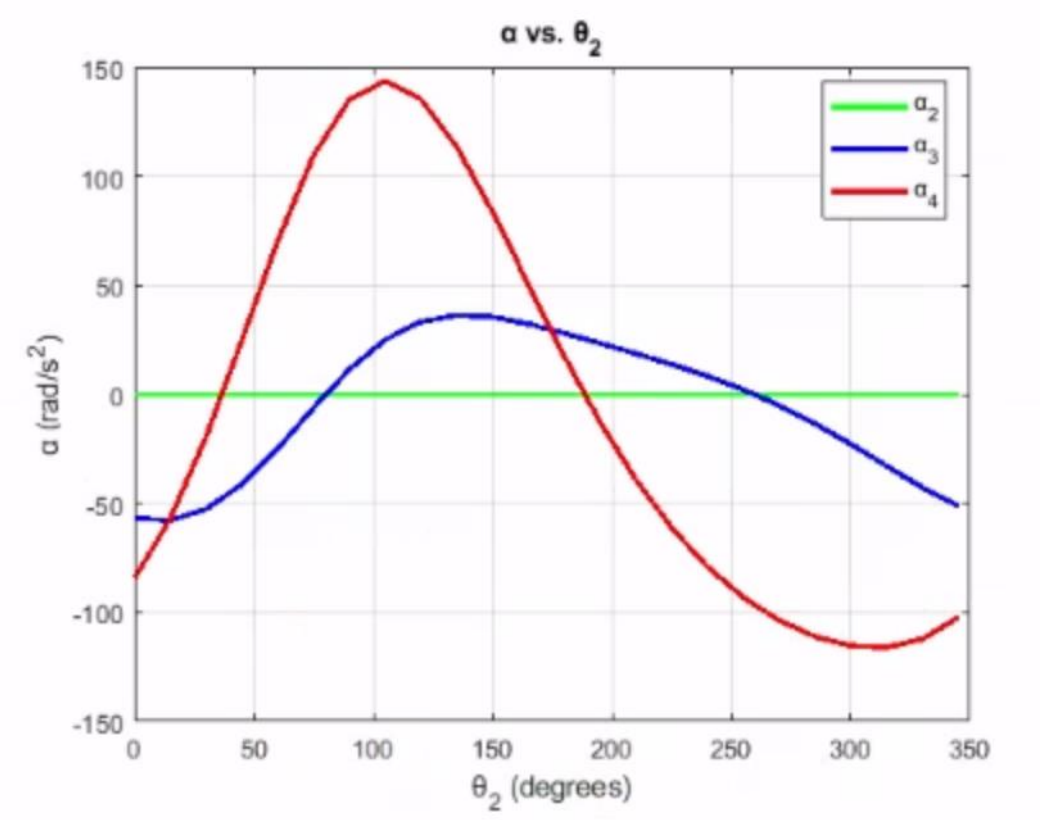
α vs. θ2
α2
α3
α4
α (rad/s2)
θ2 (degrees)
150
100
50
0
-50
-100
-150
0
50
100
150
200
250
300
350

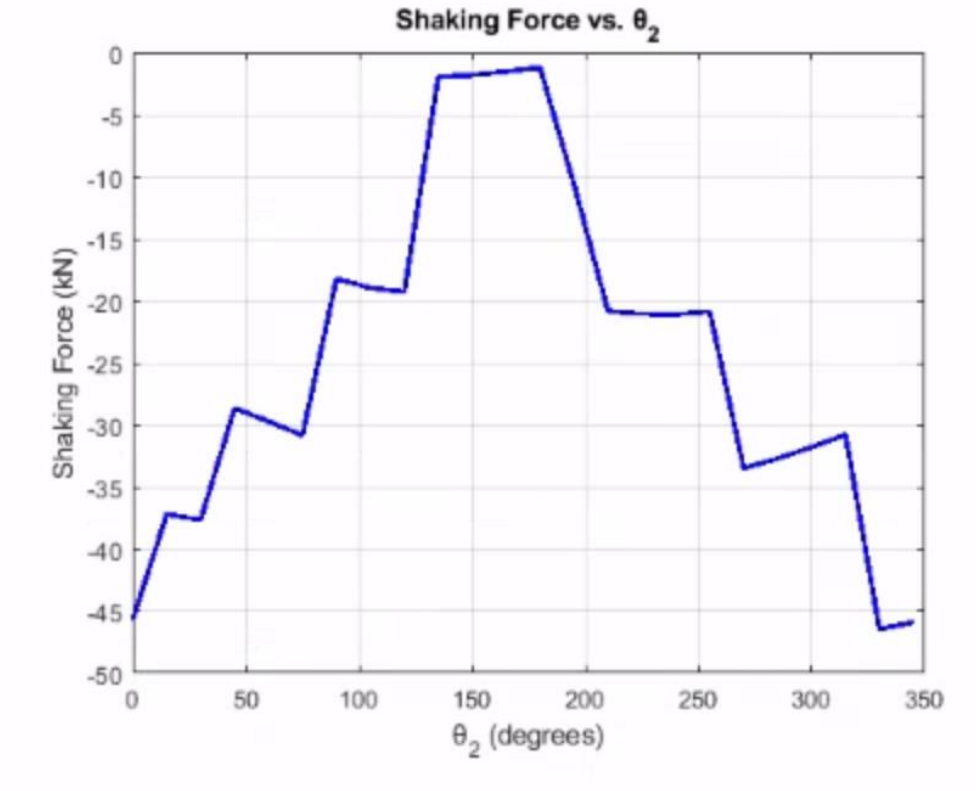
Shaking Force vs. θ2
Shaking Force (kN)
θ2 (degrees)
0
-5
-10
-15
-20
-25
-30
-35
-40
-45
-50
0
50
100
150
200
250
300
350

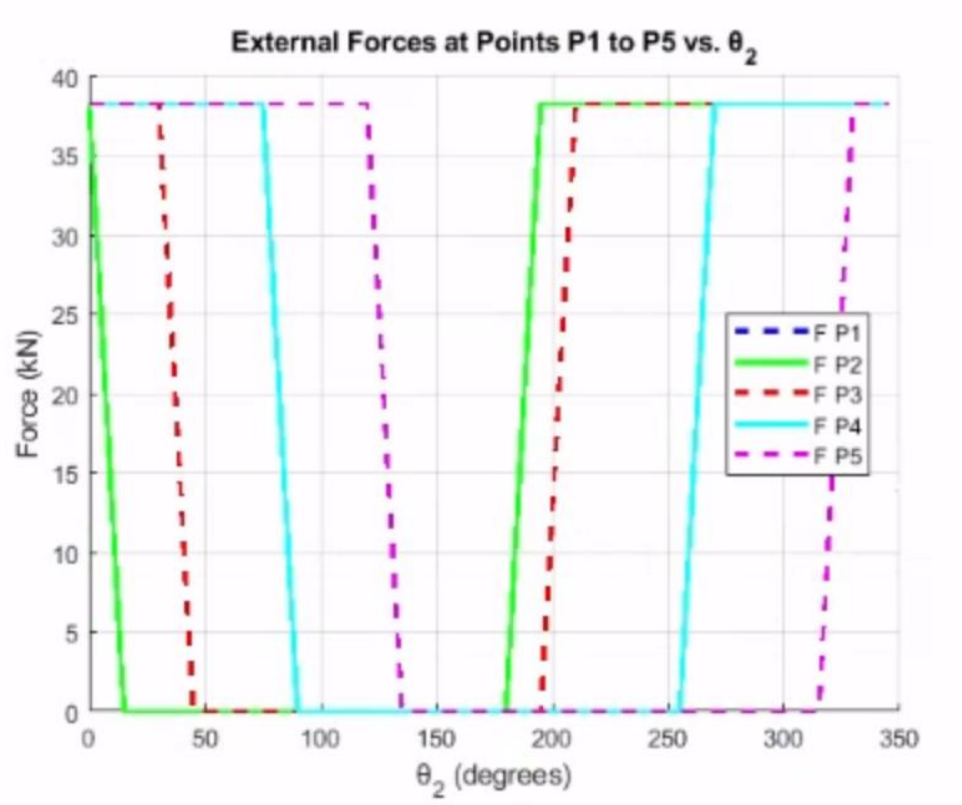
External Forces at Points P1 to P5 vs. θ2
Force (kN)
θ2 (degrees)
F P1
F P2
F P3
F P4
F P5

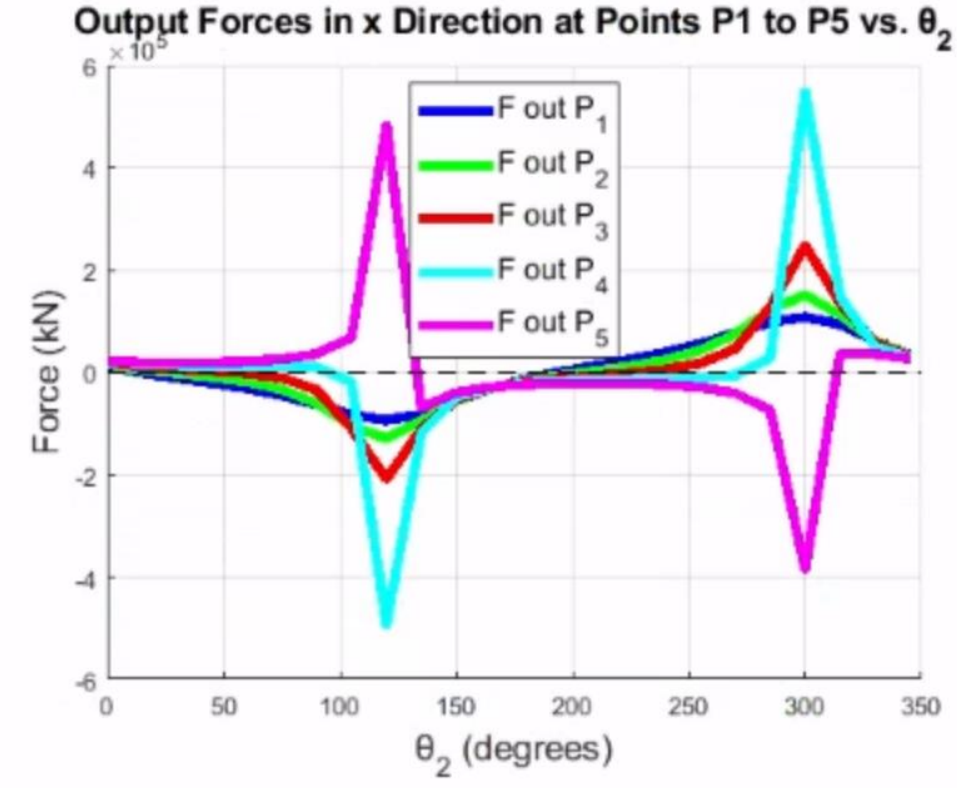
Output Forces in x Direction at Points P1 to P5 vs. θ2
×10^5
Force (kN)
θ2 (degrees)
F out P1
F out P2
F out P3
F out P4
F out P5

APPENDIX C

Jaw Crusher Goodman Factor of Safety Calculations MATLAB code – "JawCrusherConceptOneGoodmanFOS.m"

Torque Calcualtions

```
motor_power = 2200; % watts, power of the motor

speed_shaft_rpm = 190; % rpm, speed of the shaft
speed_shaft_rad = speed_shaft_rpm * 2 * pi() / 60; % rad/s, speed of the shaft

diameter_drive = 75/1000; % m, diameter of the driving pulley
diameter_driven = 315/1000; % m, diameter of the driven pulley
pulley_ratio = diameter_drive / diameter_driven; % ratio of driving to driven pulley diameters

speed_motor_rpm = speed_shaft_rpm*diameter_driven/diameter_drive; % rpm, speed of the motor
speed_motor_rad = speed_motor_rpm * 2 * pi / 60; % rad/s, speed conversion from RPM to rad/s

torque_drive = motor_power / speed_motor_rad; % Nm, calculated torque on the driving pulley
torque_driven = torque_drive / pulley_ratio; % Nm, calculated torque on the driven pulley
torque = torque_driven; % Nm, constant torque applied at the pulley

fprintf('Torque: %.2f Nm\n\n', torque);
```

```
Torque: 110.57 Nm
```

Forces Acting on Shaft calculations

```
% Known Values
radius = diameter_driven/2; % m, radius of the driven pulley
BeltAngle_deg = -20; % degrees, angle of the belt
percentage_difference = 0.15; % percentage difference between tensions P1 and P2

% External forces acting on swinging jaw
Force_z = 66*1000 ; % N, Maximum external forces acting on the shaft on z-axis
Force_y = -9*1000 ; % N, Maximum external forces acting on the shaft on y-axis

% Forces acting on pulley
P1 = torque / radius; % N, tension P1 on the pulley
P2 = percentage_difference * P1; % N, tension P2 on the pulley, a percentage of P1
BeltAngle_rad = BeltAngle_deg * pi / 180; % radians, belt angle conversion from degrees to radians
Ft = -(P1 + P2) * cos(BeltAngle_rad); % N, tangential force on the pulley
Fr = (P1 + P2) * sin(BeltAngle_rad); % N, radial force on the pulley

% Variables to solve for
syms Az Ay Dz Dy

% Known forces
By = Force_y/2; % N, y-component of total force on bearing B
Bz = Force_z/2; % N, z-component of total force on bearing B
Cy = By; % N, y-component of total force on bearing C
Cz = Bz; % N, z-component of total force on bearing B
Ey = Fr; % N, y-component of total force on driven pulley
Ez = Ft; % N, z-component of total force on driven pulley

% Distance from origin to where forces are applied
d_A = 35/1000; % m, Distance to center of bearing A from origin
d_B = 108/1000; % m, Distance to center of bearing B from origin
d_C = 561/1000; % m, Distance to center of bearing C from origin
d_D = 635/1000; % m, Distance to center of bearing D from origin
d_E = 715/1000; % m, Distance to center of driven pulley from origin

% Sum of Forces on z-axis
eq1 = Az + Bz + Cz + Dz + Ez == 0;

% Sum of Forces on y-axis
eq2 = Ay + By + Cy + Dy + Ey == 0;
```

```
% Sum of Moments about point A on z-axis (y-x)
eq3 = (Bz * d_B) + (Cz * d_C) + (Dz * d_D) + (Ez *d_E)  == 0;

% Sum of Moments about point A on y-axis (z-x)
eq4 = (By * d_B) + (Cy * d_C)+ (Dy * d_D) + (Ey * d_E) == 0;

% Solve the system of equations
S = solve([eq1, eq2, eq3, eq4], [Az, Ay, Dz, Dy]);

fprintf('Torque = %.2f Nm\n\n', torque);
fprintf('Ft = %.2f kN\n', Ez/1000);
fprintf('Fr =  %.2f kN\n\n', Ey/1000);
fprintf('Az = %.2f kN\n', double(S.Az)/1000);
fprintf('Ay = %.2f kN\n\n', double(S.Ay)/1000);
fprintf('Bz = %.2f kN\n', Bz/1000);
fprintf('By: %.2f kN\n\n', By/1000);
fprintf('Cz = %.2f kN\n', Cz/1000);
fprintf('Cy: %.2f kN\n\n', Cy/1000);
fprintf('Dz = %.2f kN\n', double(S.Dz)/1000);
fprintf('Dy = %.2f kN\n\n', double(S.Dy)/1000);
```

```
Torque = 110.57 Nm

Ft = -0.76 kN
Fr =  -0.28 kN

Az = -31.33 kN
Ay = 4.22 kN

Bz = 33.00 kN
By: -4.50 kN

Cz = 33.00 kN
Cy: -4.50 kN

Dz = -33.91 kN
Dy = 5.05 kN
```

Shaft Deflection, Slope and Moment Calculations

```
% checking xy plane deflections/slopes
%Forces
F=[By, Cy, Ey]; % N, magnitudes of forces applied
Floc=[d_B, d_C, d_E]; % m, location of where forces are applied (d_B, d_C, d_E)
d=[55, 65, 55]/1000; % m, diameters of the shaft
dloc=[0, 80, 590]/1000; % m, locations of start of diameter change
Rloc=[d_A, d_D]; % m, locations of the center of supporting bearings
L1 = 0.74; % m, length of the shaft
[x1,y1,dydx1, M1, MdEI1, Ry, diam1, EI1]=ShaftDeflectionMetric(F,Floc,d,dloc,Rloc,L1);


% checking xz plane deflections/slopes
%Forces
F=[Bz, Cz, Ez]; % N, magnitudes of forces are applied
Floc=[d_B, d_C, d_E];% m, location of where forces are applied
[x2,y2,dydx2, M2, MdEI2, Rz, diam2, EI2]=ShaftDeflectionMetric(F,Floc,d,dloc,Rloc,L1);


% vector summing to find total slopes and deflections
x=x1; %should be same x value for both dimensions
y=sqrt(y1.^2+y2.^2);
dydx=sqrt(dydx1.^2+dydx2.^2);
M=sqrt(M1.^2+M2.^2);

figure
subplot(3,1,1)
plot(x,diam1/2,'r')
title('Half-Shaft geometry')
xlim([0,L1])
ylabel('Radius')

subplot(3,1,2)
plot(x,y,'g')
xlim([0,L1])
title('magnitude of total deflection')
ylabel('Deflection')
```

```
subplot(3,1,3)
plot(x,dydx,'b')
xlim([0,L1])
title('magnitude of total Slope')
ylabel('Slope (rad)')

figure
plot(x,M)
xlabel('shaft length (m)')
ylabel('Moment (Nm)')

% Critical points
selected_points = [35, 108, 561, 715, 80, 590]/1000; % m;
% Find Corresponding Indices
[~, indices] = min(abs(x - selected_points.'), [], 2);

for i = 1:length(indices)
    fprintf('Deflection and slope at critical points\n')
    fprintf('At x = %.3f m:\n', selected_points(i));
    fprintf('Deflection = %.6f m\n', y(indices(i)));
    fprintf('Slope = %.6f rad\n', dydx(indices(i)));
    fprintf('Moment = %.2f Nm\n\n', M(indices(i)));
end
```

```
Deflection and slope at critical points
At x = 0.035 m:
Deflection = 0.000000 m
Slope = 0.003891 rad
Moment = 0.00 Nm

Deflection and slope at critical points
At x = 0.108 m:
Deflection = 0.000264 m
Slope = 0.003198 rad
Moment = 2442.30 Nm

Deflection and slope at critical points
At x = 0.561 m:
Deflection = 0.000269 m
Slope = 0.003203 rad
Moment = 2510.73 Nm

Deflection and slope at critical points
At x = 0.715 m:
Deflection = 0.000317 m
Slope = 0.003967 rad
Moment = 0.00 Nm

Deflection and slope at critical points
At x = 0.080 m:
Deflection = 0.000169 m
Slope = 0.003514 rad
Moment = 1505.53 Nm

Deflection and slope at critical points
At x = 0.590 m:
Deflection = 0.000171 m
Slope = 0.003539 rad
Moment = 1549.36 Nm
```

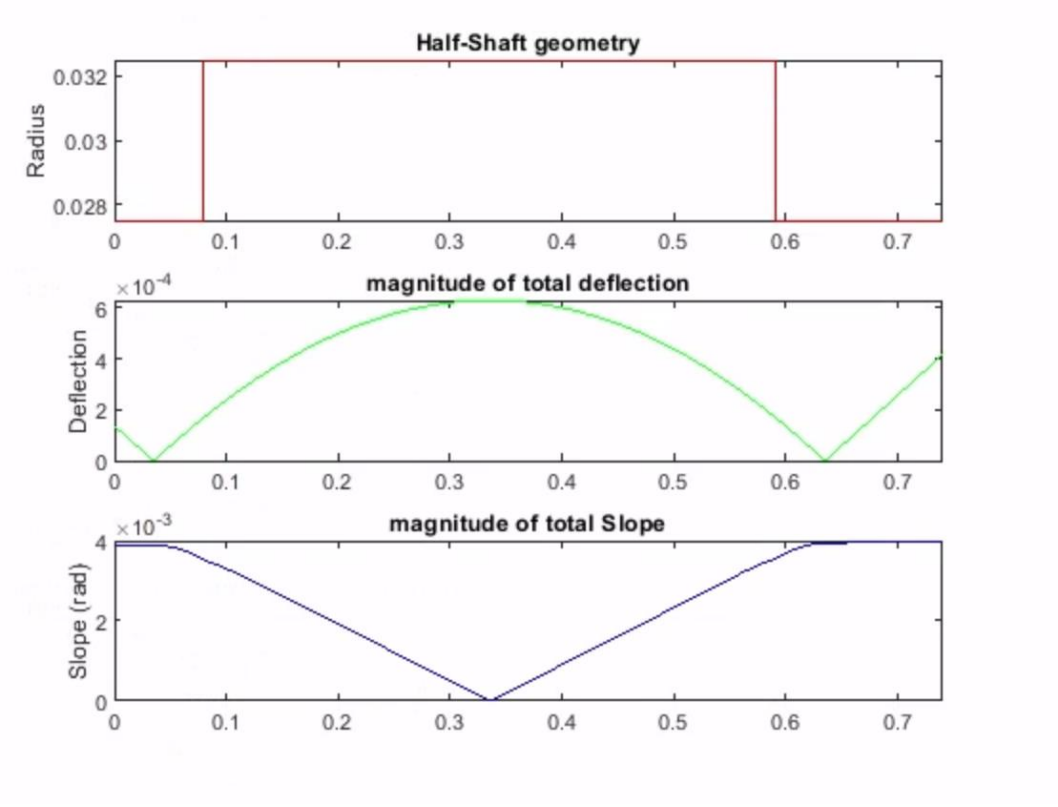
Half-Shaft geometry
Radius
0.032
0.03
0.028
0 0.1 0.2 0.3 0.4 0.5 0.6 0.7
magnitude of total deflection
×10^-4
Deflection
6
4
2
0
0 0.1 0.2 0.3 0.4 0.5 0.6 0.7
magnitude of total Slope
×10^-3
Slope (rad)
4
2
0
0 0.1 0.2 0.3 0.4 0.5 0.6 0.7

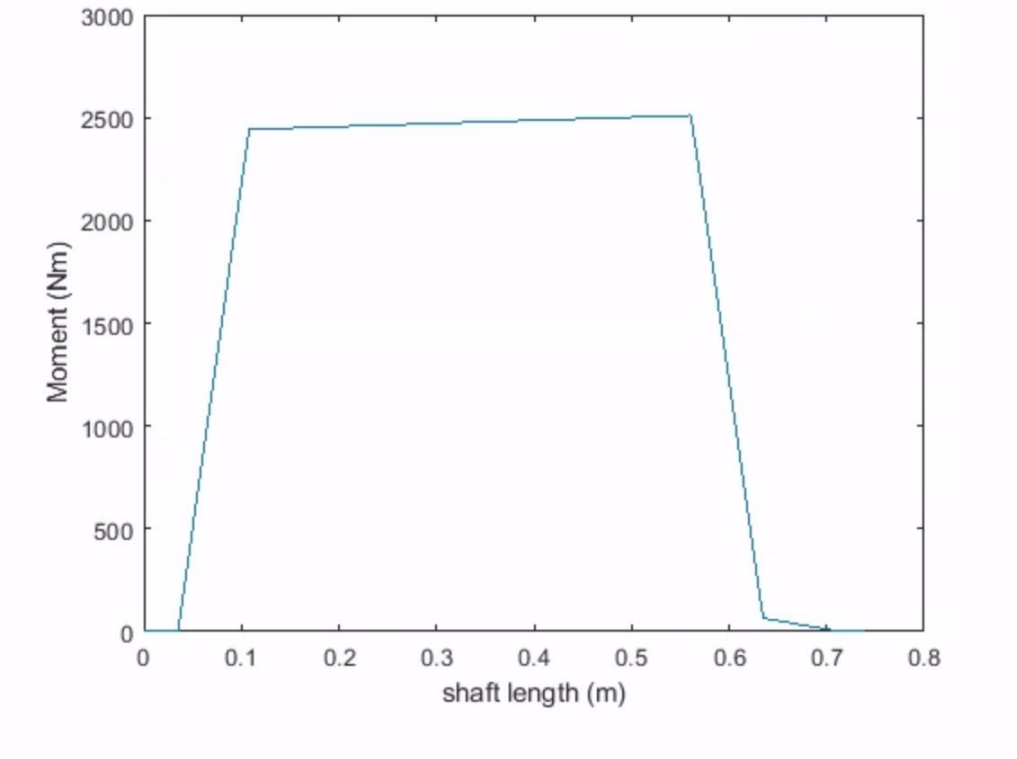
Moment (Nm)
3000
2500
2000
1500
1000
500
0
0 0.1 0.2 0.3 0.4 0.5 0.6 0.7 0.8
shaft length (m)

Factor of Safety Calculations

```
% Material properties and stress concentration factors - AISI 1020CD
Sut = 470e6; % Pa, Ultimate tensile strength
Sy = 390e6; % Pa, Yield strength
Se_prime = 0.5 * Sut; % Pa, Modified endurance limit

% Stress concentration factors and notch sensitivities
Kt_bending = 1.75;
q = 0.78; % Notch sensitivity for bending
Kt_shear = 1;
qs = 0.82; % Notch sensitivity for shear

Kf = 1 + q * (Kt_bending - 1);
Kfs = 1 + qs * (Kt_shear - 1);

% K factors
ka = 0.76; % Surface finish factor
kb = 0.86; % Size factor
kc = 1; % Load factor
kd = 1; % Temperature factor
ke = 0.814; % Reliability factor
kf = 1; % Miscellaneous-effects factor

% Adjusted Se using Marin factors
Se = ka * kb * kc * kd * ke * kf * Se_prime;

% Critical points data
critical_points = [150, 591]/1000; % m
diameters_at_critical_points = [55, 55]/1000; % m
M_max = [1500.20, 1447.28]; % Nm
M_min = [223.76, 211.77]; % Nm

fprintf('Factor of Safety Calculations:\n\n');
```

```
% Loop through each critical point to calculate FS
for i = 1:length(critical_points)
    % Diameter at the current critical point
    diameter_m = diameters_at_critical_points(i);

    % Moments at the current critical point
    M_a = (M_max(i) - M_min(i)) / 2;
    M_m = (M_max(i) + M_min(i)) / 2;

    % Bending and torsional stresses
    sigma_a = Kf * (32 * M_a) / (pi * diameter_m^3);
    sigma_m = Kf * (32 * M_m) / (pi * diameter_m^3);
    tau_a = Kfs * (16 * 0) / (pi * diameter_m^3);
    tau_m = Kfs * (16 * torque) / (pi * diameter_m^3);

    % Combined stresses for Goodman calculation
    A = sqrt(4*(Kf*M_a)^2 + 3*(Kfs*1.2)^2);
    B = sqrt(4*(Kf*M_m)^2 + 3*(Kfs*torque)^2);

    % Goodman and Yield FoS
    GoodmanFOS = ((pi * diameter_m^3) / 16) * ((A / Se) + (B / Sut))^-1;
    sigma_ar = (sigma_a/1e6)/(1-(sigma_m/1e6)/(Sut/1e6));
    f = 0.85;
    a = (f * (Sut/1e6))^2 / (Se/1e6);
    b = -1/3 * log((f*(Sut/1e6))/(Se_prime/1e6));
    N = ((sigma_ar)/a)^(1/b);


    sigma_prime_max = sqrt((sigma_m + sigma_a)^2 + 3 * (tau_m + tau_a)^2);
    YieldFOS = Sy / sigma_prime_max;

    % Gerber FoS
    GerberFOS = ((8 * A) / (pi * diameter_m^3 * Se) * (1 + sqrt(1 + (2 * B * Se / (A * Sut))^2)))^-1;
```

```
Factor of Safety Calculations:

For critical point at x = 0.15 m:
Diameter = 55.00 mm
Goodman Factor Of Safety = 1.4842
Gerber Factor Of Safety = 1.8086
Estimated life = 8.88 * 10^6
Yield Factor Of Safety = 2.68

For critical point at x = 0.59 m:
Diameter = 55.00 mm
Goodman Factor Of Safety = 1.5357
Gerber Factor Of Safety = 1.8705
Estimated life = 11.18 * 10^6
Yield Factor Of Safety = 2.77
```

APPENDIX D

Hammer Mill Crusher Goodman Factor of Safety Calculations MATLAB code: "HammerMillGoodmanFOS.m"

Centrifugal Force Exerted by the Hammers

Parameters

```
Nh = 16; % Number of hammers
mh = 0.52; % kg, Hammer mass
rh = 0.117; % m, Radius of hammer
N = 600; % rpm, rotating velocity of the shaft
omega_h = 2 * pi * N / 60; % rad/s, angular velocity of the shaft

% Calculate the centrifugal force of the hammers
Fh = Nh * mh * rh * omega_h^2;

% Display the result
fprintf('The centrifugal force exerted by the hammers is %.2f N\n\n', Fh);
```

```
The centrifugal force exerted by the hammers is 3842.99 N
```

Torque Calculations

```
motor_power = P; % watts, power of the motor

speed_shaft_rpm = 600; % rpm, speed of the shaft
speed_shaft_rad = speed_shaft_rpm * 2 * pi() / 60; % rad/s, speed of the shaft

diameter_drive = 100/1000; % m, diameter of the driving pulley
diameter_driven = 100/1000; % m, diameter of the driven pulley
pulley_ratio = diameter_drive / diameter_driven; % ratio of driving to driven pulley diameters

speed_motor_rpm = speed_shaft_rpm * pulley_ratio; % rpm, speed of the motor corrected
speed_motor_rad = speed_motor_rpm * 2 * pi / 60; % rad/s, speed conversion from RPM to rad/s

torque_drive = motor_power / speed_motor_rad; % Nm, calculated torque on the driving pulley
torque_driven = torque_drive * pulley_ratio; % Nm, calculated torque on the driven pulley, corrected
torque = torque_driven; % Nm, constant torque applied at the pulley

fprintf('Torque: %.2f Nm\n\n', torque);
```

```
Torque: 35.01 Nm
```

Forces Acting on Shaft calculations

```
% Known Values
radius = diameter_driven / 2; % m, radius of the driven pulley
BeltAngle_deg = -20; % degrees, angle of the belt, negative to indicate direction
percentage_difference = 0.15; % percentage difference between tensions P1 and P2
WeightofHammerMechanism = 13.210 * 9.81; % N, weight of the swinging jaw + impact plate

% Forces acting on pulley (Euler-Eytelwein Formula)
P1 = torque / radius; % N, tension P1 on the pulley
P2 = P1 - (percentage_difference * P1); % N, tension P2 on the pulley, a corrected calculation
BeltAngle_rad = BeltAngle_deg * pi / 180; % radians, belt angle conversion from degrees to radians
Ft = -(P1 + P2) * cos(BeltAngle_rad); % N, tangential force on the pulley
Fr = (P1 + P2) * sin(BeltAngle_rad); % N, radial force on the pulley

% Variables to solve for
syms Az Ay Gz Gy

% Known forces
F_pulley_y = Fr; % N, y-component of total force on driven pulley
F_pulley_z = Ft; % N, z-component of total force on driven pulley
By = WeightofHammerMechanism/5; % N, y-component of total force on hammer mechanism
Bz = 0; % N, z-component of total force on hammer mechanism
Cy = WeightofHammerMechanism/5; % N, y-component of total force on hammer mechanism
Cz = 0; % N, z-component of total force on hammer mechanism
Dy = WeightofHammerMechanism/5; % N, y-component of total force on hammer mechanism
Dz = 0; % N, z-component of total force on hammer mechanism
Ey = WeightofHammerMechanism/5; % N, y-component of total force on hammer mechanism
Ez = 0; % N, z-component of total force on hammer mechanism
Fy = WeightofHammerMechanism/5; % N, y-component of total force on hammer mechanism
Fz = 0; % N, z-component of total force on hammer mechanism

% Distance from origin to where forces are applied
d_pulley = 25/1000; % m, Distance to center of driven pulley from origin
d_A = 103/1000; % m, Distance to center of bearing A from origin
d_B = 175/1000; % m, Distance to center of Disc 1 of hammer mechanism from origin
d_C = 210/1000; % m, Distance to center of Disc 2 of hammer mechanism from origin
d_D = 245/1000; % m, Distance to center of Disc 3 of hammer mechanism from origin
d_E = 280/1000; % m, Distance to center of Disc 4 of hammer mechanism from origin
d_F = 315/1000; % m, Distance to center of Disc 5 of hammer mechanism from origin
d_G = 385/1000; % m, Distance to center of bearing G from origin
```

```
% Sum of Forces on z-axis
eq1 = F_pulley_z - Az + Bz + Cz + Dz + Ez + Fz - Gz == 0;

% Sum of Forces on y-axis
eq2 = -F_pulley_y + Ay - By - Cy - Dy - Ey - Fy + Gy == 0;

% Sum of Moments about point A on z-axis (y-x)
eq3 = (F_pulley_z * (-d_A + d_pulley)) + (Bz * d_B) + (Cz * d_C) + (Dz * d_D) + (Ez * d_E) + (Fz * d_F) + (-Gz * d_G) == 0;

% Sum of Moments about point A on y-axis (z-x)
eq4 = (-F_pulley_y * (-d_A + d_pulley)) + (-By * d_B) + (-Cy * d_C) + (-Dy * d_D) + (-Ey * d_E) + (-Fy * d_F) + (Gy * d_G) == 0;

% Solve the system of equations
S = solve([eq1, eq2, eq3, eq4], [Az, Ay, Gz, Gy]);

fprintf('Torque = %.2f Nm\n\n', torque);
fprintf('Ft = %.2f kN\n', F_pulley_z/1000);
fprintf('Fr =  %.2f kN\n\n', F_pulley_y/1000);
fprintf('Az = %.2f kN\n', double(S.Az)/1000);
fprintf('Ay = %.2f kN\n\n', double(S.Ay)/1000);
fprintf('Bz = %.2f kN\n', Bz/1000);
fprintf('By = %.2f kN\n\n', By/1000);
fprintf('Cz = %.2f kN\n', Cz/1000);
fprintf('Cy = %.2f kN\n\n', Cy/1000);
fprintf('Dz = %.2f kN\n', Dz/1000);
fprintf('Dy = %.2f kN\n\n', Dy/1000);
fprintf('Ez = %.2f kN\n', Ez/1000);
fprintf('Ey = %.2f kN\n\n', Ey/1000);
fprintf('Fz = %.2f kN\n', Fz/1000);
fprintf('Fy = %.2f kN\n\n', Fy/1000);
fprintf('Gz = %.2f kN\n', double(S.Gz)/1000);
fprintf('Gy = %.2f kN\n\n', double(S.Gz)/1000);
```

```
Torque = 35.01 Nm

Ft = -1.22 kN
Fr =  -0.44 kN

Az = -1.46 kN
Ay = -0.49 kN

Bz = 0.00 kN
By = 0.03 kN

Cz = 0.00 kN
Cy = 0.03 kN

Dz = 0.00 kN
Dy = 0.03 kN

Ez = 0.00 kN
Ey = 0.03 kN

Fz = 0.00 kN
Fy = 0.03 kN

Gz = 0.25 kN
Gy = 0.25 kN
```

Shaft Deflection, Slope and Moment Calculations

```
% checking xy plane deflections/slopes
%Forces
F=[Fr ,Bz, Cz, Dz, Ez, Fz]; % N, magnitudes of forces applied
Floc=[d_pulley, d_B, d_C, d_D, d_E, d_F]; % m, location of where forces are applied (d_B, d_C, d_pulley)
d=[30, 40, 30]/1000; % m, diameters of the shaft
dloc=[0, 150, 320]/1000; % m, locations of start of diameter change
Rloc=[d_A, d_G]; % m, locations of the center of supporting bearings
L1 = 415/1000; % m, length of the shaft
[x1,y1,dydx1, M1, MdEI1, Ry, diam1, EI1]=ShaftDeflectionMetric(F,Floc,d,dloc,Rloc,L1);


% checking xz plane deflections/slopes
%Forces
F=[Ft ,By, Cy, Dy, Ey, Fy]; % N, magnitudes of forces are applied
Floc=[d_pulley, d_B, d_C, d_D, d_E, d_F];% m, location of where forces are applied
[x2,y2,dydx2, M2, MdEI2, Rz, diam2, EI2]=ShaftDeflectionMetric(F,Floc,d,dloc,Rloc,L1);


% vector summing to find total slopes and deflections
x=x1; %should be same x value for both dimensions
y=sqrt(y1.^2+y2.^2);
dydx=sqrt(dydx1.^2+dydx2.^2);
M=sqrt(M1.^2+M2.^2);

figure
subplot(3,1,1)
plot(x,diam1/2,'r')
title('Half-Shaft geometry')
xlim([0,L1])
ylabel('Radius')

subplot(3,1,2)
plot(x,y,'g')
xlim([0,L1])
title('magnitude of total deflection')
ylabel('Deflection')

subplot(3,1,3)
plot(x,dydx,'b')
xlim([0,L1])
title('magnitude of total Slope')
ylabel('Slope (rad)')
```

```
figure
plot(x,M)
xlabel('shaft length (m)')
ylabel('Moment (Nm)')

% Critical points
selected_points = [15, 103, 149, 341, 385]/1000; % m;
% Find Corresponding Indices
[~, indices] = min(abs(x - selected_points.'), [], 2);

for i = 1:length(indices)
    fprintf('Deflection and slope at critical points\n')
    fprintf('At x = %.3f m:\n', selected_points(i));
    fprintf('Deflection = %.6f m\n', y(indices(i)));
    fprintf('Slope = %.6f rad\n', dydx(indices(i)));
    fprintf('Moment = %.2f Nm\n\n', M(indices(i)));
end
```

```
Deflection and slope at critical points
At x = 0.015 m:
Deflection = 0.000098 m
Slope = 0.001255 rad
Moment = 0.00 Nm

Deflection and slope at critical points
At x = 0.103 m:
Deflection = 0.000000 m
Slope = 0.000760 rad
Moment = 101.05 Nm

Deflection and slope at critical points
At x = 0.149 m:
Deflection = 0.000022 m
Slope = 0.000215 rad
Moment = 87.36 Nm

Deflection and slope at critical points
At x = 0.341 m:
Deflection = 0.000013 m
Slope = 0.000255 rad
Moment = 18.49 Nm

Deflection and slope at critical points
At x = 0.385 m:
Deflection = 0.000000 m
Slope = 0.000306 rad
Moment = 0.00 Nm
```

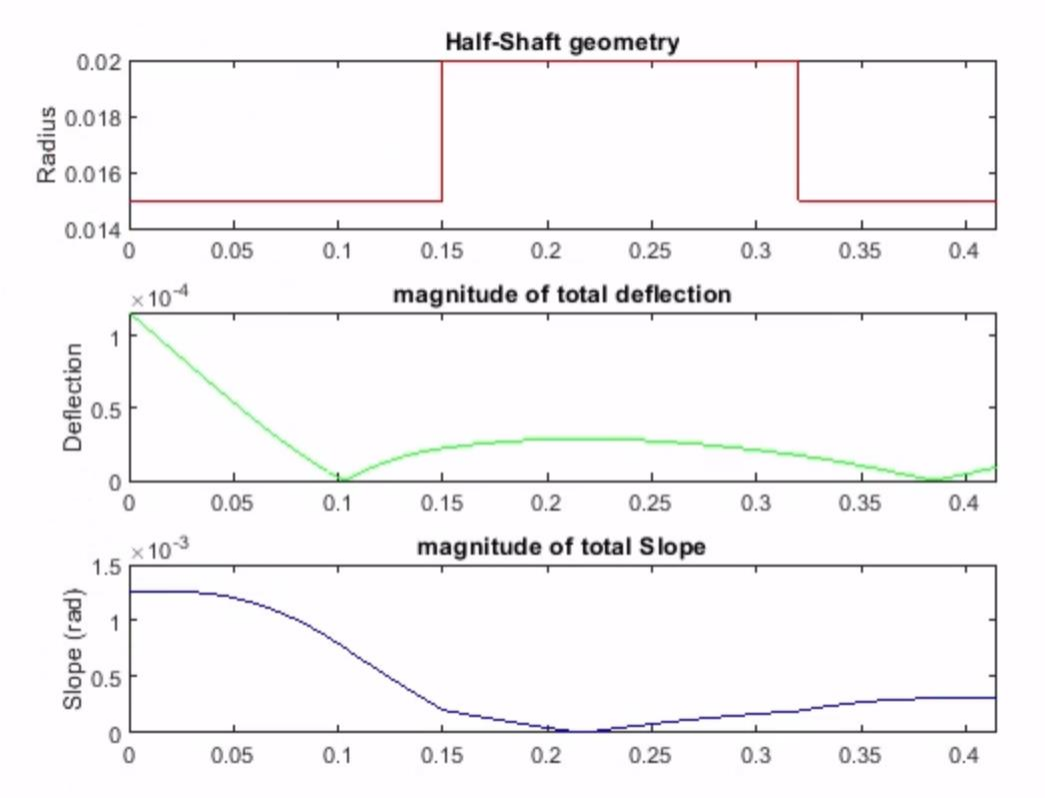
Half-Shaft geometry
Radius
0.02
0.018
0.016
0.014
0
0.05
0.1
0.15
0.2
0.25
0.3
0.35
0.4
magnitude of total deflection
×10^-4
Deflection
1
0.5
0
magnitude of total Slope
×10^-3
Slope (rad)
1.5
1
0.5
0

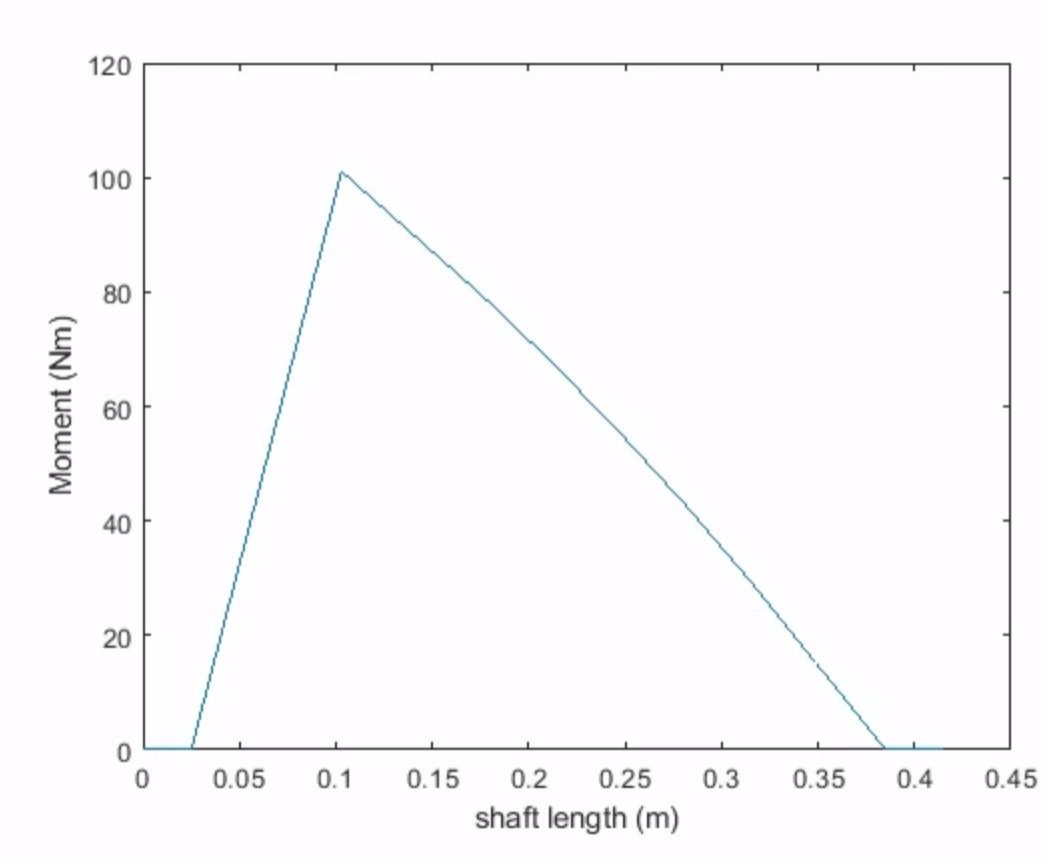
Moment (Nm)
120
100
80
60
40
20
0
0
0.05
0.1
0.15
0.2
0.25
0.3
0.35
0.4
0.45
shaft length (m)

Factor of Safety Calculations

```
% Material properties and stress concentration factors - AISI 1020CD
Sut = 470e6; % Pa, Ultimate tensile strength
Sy = 390e6; % Pa, Yield strength
Se_prime = 0.5 * Sut; % Pa, Modified endurance limit

% Stress concentration factors and notch sensitivities
Kt_bending = 1.75;
q = 0.78; % Notch sensitivity for bending
Kt_shear = 1;
qs = 0.82; % Notch sensitivity for shear

Kf = 1 + q * (Kt_bending - 1);
Kfs = 1 + qs * (Kt_shear - 1);

% K factors
ka = 0.76; % Surface finish factor
kb = 0.86; % Size factor
kc = 1; % Load factor
kd = 1; % Temperature factor
ke = 0.814; % Reliability factor
kf = 1; % Miscellaneous-effects factor

% Adjusted Se using Marin factors
Se = ka * kb * kc * kd * ke * kf * Se_prime;

% Critical points data
critical_points = [103, 385]/1000; % m
diameters_at_critical_points = [30, 30]/1000; % m
M_max = [101.05, 0]; % Nm
M_min = [101.05, 0]; % Nm
T_max = [torque + StartUpTorque, torque + StartUpTorque];
T_min = [torque, torque];

fprintf('Factor of Safety Calculations:\n\n');
```

```
% Loop through each critical point to calculate FS
for i = 1:length(critical_points)
    % Diameter at the current critical point
    diameter_m = diameters_at_critical_points(i);

    % Moments at the current critical point
    M_a = (M_max(i) - M_min(i)) / 2;
    M_m = (M_max(i) + M_min(i)) / 2;
    T_a = (T_max(i) - T_min(i)) / 2;
    T_m = (T_max(i) + T_min(i)) / 2;

    % Bending and torsional stresses (simplified)
    sigma_a = Kf * (32 * M_a) / (pi * diameter_m^3);
    sigma_m = Kf * (32 * M_m) / (pi * diameter_m^3);
    tau_a = Kfs * (16 * T_a) / (pi * diameter_m^3);
    tau_m = Kfs * (16 * T_m) / (pi * diameter_m^3);

    % Combined stresses for Goodman calculation
    A = sqrt(4*(Kf*M_a)^2 + 3*(Kfs*T_a)^2);
    B = sqrt(4*(Kf*M_m)^2 + 3*(Kfs*T_m)^2);

    % Goodman and Yield FoS
    GoodmanFOS = ((pi * diameter_m^3) / 16) * ((A / Se) + (B / Sut))^-1;
    sigma_ar = (sigma_a/1e6)/(1-(sigma_m/1e6)/(Sut/1e6));
    f = 0.85;
    a = (f * (Sut/1e6))^2 / (Se/1e6);
    b = -1/3 * log((f*(Sut/1e6))/(Se_prime/1e6));
    N = ((sigma_ar)/a)^(1/b);


    sigma_prime_max = sqrt((sigma_m + sigma_a)^2 + 3 * (tau_m + tau_a)^2);
    YieldFOS = Sy / sigma_prime_max;

    % Gerber FoS
    GerberFOS = ((8 * A) / (pi * diameter_m^3 * Se) * (1 + sqrt(1 + (2 * B * Se / (A * Sut))^2)))^-1;

    % Display results
    fprintf('For critical point at x = %.2f m:\n', critical_points(i));
    fprintf('Diameter = %.2f mm\n', diameter_m * 1000);
    fprintf('Goodman Factor Of Safety = %.4f\n', GoodmanFOS);
    fprintf('Gerber Factor Of Safety = %.4f\n', GerberFOS);
    fprintf('Estimated life = %.2f * 10^6\n', N/1e6);
    fprintf('Yield Factor Of Safety = %.2f\n\n', YieldFOS);
end
```

```
Factor of Safety Calculations:

For critical point at x = 0.10 m:
Diameter = 30.00 mm
Goodman Factor Of Safety = 5.5744
Gerber Factor Of Safety = 6.3107
Estimated life = Inf * 10^6
Yield Factor Of Safety = 6.04

For critical point at x = 0.39 m:
Diameter = 30.00 mm
Goodman Factor Of Safety = 12.1569
Gerber Factor Of Safety = 15.1613
Estimated life = Inf * 10^6
Yield Factor Of Safety = 17.05
```

APPENDIX E

Sand Dryer Heat Calculations MATLAB code – "SandDryerHeat.m"

```
% Constants
L = 0.9; % m, length
W = 0.75; % m, width
H = 0.75; % m, height
V_container = L * W * H; % Volume of the container
moisture_content = 0.10; % Moisture content
k = 0.25; % W/mK, thermal conductivity of sand
cp_sand = 720; %  J/kgK, specific heat capacity of sand
cp_water = 4180; % J/kg·K, Specific heat capacity of water
rho_sand = 1800; % kg/m^3, density of sand
alpha = k / (cp_sand * rho_sand); % thermal diffusivity
T_initial = 20; % °C, initial temperature of sand
T_coil = 80; % °C, temperature of the water in the coil
L_vaporization = 2256e3; % J/kg, Latent heat of vaporization of water

Nx = 19; % number of grid points in X-direction
Ny = 19; % number of grid points in Y-direction
dx = L/Nx;
dy = W/Ny;
dt = 5;
t_final = 24*3600; % Seconds, Simulation time

% Water properties at 80°C
rho_water = 971.8; %  kg/m^3, Density of water
mu_water = 0.354e-3; %  Pa·s, Dynamic viscosity of water
k_water = 0.67; % W/m·K, Thermal conductivity of water
cp_water = 4180; % J/kg·K, Specific heat capacity
Pr_water = cp_water * mu_water / k_water; % Prandtl number

% Flow conditions
D = 0.02; % m, Diameter of the pipe
L_pipe = 0.75; % m, Length of the pipe where heat transfer is evaluated
A_cross_sectional = pi * (D/2)^2;
flow_rate = 0.01 / 1000; % m^3/s, Flow rate
v = flow_rate / A_cross_sectional; % Mean velocity of the fluid

% Reynolds number
Re = D * v * rho_water / mu_water;
```

```
% Determine flow regime and calculate Nusselt number (Nu)
if Re < 2300
    % Laminar flow
    Nu = 1.86 * (Re * Pr_water * (L_pipe / D))^(1/3);
elseif Re > 4000
    % Turbulent flow using Dittus-Boelter equation (for heating)
    Nu = 0.023 * Re^0.8 * Pr_water^0.4;
else
    % Transition region
    Nu_laminar = 1.86 * (Re * Pr_water * (L_pipe / D))^(1/3);
    Nu_turbulent = 0.023 * Re^0.8 * Pr_water^0.4;
    Nu = (Nu_laminar + Nu_turbulent) / 2;
end
```

```
% heat transfer coefficient
h_conv = Nu * k_water / D;

T = T_initial * ones(Nx, Ny); % initial temperature matrix

% Coil positions and initial temperatures
coil_columns = [5 10 15]; % columns with coils
for c = coil_columns
    T(:, c) = T_coil;
end


for t = 0:dt:t_final
    T_old = T;
    for i = 2:Nx-1
        for j = 2:Ny-1
            if ismember(j, coil_columns)
                q_prime = h_conv * pi * D * (T_coil - T_old(i, j));
                Q = q_prime * L_pipe * dt;
                delta_T = Q / (rho_sand * cp_sand * dx * dy * H);
                T(i, j) = T_old(i, j) + delta_T;
            else
                T(i, j) = T_old(i, j) + alpha * dt / dx^2 * (T_old(i+1, j) + T_old(i-1, j) - 4*T_old(i, j) + T_old(i, j+1) + T_old(i, j-1));
            end
        end
    end
```

```
    % Boundary conditions
    T(1, :) = T(2, :); % top boundary
    T(Nx, :) = T(Nx-1, :); % bottom boundary
    T(:, 1) = T(:, 2); % left boundary
    T(:, Ny) = T(:, Ny-1); % right boundary

    for c = coil_columns
        T(:, c) = T_coil;
    end
end

figure;
imagesc(T);
c = colorbar;
set(c, 'FontSize', 14);
title('Temperature Distribution in Sand after 24 hours (°C)', 'FontSize', 20);
xlabel('Column', 'FontSize', 14);
ylabel('Row', 'FontSize', 14);


V_zone = (L/Nx) * (W/Ny) * H; % Volume per zone

m_sand_zone = rho_sand * V_zone; % Mass of sand per zone
m_water_zone = 0.1 * m_sand_zone; % 10% moisture content

Q_evap = zeros(Nx, Ny); % Heat required to evaporate water in each zone
Q_generated = zeros(Nx, Ny); % Heat generated in each zone due to temperature change
```

```
for i = 1:Nx
    for j = 1:Ny
        % Heat required to evaporate water
        Q_evap(i, j) = m_water_zone * L_vaporization;

        % Change in temperature from initial to final
        Delta_T = T(i, j) - T_initial;

        % Heat generated in the zone due to temperature change
        Q_generated(i, j) = m_sand_zone * cp_sand * Delta_T;
    end
end

figure;
min_val = min(min([Q_evap, Q_generated]));
max_val = max(max([Q_evap, Q_generated]));

% Plot for heat required to evaporate water
subplot(1, 2, 1);
imagesc(Q_evap);
c = colorbar;
set(c, 'FontSize', 14);
caxis([min_val max_val]);
title('Heat Required to Evaporate Water in Each Zone (J)', 'FontSize', 20);
xlabel('Column', 'FontSize', 14);
ylabel('Row', 'FontSize', 14);
```

```
% Plot for heat generated in each zone
subplot(1, 2, 2);
imagesc(Q_generated);
c = colorbar;
set(c, 'FontSize', 14);
caxis([min_val max_val]);
title('Heat Generated in Each Zone (J)', 'FontSize', 20);
xlabel('Column', 'FontSize', 14);
ylabel('Row', 'FontSize', 14);
```

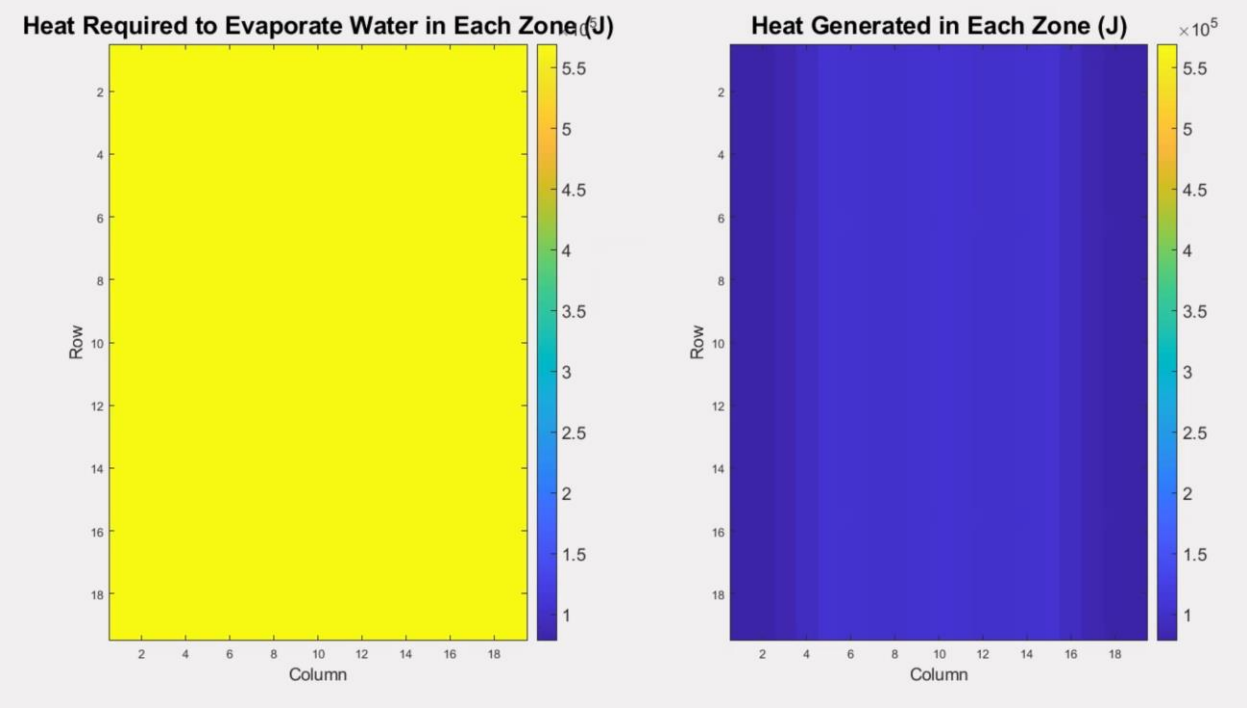
Heat Required to Evaporate Water in Each Zone (J)
×10^5
Row
Column
Heat Generated in Each Zone (J)
×10^5
Row
Column

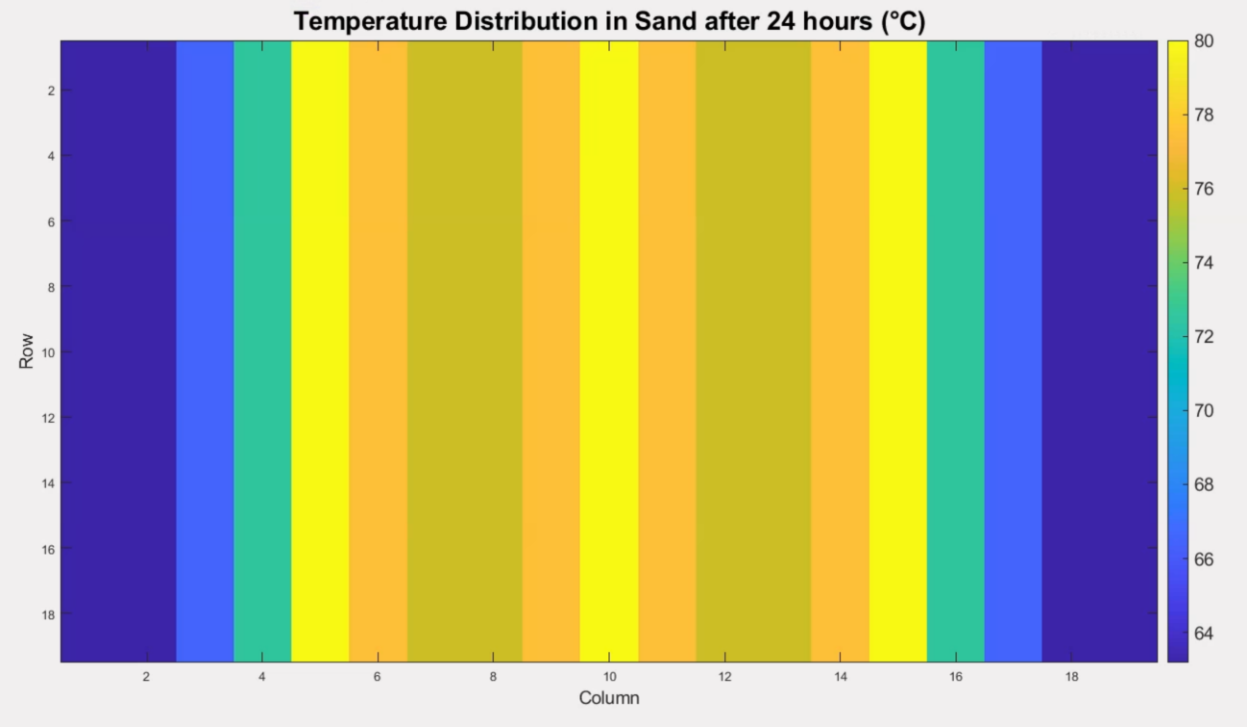
Temperature Distribution in Sand after 24 hours (°C)
Row
Column

APPENDIX F

Free Body Diagram of Jaw Crusher Shaft

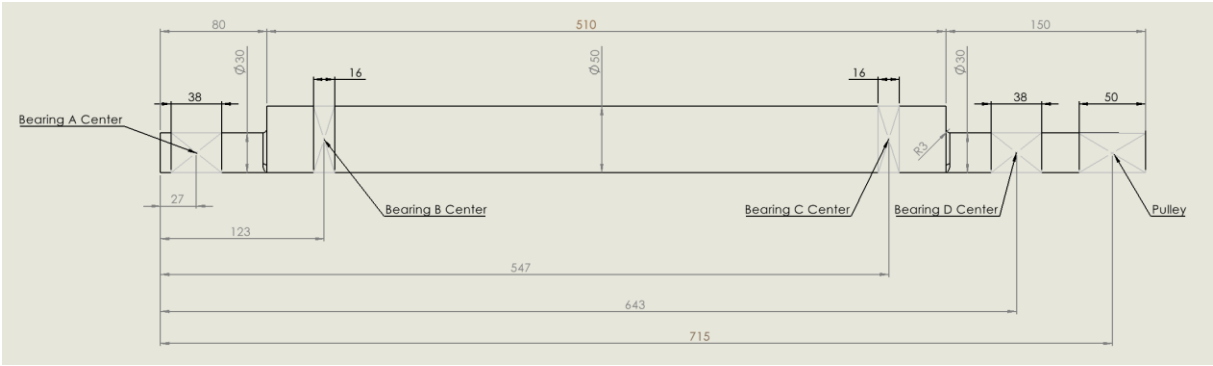

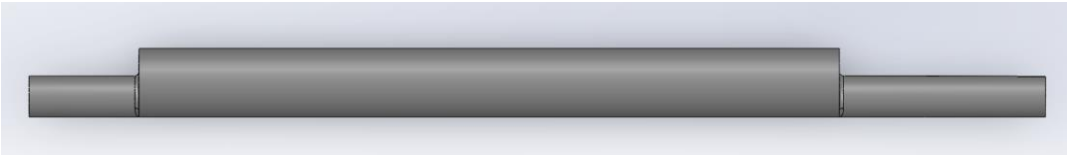

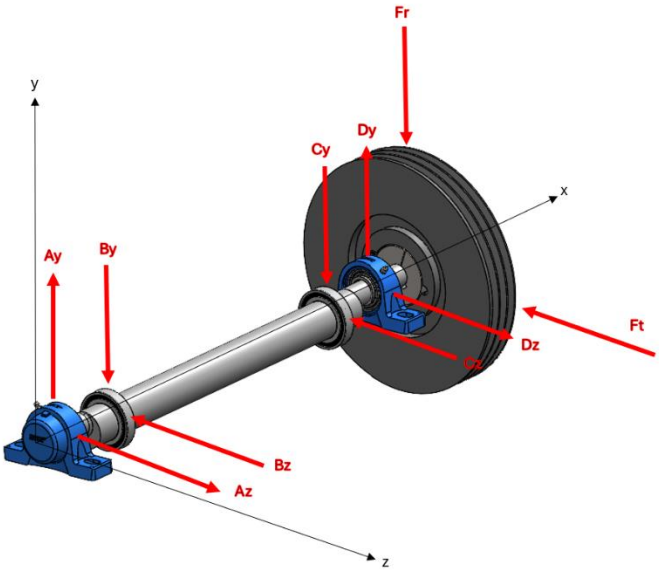

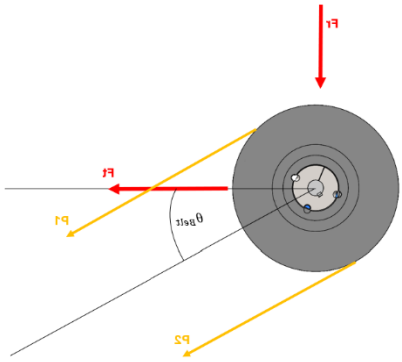

APPENDIX G

Free Body Diagram of Hammer Mill Crusher Shaft

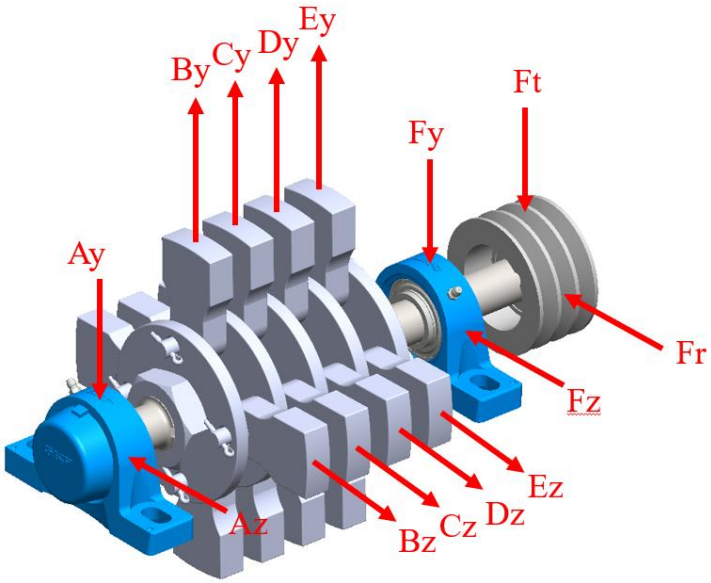

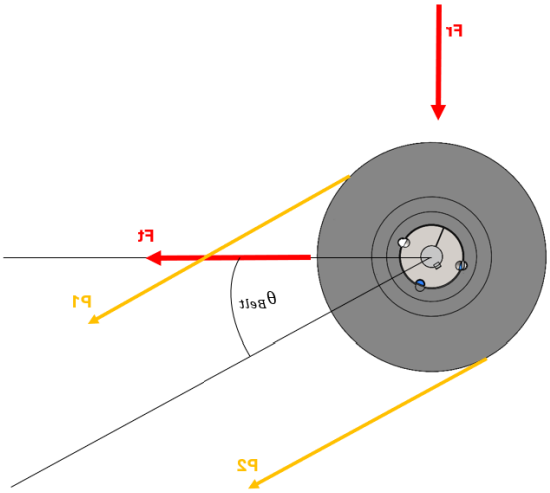

APPENDIX H

Weight Table for the Jaw Crusher, Hammer Mill Crusher, Crushers Support and the Sand Dryer.

Mass = 757.394577 kilograms

Volume = 0.209567 cubic meters

Surface area = 41.950406 square meters

Center of mass: (meters)
X = 0.440908
Y = 1.134634
Z = -0.730719

Principal axes of inertia and principal moments of inertia: (kilograms * square meters)
Taken at the center of mass.

Ix = (0.001062, 0.300164, 0.953887)	Px = 229.254212
Iy = (-0.424470, -0.863554, 0.272212)	Py = 916.360018
Iz = (0.905442, -0.405185, 0.126493)	Pz = 1032.994164

Moments of inertia: (kilograms * square meters)
Taken at the center of mass and aligned with the output coordinate system. (Using positive tensor notation.)

Lxx = 1011.978761	Lxy = 43.008880	Lxz = -12.661993
Lyx = 43.008880	Lyy = 873.601124	Lyz = 202.711982
Lzx = -12.661993	Lzy = 202.711982	Lzz = 293.028509

Moments of inertia: (kilograms * square meters)
Taken at the output coordinate system. (Using positive tensor notation.)

Ixx = 2391.454602	Ixy = 421.910065	Ixz = -256.679362
Iyx = 421.910065	Iyy = 1425.249691	Iyz = -425.242619
Izx = -256.679362	Izy = -425.242619	Izz = 1415.330797

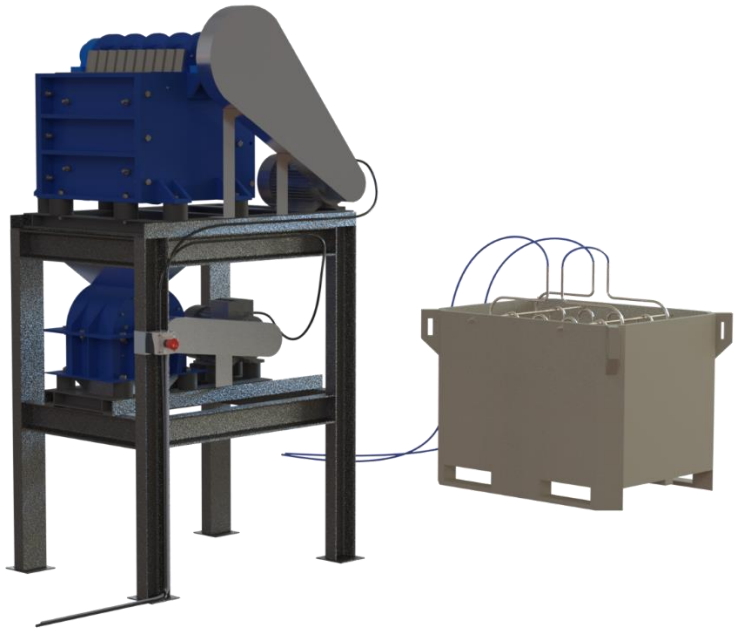

APPENDIX I

Functional Block Diagram

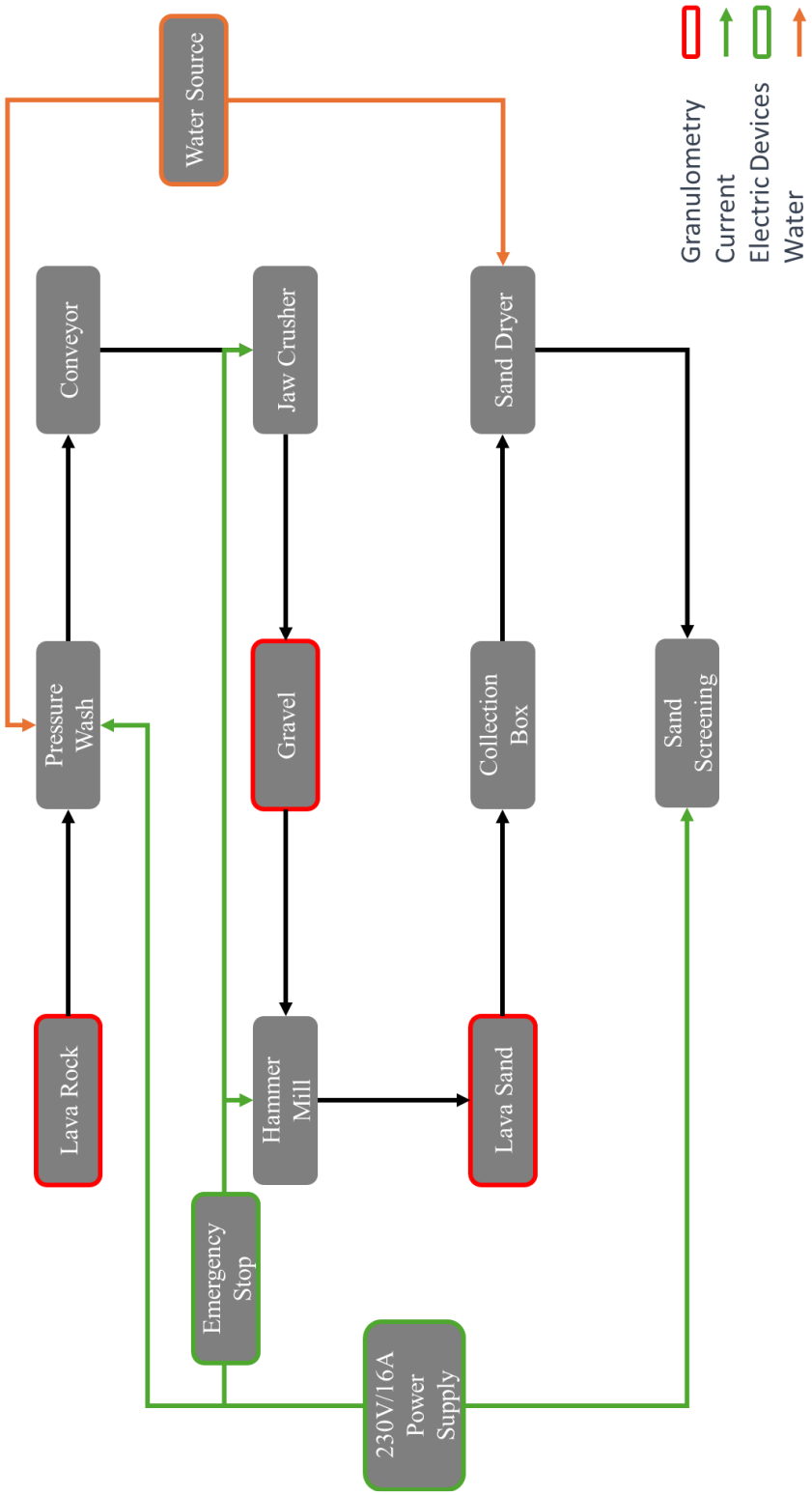

APPENDIX J

ABET Outcome 2, Design Factor Considerations

ABET Outcome 2 states "*An ability to apply engineering design to produce solutions that meet specified needs with consideration of public health safety, and welfare, as well as global, cultural, social, environmental, and economic factors.*"

Table 14. Design Factors Considered

Design Factor	Page number, or reason not applicable
Public health safety, and welfare	Section 3.4.1, pg. 5
Global	N/A since this project focuses on a single location
Cultural	N/A the system has no cultural impact
Social	N/A the system has no social impact
Environmental	Section 3.4.2, pg. 5
Economic	Section 3.4.2, pg.5
Reference for Standards	Section 3.3, pg. 4